Encyclopedia of Nanoscience and Nanotechnology
www.aspbs.com/enn

Micro- and Nanomechanics

Barton C. Prorok
Auburn University, Auburn, Alabama, USA

Yong Zhu, Horacio D. Espinosa,* Zaoyang Guo, Zdenek P. Bazant
Northwestern University, Evanston, Illinois, USA

Yufeng Zhao, Boris I. Yakobson
Rice University, Houston, Texas, USA

CONTENTS

1. MECHANICS OF SCALE

It has been known for quite some time that materials and structures with small-scale dimensions do not behave in the same manner as their bulk counterparts. This aspect was first observed in thin films where certain defect structures were found to have deleterious effects on the film's structural integrity and reliability. This became a significant concern because thin films are routinely employed as components in microelectronics and microelectromechanical systems (MEMS). Their properties frequently allow essential device functions and therefore accurate identification of these properties is key to the development of new technologies. Unfortunately, most of our knowledge is based on bulk material behavior, which many times fails to describe material response in small-scale dimensions because of the dominance of surface and interface effects, finite number of grains in a given structure (e.g., through the thickness), and the role played by the manufacturing process (e.g., texture, residual stress, and dislocation structure). This last feature is particularly important since material surfaces and microstructures are the result of the process employed to deposit or remove material [1].

1.1. Thin Films

As thin film dimensions begin to approach that of the films microstructural features, the material mechanical properties begin to exhibit a dependence on the specimen size. In metallic thin films this translates to plastic yielding occurring at increased stresses over their bulk counterparts. Although this phenomenon was observed as early as 1959 [2], no consensus or common basic understanding of it yet exists. In addition to plastic behavior, other mechanical properties can exhibit size effects, such as fracture toughness and fatigue resistance. Each of these properties operates on a characteristic length scale that can be compared to the physical dimensions of microelectronics, microdevices, or nanodevices. This is shown schematically in Figure 1, which utilizes a logarithmic length scale map beginning at the atomic scale and ending at the macro scale. On the left are four categories of structures and the regime where their dimensional size fits on the length scale. On the right are regimes indicating where dimensional size effects begin to affect the material mechanical properties and theories used to predict behavior. Elastic properties are dependent on the bonding nature of the material and only exhibit size effects at the atomic scale. In contrast, plastic, fatigue, and fracture properties all exhibit size effects in the micrometer and submicrometer regime. These properties all depend on defect generation and evolution, which are mechanisms that

---

[*] Corresponding author.

ISBN: 1-58883-061-6/$35.00

Encyclopedia of Nanoscience and Nanotechnology
Edited by H. S. Nalwa
Volume 5: Pages (555–600)

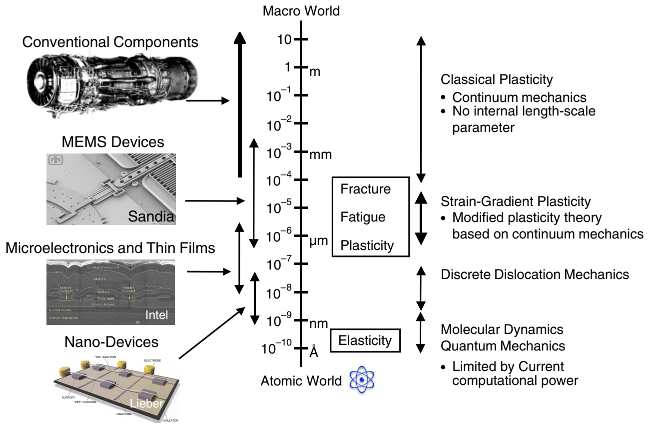

Figure 1. Illustration of length-scale effects on the mechanical properties of materials.

operate on characteristic length scales [3]. These fundamental changes in mechanical behavior occur in the size scale of MEMS and microelectronics devices, and thus, a better understanding of inelastic mechanisms is required to better predict their limits of strength and reliability.

The right side of Figure 1 also lists the theories used to predict material behavior and the length scale where they are applicable. These include classical plasticity, strain gradient plasticity, discrete dislocation mechanics, molecular dynamics, and quantum mechanics. Classical plasticity is described in terms of traditional continuum mechanics, which describes the relationships between stress and strain and is applicable for predicting behavior from a size of approximately 100 micrometers and greater. Molecular dynamics (MD) is at the other end of the scale and involves the generation, mobility, and interaction between individual dislocations, twinning, stacking faults, and other defects. It is only applicable at the lower end of the scale since it is based on large scale numerical simulation. Therefore, it is subsequently limited by current computational power (i.e., systems approximately one million atoms in size). In the regime between classical plasticity and discrete dislocation mechanics, a theory called strain gradient plasticity has been developed in the last decade to describe material behavior [4]. It considers the effect of gradients in strain in the description of flow behavior. A large number of theories have been proposed. However, as will be discussed in Section 4, most of these theories exhibit unreasonable predictions as the size of the structure approaches one nanometer. For this reason, its applicability is limited to structures with minimum dimension of a few hundred nanometers. Between this theory and molecular dynamic, a model based on discrete dislocation dynamics has been postulated [5–7]. These models are currently in an early stage of development so they are not discussed here in detail.

The mechanical response of thin films depends on many factors. Of particular importance is the existence of film thickness effects that arise because of geometrical constraints on dislocation motion. Size effects on mechanical properties begin to play a dominant role when one or more of the structure's dimensions begins to approach the scale of the material microstructural features. The onset of plastic deformation depends strongly on the ability of dislocations to move under an induced stress [8, 9]. The ease of their movement can be hindered by any number of obstacles such as grain boundaries, precipitates, interfaces, etc. Specimen size then begins to govern plastic behavior by creating geometrical constraints, surface effects, and the competition of deformation mechanisms (i.e., dislocation motion versus twinning or phase transitions). Other effects that specimen size can have on plastic deformation involve microstructural changes. This includes grain size, morphology, and crystallographic texture. Preferential grain orientations can result from a minimization of surface energies [10, 11]. The average grain size is also typically on the order of the film thickness, due to an effect called the "specimen thickness effect" which depends upon grain boundaries being pinned by their surface grooves, occurring when the mean equivalent grain diameter is on the order of the film thickness [12, 13].

Several theoretical models, based on single dislocation motion, have been proposed to explain the size effect phenomenon [14–16]. However, each predicts strength increases far below experimentally obtained values. The higher yield point of metallic thin films is likely the result of a combined interaction between strain hardening and deformation mode transition from dislocation motion to twinning.

Several pioneering studies have experimentally identified the existence of size effects on the plasticity of metals. These studies were able to obtain experimental nanoindentation data showing a strong size effect as evidenced by material hardness decrease as indentation depth increases [17–19]. Figure 2 is a reproduction of the data from Ma and

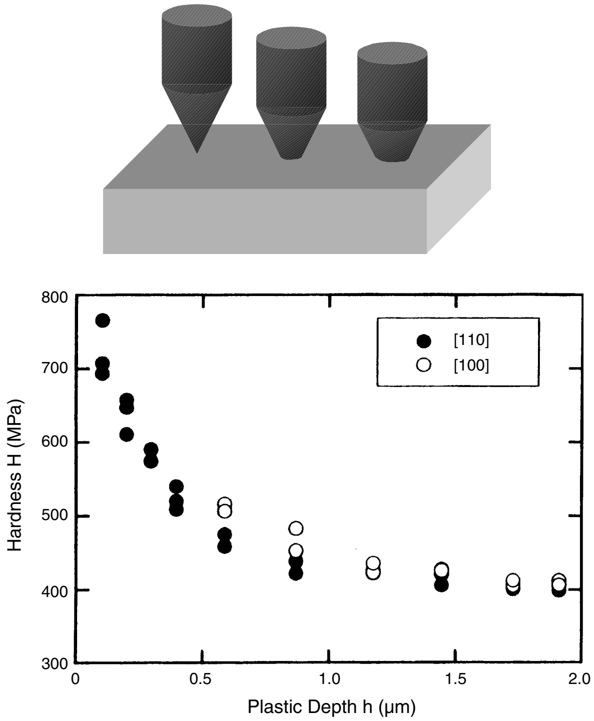

Figure 2. Plot of hardness vs plastic depth illustrating how hardness increases with smaller plastic depth. Reprinted with permission from [18], Q. Ma and D. R. Clarke, *J. Mater. Res.* 10, 853 (1995). © 1995, Materials Research Society.

Clarke [18] of nanoindentation performed on epitiaxially grown silver on sodium chloride and shows that the hardness increases by a factor of two to three as penetration depth decreases. Their results have been verified and expanded in subsequent studies [20–27].

Other pioneering work involved bending strips of metal of varying thickness around a rigid rod [28] and applying a torque load to copper rods of varying diameter [29]. The strips varied in thickness from 12, 25, and 50 μm and each was bent around a rigid rod whose diameter was scaled to the film thickness to ensure identical states of strain in each strip. Figure 3 shows the results in the form of normalized bending moment versus surface strain. It is clear from this plot that as each strip was strained to the same degree, the thinner strips required a larger bending moment. The copper rod experiment used rods of varying diameter, 12–170 μm. A torque was applied to each rod in order to twist them all to the same degree (i.e. to identical states of strain). A plot of torque versus twist per unit length is shown in Figure 4 and indicates an increase in strength by a factor of three for the smallest rod over the largest. Direct tensile tests were also performed on identically sized copper rods (Fig. 4). The authors concluded that for the most part, no size effects existed when subjected to direct tension. The results of these tests show a strength increase for smaller structures over larger ones when subject to bending and torsional loads.

In these pioneering studies, the size dependence of the mechanical properties was considered to be a result of nonuniform straining [23, 29, 30]. It was shown that classical continuum plasticity could not predict the size dependence in this regime. The generally accepted size limit for accurate description of plasticity by the classical theory is systems with dimensions greater than approximately 100 μm. As previously mentioned, molecular mechanics can accurately describe material behavior at the atomic level. However, due to the computational cost and limitations on performing atomistic simulations for more than one million atoms, the maximum size regime computationally approachable is systems with dimensions <0.1 μm [30]. This leaves an intermediate region where a continuum strain gradient plasticity theory, to describe material behavior, is highly desirable [4, 29–35].

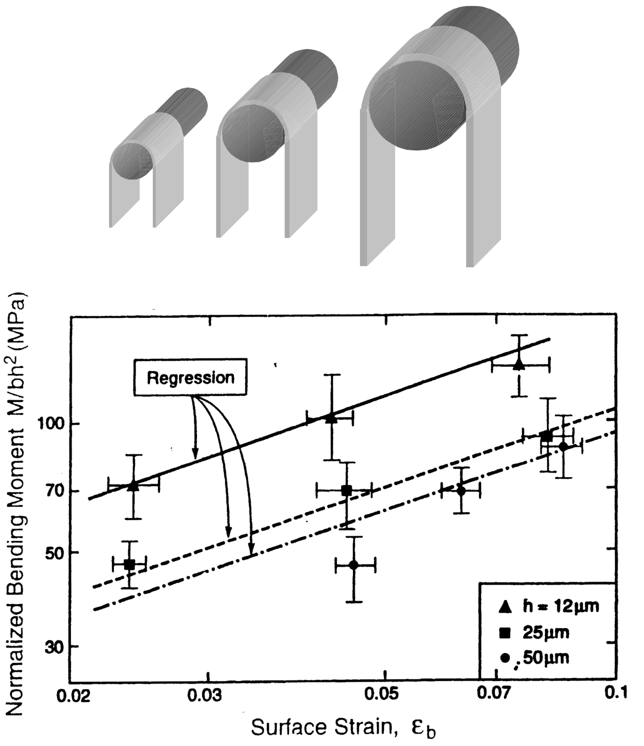

Figure 3. Plot of normalized bending moment vs surface strain illustrating how the thinner films require more bending moment for the same state of strain. Reprinted with permission from [28], J. S. Stolken and A. G. Evans, *Acta Mater.* 46, 5109 (1998). © 1998, Elsevier Science.

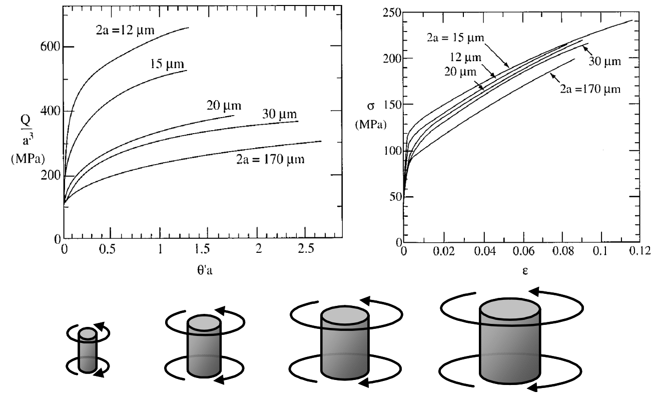

Figure 4. Plot of applied torque vs twist for copper rods of varying diameter and stress–strain of identical rods subject to direct tension. Reprinted with permission from [29], N. A. Fleck et al., *Acta Metal. Mater.* 42, 475 (1994). © 1994, Elsevier Science.

In the aforementioned work of Fleck et al. [29], direct tensile tests were also performed on identically sized copper wires. The authors concluded that for the most part, no size effects existed for this case. It should be noted that the smallest rod diameter investigated by this group was 12 μm. The homogeneous manner in which the uniaxial tests were conducted appears to have hindered gradients in plasticity from occurring. Can size effects then exist in the absence of strain gradients? Recent work on tensile testing of thin gold films of submicrometer thickness has shown that strong size effects do indeed exist in the absence of strain gradients [36–39]. In these studies, grain size was held constant at approximately 250 nm while specimen thickness and width were varied systematically. Figure 5a is a composite scanning electron microscopy (SEM) image showing the side view of the three studied membranes with different thicknesses. For each thickness, there is a characteristic number of grains composing the film ranging from one to five. Stress–strain plots for these films are presented in Figure 5b. They show that the yield stress more than tripled when film thickness was decreased from 1 to 0.3 μm, with the thinner specimens exhibiting brittle-like failure and the thicker a strain softening behavior. It is believed that these size effects stem from the limited number of grains in the film thickness, which limits the number of dislocation sources and active slip systems. In such case, other deformation modes such as twining and grain boundary shearing accompanied by diffusion become dominant [36]. The same features were observed in other face center cubic (fcc) metals [36].

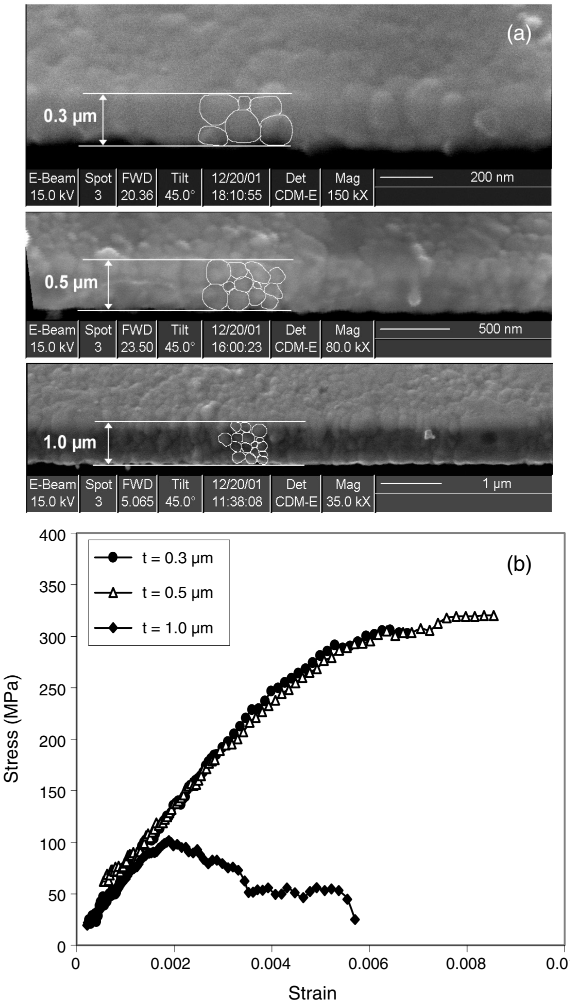

Figure 5. SEM image highlighting the number of grains existing through the film thickness (a). Note the various magnifications and 45° tilt employed during imaging. Stress–strain plot for a gold membranes 0.3, 0.5, and 1.0 μm thick (b). Reprinted with permission from [37], H. D. Espinosa et al., *J. Mech. Phys. Solids* 51, 47 (2003). © 2003, Elsevier Science.

Clearly there are many things to learn about materials at this scale. Future investigations should be pursued and focus on varying the material microstructure systematically to gain further insight into its effects on the size dependent plasticity phenomenon. Further progress can also be made by combining experimental results with analytical and computational studies to better understand the fundamental deformation mechanisms, particularly the mechanics of dislocation generation, motion, interaction, and the competition between inter- and intragranular deformation processes.

1.2. Nanostructures

As structures move beyond the submicrometer to the nanometer scale, description of mechanical behavior focuses on issues other than the traditional ensemble of defects. For instance, the length scale of a typical dislocation and the volume of material required for it to have significant influence on deformation are large compared to the typical volume of a nanosized object. Therefore, it can be argued that beyond a certain point, other types of defects, surface forces, and intermolecular processes control mechanical behavior.

Nanostructures can be described as either a bulk material with a grain structure of a nominal size in the range of 1 to 100 nanometers, or structures with one or more dimensions below 100 nm. A more rigorous definition is based on the functionality of the structure (i.e., when dimensions are such that new and unique properties can be achieved). An example of a nanostructure is a carbon nanotube, which is a molecular scale fibrous structure made of carbon atoms. They were discovered by Sumio Iijima in 1991 and are a subset of the family of fullerene structures [40]. The simplest way to describe the structure of a carbon nanotube is to imagine a flat plane of carbon graphite rolled into a tube, much the same as a piece of paper; see Figure 6. Like

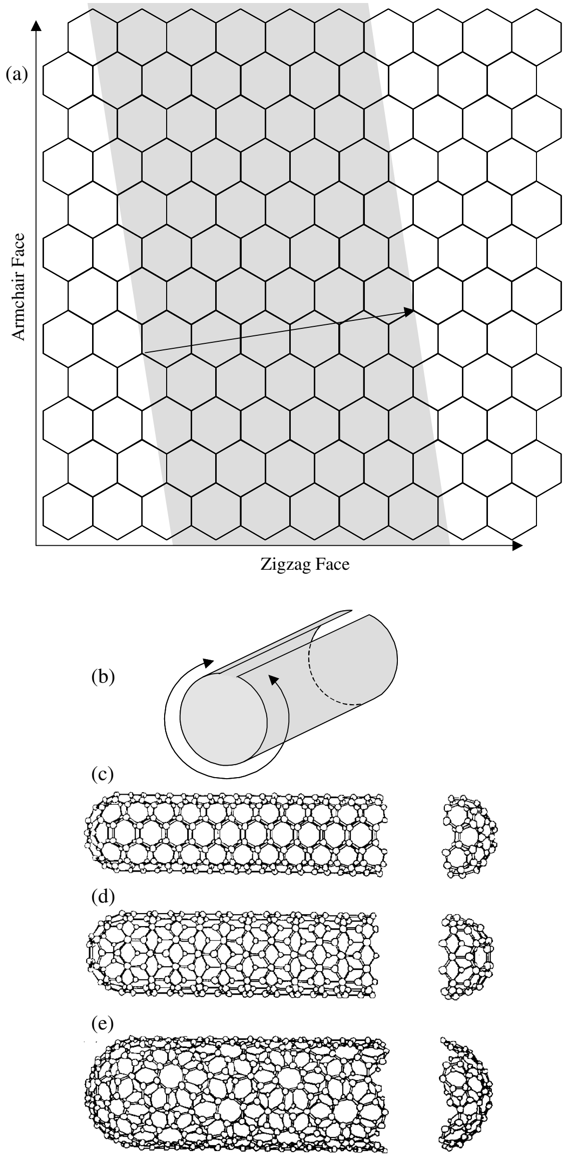

Figure 6. Schematic drawings of a two-dimensional graphene sheet (a), rolled-up sheet (b), and armchair (c), zigzag (d), and chiral (e) nanotubes. (c)–(e) Reprinted with permission from [41], M. S. Dresselhaus et al., *Carbon* 33, 883 (1995). © 1995, Elsevier Science.

paper, a graphene plane can be rolled in several directions to achieve varying structures [41]. Figure 7 shows transmission electron microscopy (TEM) images of carbon nanotubes as a gathered bunch and in a rope-like form [42]. Since their discovery, many scientists have been fascinated by their unique and outstanding properties. Extensive articles and books have been dedicated to carbon nanotubes. Among those, Qian et al. [43] contributed a comprehensive review article, "Mechanics of Carbon Nanotube," from the perspective of both experimentation and modeling.

Dislocation theory has been used to describe relaxation and intramolecular plasticity in carbon nanotubes (CNTs) [44]. By analyzing the dynamic topology of the graphene wall of a CNT, Yakobson argued that dislocations dipoles resulting from Stone–Wales (SW) diatomic interchanges play a key role in CNT relaxation under tension. The dislocation core is identified as a 5/7 pentagon–heptagon and the dipole as a 5/7 attached to an inverted 7/5 core; see Figure 8. When the dislocations unlock, one of two possible mechanisms occurs as a function of temperature. At low temperatures, a mechanism of transformations 7/8/7 and then 7/8/8/7, etc., leads to the brittle failure upon formation of larger molecular openings such as 7/14/7. At high temperatures, the two dislocations glide away from each other in a spiral path. When enough glide has taken place, they leave behind a nanotube of smaller diameter and changed electrical properties; see Figure 8.

A dominant characteristic of nanostructures is that they possess a rather large surface area to volume ratio. As this ratio increases, interfaces and interfacial energy as well as surface topography are expected to play a commanding role in deformation and failure processes. The picture of nanoscale behavior can be viewed as the following: At the larger end of the length scale, 50 to 100 nanometers, dislocation generation and motion will continue to dictate material behavior. As the grain size or structural dimensions fall below this range, behavioral control is transitioned to surface and intermolecular mechanisms. Understanding the mechanics of these materials and structures, and the competition and relationship between their deformation mechanisms, will be essential to predicting their behavior in applications of nanoscale electronics and devices. These types of concerns compose the field of nanomechanics, the foundation of which is currently being laid out.

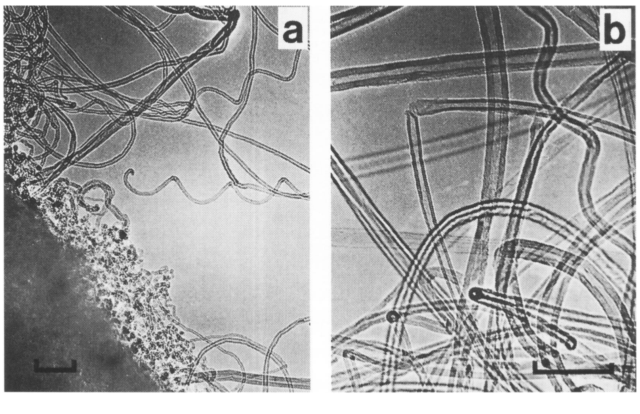

Figure 7. TEM image of a gathered collection of carbon nanotubes (a) and bunched in a ropelike form. Reprinted with permission from [42], V. Ivankov et al., *Carbon* 33, 1727 (1995). © 1995, Elsevier Science.

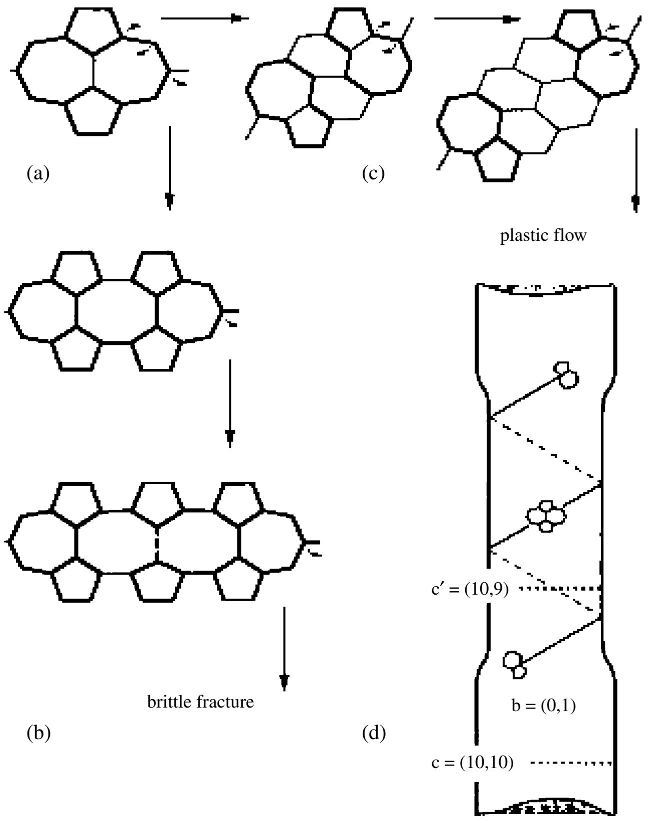

Figure 8. (a) In an armchair CNT, the first Stone–Wales rotation of an equatorially oriented bond into a vertical position creates a nucleus of relaxation. SW rotations marked by arrows show further evolution as (b) a brittle crack or (c) a couple of dislocations gliding away from each other. (d) The change of the CNT chirality and a stepwise change of diameter cause the corresponding variations of electrical properties. Formation of the next SW defect continues the necking process, unless the dislocations pile up at insufficient temperature. Reprinted with permission from [44], B. I. Yakobsons, *Appl. Phys. Lett.* 72, 918 (1998). © 1998, American Institute of Physics.

2. MICRO- AND NANOSCALE MEASUREMENT TECHNIQUES

Mechanical testing at the micro- and nanoscales is quite challenging. Since the physical dimensions of specimens range from a few hundred micrometers down to as small as 1.0 nanometer, novel mechanical testing methods have been developed to successfully measure their properties. Specimens of such size are easily damaged through handling and it is difficult to position them to ensure uniform loading along specimen axes. They are also difficult to attach to the instrument grips. Testing has been shown to suffer from inadequate load resolution as well as having data reduction formulas that are hypersensitive to precise dimensional measurements. To minimize these effects, a variety of micro- and nanoscale testing techniques have been employed to investigate size effects on mechanical properties. Reviews detailing the particulars are given in [15, 45–47].

2.1. Thin Film Measurement Techniques

The mechanical testing of thin films has been pursued for a few decades. The methods are quite unique and diverse. They can be grouped into four categories: depth sensing indentation, bending or curvature, tensile tests, and microelectromechanical system approaches.

2.1.1. Depth Sensing Indentation

Depth sensing indentation is a widely used method for estimating the mechanical properties of materials whereby a material's resistance to a sharp penetrating tip is continuously measured as a function of depth into the material. The result is a load-displacement signature with loading and unloading segments that describe material response. In recent years, instruments have been developed possessing subnanometer accuracy in displacement and submicro-Newton accuracy in load [48–52]. Another major improvement in the indentation methodology is the ability to continuously measure contact stiffness at any point during the test. These new tools have fueled interest in studying the mechanical properties of thin films and nanostructured materials by nanoindentation.

In indentation testing, the indenter tip geometry is generally pyramidal or spherical in shape and fashioned from single crystal diamond. In micro- and nanoscale testing the most frequently used indenter is the three-sided Berkovich tip. This geometry allows the tip to be ground to a very fine point, as opposed to the chisel-like point in four-sided Vickers indenters, resulting in self-similar geometry over a wide range of indentation depths. Other indenter geometries include spherical (good for defining the elastic-plastic transition of a material; however, there is great difficulty in obtaining high-quality spheres of sufficient hardness), cube-corner (sharper than the Berkovich, but produces much higher stresses and strains in the indenter vicinity that results in cracking), and conical (has self-similarity like the Berkovich with an additional advantage of no stress concentrations from sharp edges; however, like the spherical indenter there is difficulty in manufacturing high quality tips). Table 1 summarizes the various indenter geometries.

The process of driving the indenter into the material can be described as follows. After making contact, load is applied to either maintain a constant tip displacement rate or a constant strain rate. Initially, deformation constitutes only elastic displacement of the material, which quickly evolves into permanent or plastic deformation as the load is increased. Thus, zones of elastic and plastic deformation surround the penetrating tip with plasticity mostly occurring in the vicinity of the tip and elasticity occurring ahead of the plastic front. The situation is best described as a complex interplay of elastic and plastic deformation processes. After the prescribed maximum depth is achieved the unloading process begins. As the load on the indenter is reduced, elastic recovery of the material forces the indenter upward. The measured load-deflection signature of this unloading process is then governed only by the elastic properties of the material. Typical loading and unloading curves are shown in Figure 9. These curves show the behavior for a hard (○) and a ductile (●) material. In comparison, the harder material requires a larger load to drive the indenter to the same

Table 1. Geometries of various indenters.

Parameter	Berkovich	Cube-corner	Cone	Spherical	Vickers
Shape			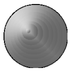	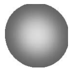	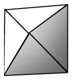
C-f angle	65.35°	35.264°	—	—	68°
Projected Contact area	$24.5600d^2$	$2.5981d^2$	πa^2	πa^2	$24.5044d^2$

C-f stands for centerline to face angle, *d* stands for indentation depth, and *a* stands for tip radius for cone and spherical indenters.

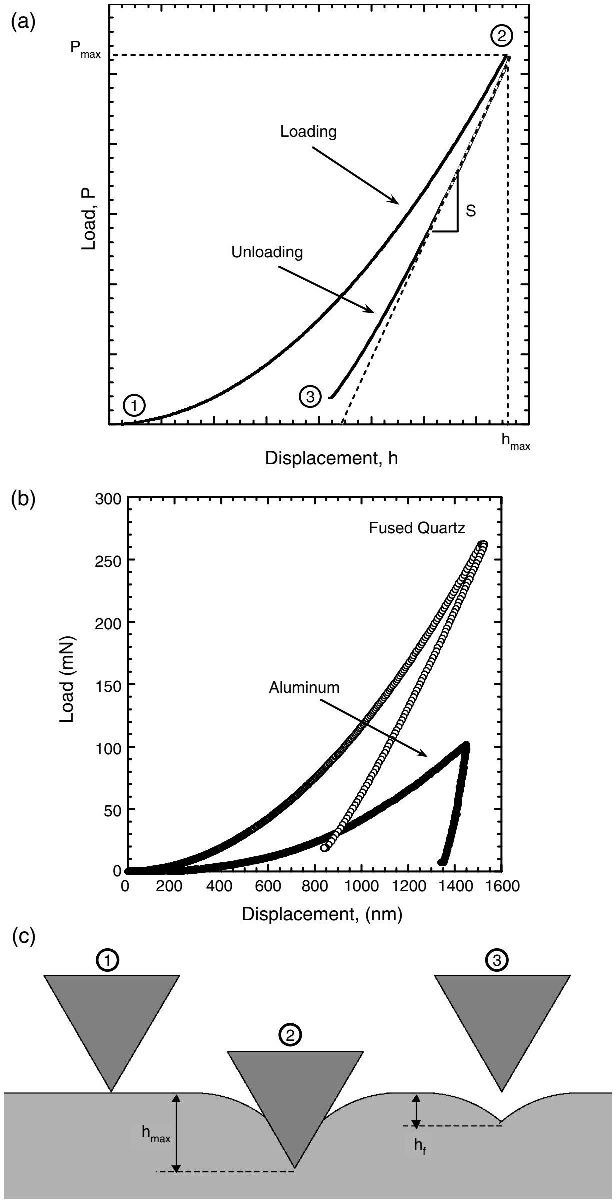

Figure 9. Schematic of the typical load-displacement signature obtained by nano-indentation (a). Comparison between hard (fused quartz) and soft (aluminum) materials (b), and side-view schematic of the nano-indentation process where the circled numbers correspond to the points in the load-displacement curve above (c).

penetration depth, reflective of its higher atomic cohesion. The harder material also stores more elastic energy than the softer material and undergoes less permanent deformation. This is seen during unloading where the harder material traces a path closer to its loading curve than the softer material. The softer material has a nearly vertical unloading signature. This is indicative of very little elastic recovery. When comparing the residual indentation marks the softer material exhibits a larger and deeper mark.

Indentation testing uses the maximum point of the load-deflection signature to determine the hardness (H) of the material, defined as the ratio of applied load (P) to the indenter/material contact area (A):

$$H = \frac{P}{A} \tag{1}$$

The contact area is determined using the relationship describing the surface area of the indenter with indentation depth, given in Table 1 for the various tip geometries. This value is referred to as the "universal hardness" and includes contributions from both elastic and plastic deformation. With today's instrumentation testing systems, this can be calculated on a continuous basis as a function of indentation depth.

Young's modulus (E) is another important material property that can be determined with nanoindentation testing. There are two methods for determining these properties based on the load displacement signature of the indent. The first involves a technique developed by Doerner and Nix [53] who took the approach that during the early stages of unloading, the contact area between the indenter and material is constant. Thus the unloading stiffness, S, is related to the materials modulus via

$$S = \frac{dP}{dh} = \frac{2}{\sqrt{\pi}} E_r \sqrt{A} \tag{2}$$

where S is measured stiffness of the upper portion of the unloading curve, dP is the change in load, dh is the change in displacement, A is the projected contact area, and E_r is the effective modulus determined by

$$\frac{1}{E_r} = \frac{(1-\nu^2)}{E} + \frac{(1-\nu_i^2)}{E_i} \tag{3}$$

where E and ν are the elastic modulus and Poisson's ratio for the specimen and E_i and ν_i are the same parameters for the indenter. An important aspect of this method is the accurate determination of contact area. By extrapolating the linear portion of the unloading curve to zero load (see Fig. 9), an extrapolated depth can be used to determine contact area. A perfect pyramid can be assumed at indentation depths above 1 μm. However, below 1 μm a correction factor must be used in order to account for blunting of the tip point [53]. This was accomplished by employing the TEM replica technique to determine the Berkovich indenter shape. Deviations from a perfect Berkovich tip below 1 μm were identified.

Oliver and Pharr [54] built on these solutions by realizing that unloading data is usually not linear but better described with a power law,

$$P = A(h - h_f)^m \tag{4}$$

where P is the load, h is the displacement, and A, m, and h_f are constants determined by a least squares fitting procedure. Elastic modulus is then obtained from a variation of Eq. (2),

$$S = \frac{dP}{dh} = \frac{2}{\sqrt{\pi}} E_r \sqrt{A}\beta \tag{5}$$

where β describes the correction of the area function due to tip blunting, approximately 1.034 for a Berkovich indenter [54]. The advantage of the Oliver and Pharr method is that the indent shape does not need to be directly measured. The method is based on the assumption that elastic modulus is independent of indentation depth. By modeling the load frame and specimen as two springs in series the total compliance, C, can be expressed as

$$C = C_f + C_s = C_f + \frac{\sqrt{\pi}}{2E_r}\frac{1}{\sqrt{A}} \tag{6}$$

where C_f is the load frame compliance and the compliance of the specimen, C_s, is $\frac{1}{S}$; see Eq. (2). If the elastic modulus is constant with indentation depth, then a plot of C vs $A^{-1/2}$ is a linear function whose intercept is C_f. For large indentation depths, the area function for a perfect Berkovich indenter can be used, namely,

$$A(h_c) = 24.5H_c^2 \tag{7}$$

Equation (7) is also a good starting place to estimate the area function of the Berkovich tip. The area function for the tip is ascertained from a series of indents at periodic depths, 100, 200, 400, 600, 1200, 1800 nm. For large indent depths it also gives initial estimates of C_f and E_r. These values can then be plugged back into Eq. (6) to further estimate the contact area for the successively smaller indents. This data can be fit to the function

$$A(h_c) = 24.5H_c^2 + C_1 h_c^1 + C_2 h_c^{1/2} + C_3 h_c^{1/4} + \cdots + C_8 h_c^{1/128} \tag{8}$$

where C_1 through C_8 are constants. The first term is the perfect Berkovich tip and the others describe the blunting of the tip. In order to obtain the most accurate area function, this new value must be plugged into Eq. (6) again, the process being iterated until convergence is attained.

Oliver and Pharr confirmed their method by obtaining data for nine materials of varying properties and plotting the computed contact area versus indentation depth with all materials falling on an identical linear line defining the tip area function. See Figures 24 and 25 in Oliver and Pharr [54]. Once the area function is known, it can be used to calculate E and H of other materials.

One inherent feature of these studies is that E and H are not directly measured and that some of the assumptions used in the data reduction may be violated. One of the key assumptions is the power law given in (3), which is obtained from a contact elasticity solution of a half space. These assumptions become quite relevant in thin films for which substrate effects are part of the experimental signatures [55–57]. Bückle [58] has recommended that indentation depth in microindentation should not exceed 10% of the film thickness in order to obtain reliable results. This is currently used as a guideline in nanoindentation, which limits the minimum film thickness that can be reliably tested, using the standard data reduction procedure given by Oliver and Pharr to approximately 1–2 μm and larger. In general, this limit is a function of substrate properties and film roughness. Nix and co-workers developed a methodology to account for the substrate effect, which enables the property measurement of much thinner films.

The load-depth signature is a complex quantity that is affected by events such as cracking, delamination, plastic deformation, strain hardening, phase transitions, etc. In particular, gradients in elastic and plastic strains exist and are a function of indentation depth [22, 23, 33, 35, 59]. Thus, many interpretative methodologies have been devised in an attempt to deconvolute these effects [60, 61].

A major complication of the nanoindentation technique, observed in some materials, is the so-called “pile-up” and “sink-in” of the material around the indenter tip [24, 62, 63]. Both effects are primarily a result of the plastic behavior of the material and have a significant effect on the contact area between the tip and specimen. Furthermore, the solutions given are based on elastic contact mechanics and do not consider the effects of plasticity in the indentation process. The inclusion of plasticity into the solution is a complex process since the constitutive equations are nonlinear. Also, material properties such as yield stress and work hardening must be included, which are heavily dependent on microstructural aspects that can vary from specimen to specimen.

Figure 10 illustrates the problems of “pile-up” and “sink-in.” Pile-up occurs in soft materials, such as metals, whereby the ease of deformation results in localized deformation in the region near the indenter tip. The result is material piling up around the indenter and effectively increasing the contact area between sample and indenter. By contrast, stiffer materials are more difficult to deform and the strain fields emanating from the penetrating indenter spread further into the material and effectively distribute the deformation to more volume, further away from the indenter. The sink-in effect arises from this feature and results in less contact area between the indenter and sample. The result is that pile-up tends to overestimate hardness and modulus due to higher contact areas and sink-in tends to underestimate hardness and modulus due to lower contact area.

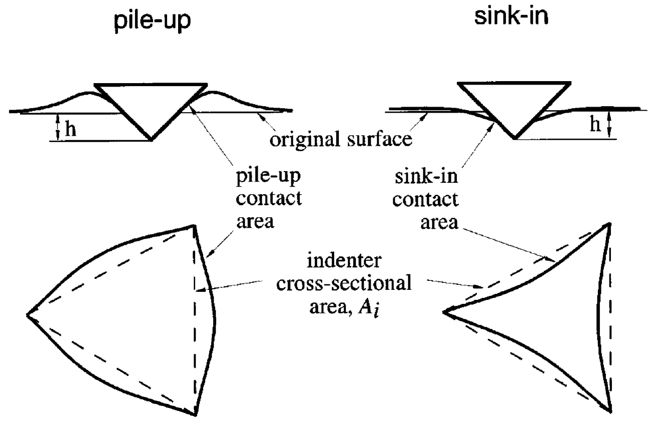

Figure 10. Schematic representation illustrating how the contact area changes during pile-up and sink-in effects. Reprinted with permission from [24], K. W. McElhaney et al., *J. Mater. Res.* 13, 1300 (1998). © 1998, Materials Research Society.

Attempts to deconvolute the substrate effects were investigated by Saha and Nix [56]. In this work, soft films that were deposited on a variety of relatively harder substrates were probed by nanoindentation; see Table 2. These systems included cases where elastic homogeneity existed between the film and substrate, that is, when the expected elastic modulus of the film was equivalent to the substrate (e.g., aluminum on glass), and cases where elastic modulus differed significantly (aluminum on sapphire). By employing the parameter P/S^2, where P is the indenter load and S is the contact stiffness, and plotting it versus indentation depth, a description of material behavior is obtained. This parameter was first proposed by Joslin and Oliver [64], who realized that both components, P and S, are directly measured in the test. They examined and combined their analytical relations, Eq. (1) for P and Eq. (5) for S, to obtain

$$\frac{P}{S^2} = \frac{1}{\beta^2}\frac{\pi}{4}\frac{H}{E_r^2} \tag{9}$$

which shows that the parameter is independent of the contact area (i.e., tip calibration) and thereby is also not corrupted by pile-up or sink-in effects. Since H and E remain constant with indentation depth for homogeneous materials, the parameter P/S^2 should be independent of depth as well. By this method, Saha and Nix have shown that when elastic homogeneity between film and substrate is met, the Oliver and Pharr data reduction method [54] allows the decoupling between indentation size effects, at small depths, and substrate induced strain gradient effects, at large depths whereby a plateau representing true intrinsic material behavior is obtained.

In the same work, Saha and Nix [56] also developed a method to account for substrate effects in cases that do not possess elastic homogeneity. Using the elastically homogeneous aluminum (Al) film on glass substrate as a starting point, they first assumed that since the glass substrate is much harder than the aluminum, all plastic deformation is accommodated by the Al film with no deformation occurring in the substrate until the indenter makes contact with it. This allowed them to make a second assumption, basically that the film hardness measured for the Al/glass system was its intrinsic value and therefore also representative of the film hardness for the Al/sapphire system. With this knowledge they calculated the reduced modulus via Eq. (9) and

Table 2. Film/substrate systems tested by Saha and Nix. Al/Al, Al/glass, W/sapphire are elastically homogenous systems.

Films	Substrates	E (GPa)	H (GPa)
Aluminum (Al)	aluminum	75	1
$E = 75$ GPa			
$H = 1$ GPa	glass	73	6
Tungsten (W)	silicon	172	13
$E = 410$ GPa			
$H = 15$ GPa	sapphire	440	30

corresponding true contact area from Eq. (5). These values provided a means to compare experimental work with an existing model developed by King [65]. The King model was actually a modification of a treatment developed by Doerner and Nix [53] who, in the specific case they studied, were able to include a term in the reduced modulus, E_r, to account for the substrate effect. The King treatment built on this by modeling the system with a flat triangular indenter geometry resulting in a reduced modulus given by

$$\frac{1}{E_r} = \frac{1-\nu_i^2}{E_i} + \frac{1-\nu_f^2}{E_f}(1-e^{-\alpha t/a}) + \frac{1-\nu_s^2}{E_s}(e^{-\alpha t/a}) \tag{10}$$

where E_s and ν_s are the elastic modulus and Poisson's ratio of the substrate respectively, a is the square root of the projected contact area, t is the thickness of the film below the indenter, and α is a scaling parameter that depends on a/t, which varies with indenter geometry. Saha and Nix have modified this analysis through incorporating a Berkovich indenter geometry by replacing t in Eq. (10) with $(t-h)$, where h is the indenter displacement into the film. Thus,

$$\frac{1}{E_r} = \frac{1-\nu_i^2}{E_i} + \frac{1-\nu_f^2}{E_f}(1-e^{-\alpha(t-h)/a}) + \frac{1-\nu_s^2}{E_s}(e^{-\alpha(t-h)/a}) \tag{11}$$

Substituting constants for E and ν of each component, with E_f taken from the elastically homogeneous case, yields the reduced modulus as a function of indentation depth that can be compared with the experimental E_r calculated through Eq. (9). Sara and Nix found that these two methods are in good agreement for up to 50% of the film thickness, after which the experimentally obtained E_r begins to decrease. Finally, by incorporating the experimentally obtained E_r values into the modified King model, a plot of the film modulus versus indentation depth is obtained; see Figure 11. Here E_f is seen to agree well up to 50% of the film thickness before beginning to decrease indicating that the King model is overpredicting the effect of the substrate. These data show that the modified analysis based on Eq. (11) is an effective method for estimating thin film modulus wherever substrate effects become relevant.

Hardness and elastic modulus are the properties most routinely measured by nanoindentation. However, it has also been shown to be an effective method for measuring other material properties such as fracture toughness in small volumes [66, 67], strain rate sensitivity and internal friction [68], and thermally activated plastic flow [69]. The frontier of nanoindentation revolves around combining current measurement and analysis with finite-element techniques [61, 70–73]. This combination will further aid the study of material mechanical behavior, especially those with nonlinear features. Finally, the so-called "Holy Grail" of nanoindentation will be the generation of material stress-strain behavior from indentation data such that mechanical properties, such as yield and postyield properties, can be estimated. Further information on recent progress in nanoindentation can be found in the literature [74–76].

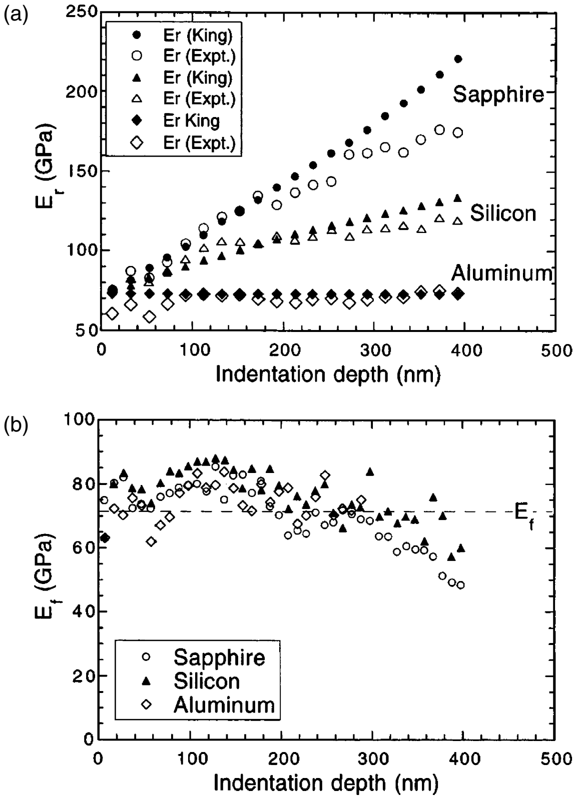

Figure 11. Comparison between modified King model and Saha and Nix experimental data for reduced modulus (a) and film modulus (b) of aluminum film on the substrates indicated. Reprinted with permission from [56], R. Saha and W. D. Nix, *Acta. Mater.* 50, 23 (2002). © 2002, Materials Research Society.

2.1.2. Bending and Curvature

Bending and curvature testing consists of microbeam bending, wafer curvature, and the bulge test. Bending tests on micromachined beams were first performed by Weihs et al. [77] and repeated by others [78–85]. The method involves deflecting a freestanding cantilever-like beam fixed at one end to the substrate. Building such structures on the micrometer scale is achieved with standard microfabrication procedures used in the microelectronics field. Dimensions are on the order of a few micrometers to submicrometer thickness, tens of micrometers wide and hundreds of micrometers in length. Structures of this size have an extremely low stiffness and therefore high-resolution load cells are required to perceive the response of the beam. Nanoindenters have been shown to provide such load resolution and are routinely used to deflect such structures. A schematic of a typical microcantilever structure being deflected by a nanoindenter is shown in Figure 12. By this method, simple elastic beam theory can be applied. Namely,

$$k = \frac{Eb}{4(1-\nu^2)}\left(\frac{t}{l}\right)^3 \tag{12}$$

where k is the stiffness, E is the elastic modulus, b is the cantilever width, ν is Poisson's ratio, t is the thickness, and l is the length of the cantilever at the point of contact.

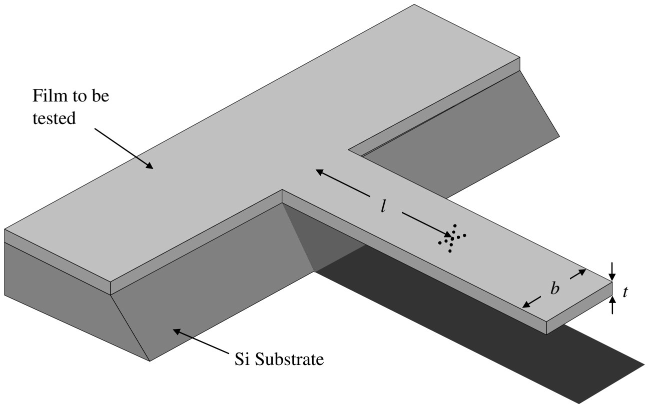

Figure 12. Schematic three-dimensional (3D) view of a freestanding cantilever structure. Parameters are defined in the text.

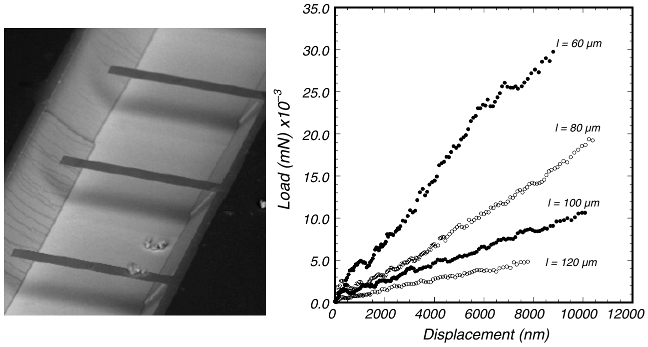

Figure 14. Load-deflection curves comparing load-displacement signatures for cantilevers lengths of 60, 80, 100, and 120 μm. Reprinted with permission from [84], B. C. Prorok et al., *Exp. Mech.* (2003). © 2003, Society for Experimental Mechanics.

An example of results obtained from this method are shown in Figures 13 and 14. Figure 13 is an optical image of a common single crystal Si atomic force microscopy (AFM) tapping-mode tip and the corresponding load-deflection signature obtained after deflecting it with a nanoindenter [84]. In this structure the Si is oriented such that the length of the cantilever is parallel to the [110] direction. The stiffness, k, was found to vary between 2.58×10^{-4} to 2.61×10^{-4} mN/nm which corresponds to a modulus of 166 to 168 GPa when using Eq. (12), close to that of the [110] direction for Si, 170 GPa [86]. Another example of microcantilever bending results is shown in Figure 14 for thin film ultrananocrystalline diamond (UNCD). The figure shows load-deflection results on UNCD freestanding cantilevers at various cantilever lengths [84, 85]. As expected, the stiffness decreased as cantilever length increased. Using Eq. (12), the modulus was found to be between 945 and 963 GPa. The microcantilever bending test has shown to be a viable method to measure elastic properties; however, the technique exhibits some unique features. For example, the analytical solution is very sensitive to the measured thickness, as seen in Eq. (12) where its influence is to the third power warranting that extra care must be taken to accurately measure the specimen thickness. Undercutting during the release step introduces uncertainties in the measurement of the cantilever length. Defining an equivalent cantilever length circumvented this problem [84]. The technique also suffers from boundary bending effects and inhomogeneous distribution of the strain since the bending moment is not constant along the length of the beam. Florando et al. [83] have put forth a solution to this issue by using a beam with a triangular width. Stress-strain behavior for the material can then be more accurately obtained.

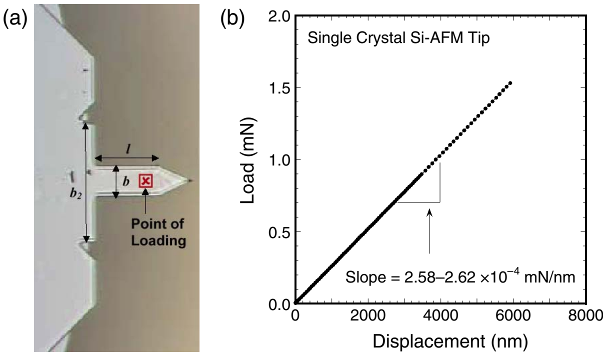

Figure 13. Optical images of (a) a silicon AFM tapping-mode tip and (b) corresponding load-displacement curve. Reprinted with permission from [84], B. C. Prorok et al., *Exp. Mech.* (2003). © 2003, Society for Experimental Mechanics.

Another bending based test is the wafer curvature method. Typically when a thin film is deposited on a substrate at elevated temperatures and then cooled to room temperature, the difference in the thermal expansion coefficient between the two materials will cause curvature in the structure to accommodate the strain. Whether this curvature is convex or concave is determined by which material has the greater coefficient of thermal expansion and if the film has tensile or compressive residual stress. This technique determines film properties by taking advantage of the fact that stress in the film is proportional to the radius of curvature of the substrate [87],

$$\sigma = \frac{E_s}{(1-\nu_s)} \frac{t_s^2}{6t_f} K_f \tag{13}$$

where t_f is the film thickness, t_s if the substrate thickness, $E_s/(1-\nu_s)$ is the biaxial modulus of the substrate, and K_f is the change in curvature. This equation relies on the assumption that the film completely accommodates lattice mismatch with the much thicker substrate [88]. A further constraint limits its application when the maximum bending deflection exceeds more than half the thickness of the substrate, $t_s/2$. Elastic and plastic properties can also be examined by varying the temperature. The technique has been used to examine a variety of thin films [15, 88–99]. There are some complexities of the wafer curvature method that hinder accurate property measurement such as nonuniformity of substrate-material adhesion and temperature. All in all, the method yields information on the material properties when confined by the substrate.

The third major bending based test is the bulge test, developed by Beams in 1959 [100], where a freestanding film is deflected by applying pressure with a compressed gas or liquid. These specimens also take advantage of standard microfabrication procedures to define their structures.

The geometry of the typical specimen consists of a thin film membrane that spans a cylindrical or rectangular chamber beneath. The film is fixed at the edges of the chamber such that the remainder of its structure is freestanding. The chamber is pressurized in a controlled manner that results in the freestanding film bulging upward. The resulting "bulge" height can then be measured by interferometry and other techniques. The test is designed to determine the in-plane mechanical properties of the film by eliminating specimen edge effects. Moreover, it also avoids the complexities of substrate material adhesion problems.

The technique has evolved over the years to settle on high aspect ratio rectangular chambers due to the "wrinkling effect" caused by biaxial states of stress that develop near the corners. This geometry confines the effect to the vicinity of the rectangle's short ends and allows uniform deformation to occur in the middle of the structure. Figure 15 is a cross-section of this region. Here, H is the bulge height, a is the membrane half-width, and P is the applied gas pressure. Pressure is related to bulge height through the relation

$$P = \frac{2\sigma_0 t}{a^2} H + \frac{4Et}{3a^4(1-\nu^2)} H^3 \tag{14}$$

where σ_0 is the residual stress, t is the film thickness, E is the material elastic modulus, and ν is the Poisson's ratio. The result of a test is a pressure-deflection plot describing the membrane behavior. A typical membrane response with several loading and unloading cycles is shown in Figure 16a for a freestanding Au film 1.8 μm thick. A comparison between the bulge and tensile tests was made for Si_3N_4 by Edwards et al. [101], whereby the elastic modulus of each technique was found to vary by as little a 1 GPa, 257 ± 5 GPa for tensile and 258 ± 1 GPa for bulge, and validating the bulge test as a viable wafer-level technique.

The method is able to examine both elastic and plastic properties. As in the case of nanoindentation, the stress-strain state in the film is not measured directly and requires a data reduction procedure that accounts for boundary effects. However, in the case the high aspect ratio membrane, stress and strain are nearly uniform in the short direction and can be approximated by

$$\varepsilon = \frac{2}{3a^2} H^2 \tag{15}$$

$$\sigma = \sigma_0 + \frac{E}{(1-\nu^2)} \varepsilon = \frac{a^2}{2t} \frac{P}{H} \tag{16}$$

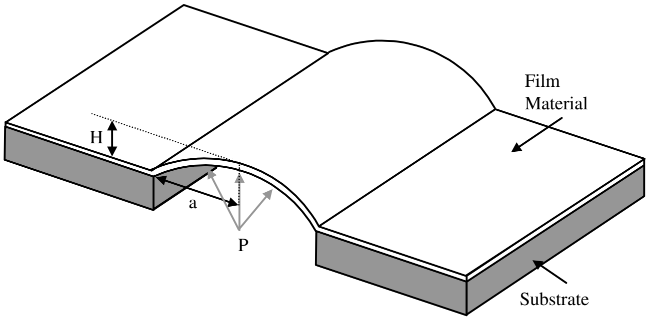

Figure 15. Cross-section of the middle of a high aspect ratio rectangular membrane; parameters are defined in the text.

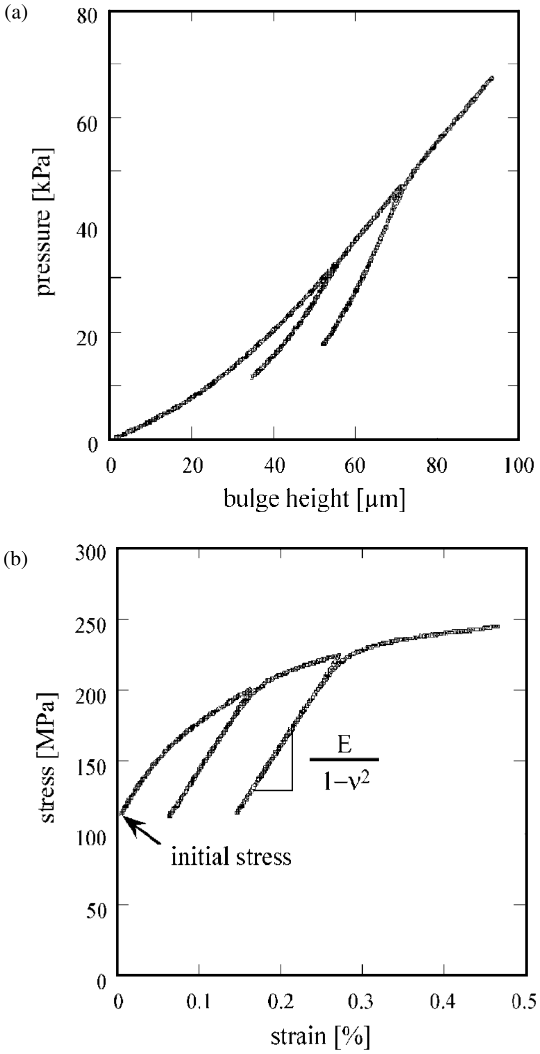

Figure 16. Pressure–height plot (a) and stress–strain plot (b) for bulge testing of an evaporated Au membrane 1.8 μm thick. Reprinted with permission from [46], O. Kraft and C. A. Volkert, *Adv. Eng. Mater.* 3, 99 (2001). © 2001, Wiley-VCH.

Using these equations, stress and strain can be extracted from the data. A plot of the stress-strain response of the data in Figure 16a is shown in Figure 16b. Several studies have utilized this technique to test thin films [102–107]. The apparatus required to perform a bulge test is simple and the method is an easy way of evaluating the in-plane mechanical properties. However, sample preparation is involved and is restricted to thin films with tensile residual stresses. Films with compressive stresses can buckle; in such a case the initial dome height must be determined as accurately as possible to avoid large errors in the experimental results. The experimental values are more accurate when the membrane is flatter.

2.1.3. Tensile Testing

The previously mentioned techniques can all be characterized as methods that subject the specimen to gradients of strain, which at the micro- and nanoscales can complicate extraction of material property data. Also, their flexibility for testing specimens of varying geometry is limited. Thus, the equivalent of a tensile test, customarily to that performed on bulk samples, is desirable in this regard. *Tensile testing* is the most direct method for obtaining a material's mechanical properties. Loads and strains are measured directly and independently, and no mathematical assumptions are needed to identify quantities describing the material response. Many researchers have been involved in an effort to establish a scale-equivalent test [36–39, 83–85, 108–125]. However, tensile testing at the micro- and nanoscales has been difficult to achieve. Difficulties arise from load resolution, specimen fabrication, handling and mounting, uniformity of geometry from specimen to specimen, and independent measurement of stress and strain. The most attractive features of direct tensile testing are that data reduction is straightforward and the tests are much less susceptible to geometrically induced errors. Nonetheless, results reported in the many referenced studies vary somewhat, reinforcing the need for an easy to use tensile test that minimizes sample preparation, handling, and mounting that can produce numerous specimens of identical features.

Several noteworthy tensile testing schemes are worth detailing here. Sharpe et al. [114–118] have developed a micromachined frame containing the specimen. The fabrication process involves patterning the dog-bone specimen on a silicon wafer and then etching a window underneath. The final structure is shown in Figure 17. The finished tensile specimen is then mounted in the testing rig and grips are attached at either end. The two narrow sides are then cut with a rotary tool to free the specimen from the frame support. A piezoelectric actuator is employed to displace the specimen and subject it to uniaxial tension. Load is measured with a load cell possessing a resolution of 0.01 g and a load range of ±100 g, and strain with an interferometric strain displacement gauge. The typical width of specimens is 600 μm and the gauge length is 400 mm. Two sets of orthogonal strips are patterned on the surface of the specimen to reflect the laser beam used in the interferometric strain displacement gauge setup. When illuminated with the laser, the strips produce interference fringe patterns that are used to measure strain with a resolution of ±5 microstrain.

Another tensile testing technique, developed by Tsuchiya et al. [122, 124, 125], employs an electrostatic force gripping system to load the film. The specimen is fabricated as a freestanding thin-film cantilever fixed at one end and with a large pad at the other end. Schematics of the architecture and gripping process are shown in Figure 18. After fabrication and release of the cantilever specimen, a probe is aligned and brought into contact with the specimen free end to be gripped. An electrostatic attractive force is generated between the two surfaces with an applied voltage. Up to certain specimen dimensions, this force is rather large compared to the force required to deform the specimen in tension; therefore, the two remain rigidly fixed together as long as the voltage is applied. Tensile testing is then achieved through piezoelectric actuation of the probe along the axis of the specimen with displacements measured by a strain gauge at the probe. Specimen dimensions in the gauged region are on the order of: length 30–300 μm; width 2–5 μm; and thickness 0.1–2.0 μm.

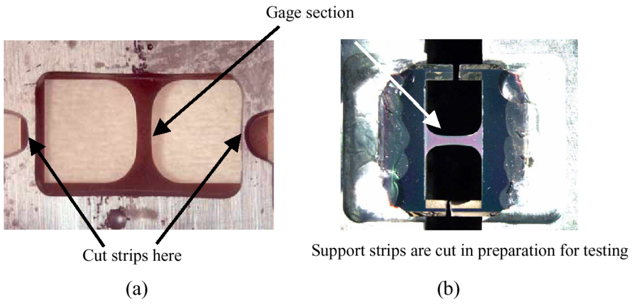

Figure 17. A tensile specimen fabricated at MIT (a) and at CWRU (b). Reprinted with permission from [118], K. M. Jackson et al., *Mater. Res. Soc. Symp. Proc.* 687 (2001). © 2001, Materials Research Society.

Chasiotis and Knauss [112, 113] developed a testing procedure similar to that of Tsuchiya et al. Their test employs electrostatic forces to pull the specimen pad to the substrate while an ultraviolet curing adhesive then fixes a probe to it. This process ensures that the specimen experiences minimum handling during attachment and improves alignment between the specimen and probe since the specimen is temporarily fixed to the substrate. The electrostatic force is then reversed through identical poling of each side to release the

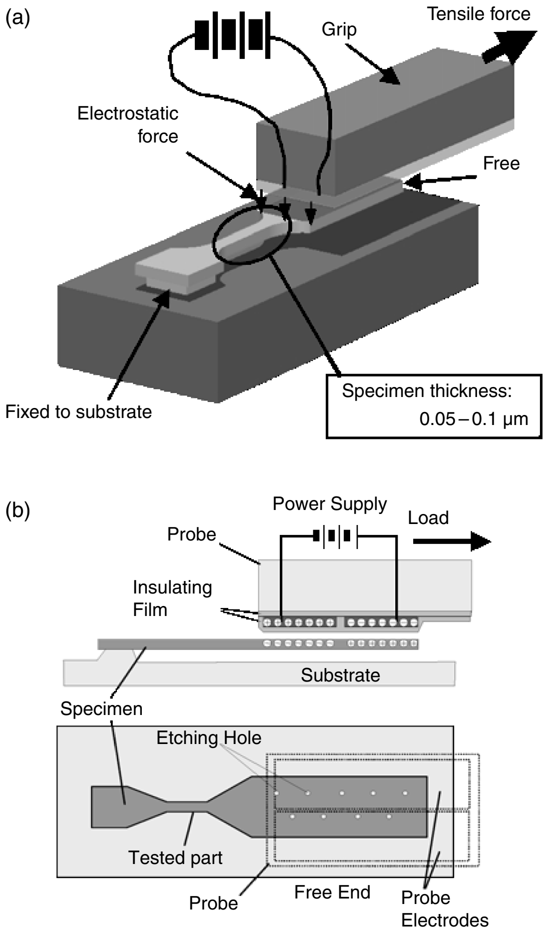

Figure 18. Schematics showing the architecture of the electrostatic grip system. Reprinted with permission from [125], T. Tsuchiya et al., *Mater. Res. Soc. Symp. Proc.* 687 (2002). © 2002, Materials Research Society.

combined pair from the substrate. Tensile testing proceeds in a similar manner to that of Tsuchiya et al. with the main difference being that measurement of strain fields is performed through AFM and digital image correlation (DIC).

Another variation of the microscale tensile test employs the cantilever architecture, but it possess a ring at the free end rather than a gripping pad [120, 126]; see Figure 19. A probe with a diameter just smaller than the inner diameter of the ring is inserted and then pulled in the direction of the specimen axis to apply direct tension. An optical encoder is used to independently measure displacement. Results were compared for two groups of specimens of significantly varying lengths to eliminate the error in stiffness due to deformation of the ring. By assuming that the effective stiffness was the same for each measurement the effect of the ring was canceled out. A problem with this test is the difficulty of eliminating friction between probe and substrate. This feature complicates the data reduction procedure and interpretation of the data.

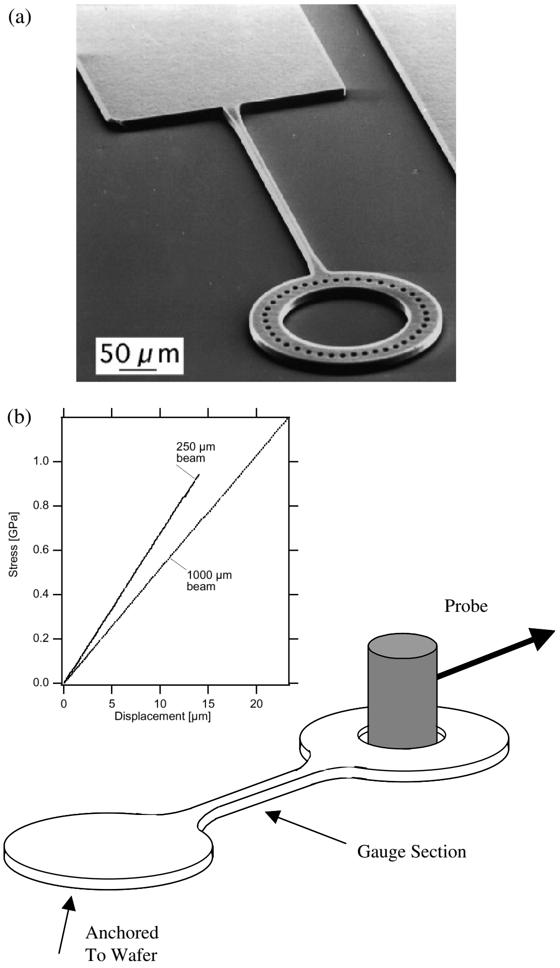

Figure 19. SEM image of the cantilever-ring architecture (a) and schematic of the loading process with experimental results for two specimens of different lengths (b). Reprinted with permission from [126], S. Greek et al., *J. Micromech. Microeng.* 9, 245 (1999). © 1999, Institute of Physics.

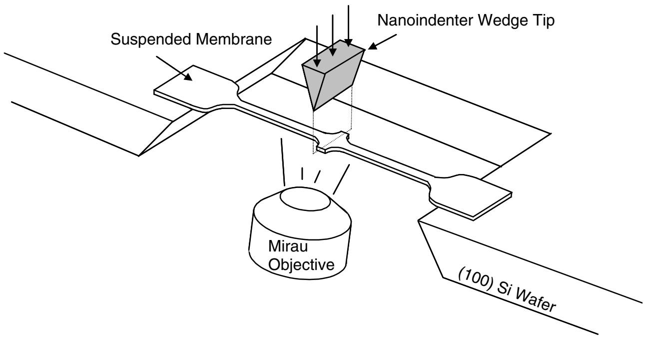

Figure 20. 3D schematic view of the membrane deflection experiment.

Another noteworthy microscale tensile test, called the membrane deflection experiment (MDE), was developed by Espinosa and co-workers [36–39, 119]. It involves the stretching of freestanding, thin-film membranes in a fixed–fixed configuration with submicrometer thickness. In this technique, the membrane is attached at both ends and spans a micromachined window beneath (see Fig. 20). A nanoindenter applies a line-load at the center of the span to achieve deflection. Simultaneously, an interferometer focused on the bottom side of the membrane records the deflection. The result is direct tension in the gauged regions of the membrane with load and deflection being measured independently. The geometry of the membranes is such that they contain tapered regions to eliminate boundary-bending effects and ensure failure in the gauge region (see Fig. 21). The result is direct tension, in the absence of bending and strain gradients of the specimen.

The MDE test has certain advantages; for instance, the simplicity of sample microfabrication and ease of handling results in a robust *on-chip* testing technique. The loading procedure is straightforward and accomplished in a highly sensitive manner while preserving the independent measurement of stress and strain. It can also test specimens of widely varying geometry, thickness from submicrometer to several micrometers, and width from one micrometer to tens of micrometers.

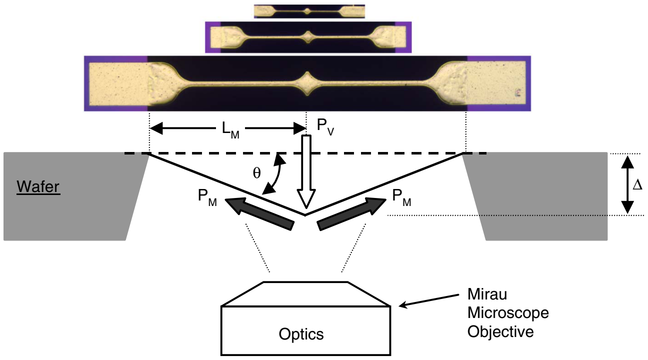

Figure 21. Side view of the MDE test showing vertical load being applied by the nanoindenter, P_V, the membrane in-plane load, P_M, and the position of the Mirau microscope objective. Reprinted with permission from [36], H. Espinosa et al., *J. Mech. Phys. Solids* (2003). © 2003, Elsevier Science.

The data directly obtained from the MDE test must then be reduced to arrive at a stress-strain signature for the membrane. The load in the plane of the membrane is found as a component of the vertical nanoindenter load by the equations

$$\tan\theta = \frac{\Delta}{L_M} \quad \text{and} \quad P_M = \frac{P_V}{2\sin\theta} \tag{17}$$

where (from Fig. 21) θ is the angle of deflection, Δ is the displacement, L_M is the membrane half-length, P_M is the load in the plane of the membrane, and P_V is the load measured by the nanoindenter. Once P_M is obtained the nominal stress, $\sigma(t)$, can be computed from

$$\sigma(t) = \frac{P_M}{A} \tag{18}$$

where A is the cross-sectional area of the membrane in the gauge region. The cross-sectional area dimensions are typically measured using AFM [37].

The interferometer yields vertical displacement information in the form of monochromatic images taken at periodic intervals. The relationship between the spacing between fringes, δ, is related through the wavelength of the monochromatic light used. Assuming that the membrane is deforming uniformly along its gauge length, the relative deflection between two points can be calculated, independently of the nanoindenter measurements, by counting the total number of fringes and multiplying by $\lambda/2$. Normally, part of the membrane is out of the focal plane and thus all fringes cannot be counted. By finding the average distance between the number of fringes that are in the focal plane of the interferometer, an overall strain, $\varepsilon(t)$, for the membrane can be computed from the following relation:

$$\varepsilon(t) = \frac{\sqrt{\delta^2 + (\lambda/2)^2}}{\delta} - 1 \tag{19}$$

This relationship is valid when deflections and angles are small. Large angles require a more comprehensive relation to account for the additional path length due to reflection off of the deflected membrane. This task and further details are given by Espinosa et al. [37].

The interferometer allows for *in-situ* monitoring of the test optically. Figure 22 shows combined interferometric images and stress-strain plots obtained from a typical membrane deflection experiment. The figure shows three instances of stress in stretching a thin gold strip obtained from the test. The first is at zero stretch and the second is at an intermediate stretch where the elastic–plastic behavior transition is exceeded and the strip is being permanently deformed. The third is at a large stretch and shows large local deformation indicating the strip is near failure. Data from MDE tests of thin gold, copper, and aluminum membranes have indeed shown that strong size effects exist in the absence of strain gradients [36].

Recently, the membrane deflection experiment was extended to measure fracture toughness of freestanding films [127]. In this method, two symmetric edge cracks are machined using a focused ion beam. A tip radius of 100 nm is achieved; see Figure 23. The toughness is computed from the equations

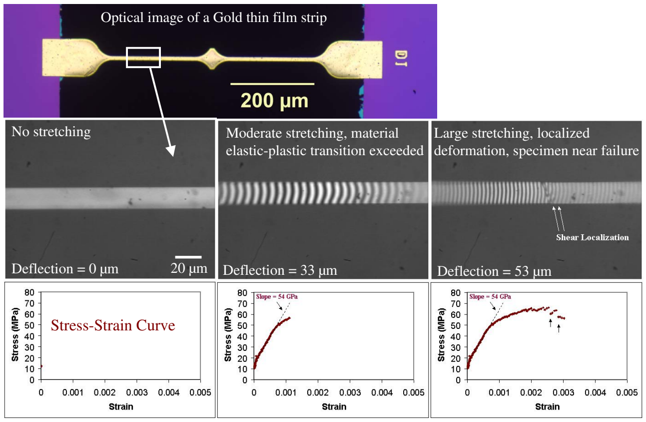

Figure 22. Magnified area of a thin gold membrane as it is stretched until it breaks. Three time points of stretching are shown that include the interferometric displacement image and the resulting stress–strain curve. Reprinted with permission from [36], H. Espinosa et al., *J. Mech. Phys. Solids* (2003). © 2003, Elsevier Science.

$$K_{IC} = \sigma_f \sqrt{\pi a} f\left(\frac{a}{W}\right) \tag{20}$$

$$f\left(\frac{a}{W}\right) = 1.12 + 0.429\left(\frac{a}{W}\right) - 4.78\left(\frac{a}{W}\right)^2 + 15.44\left(\frac{a}{W}\right)^3 \tag{21}$$

where σ_f is the fracture stress, a is the length of the crack, and W is the width of the gauge region as shown in Figure 23c.

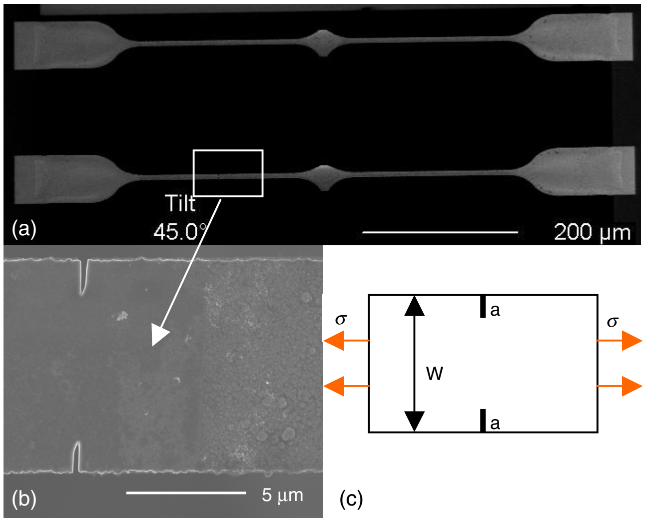

Figure 23. (a) A scanning electron micrograph of the geometry of the UNCD membranes, (b) a magnified area of the edge cracks, and (c) the schematic drawing of the two-symmetric-edge cracks model.

2.1.4. Testing Methods Based on Microelectromechanical System Technology

Microelectromechanical systems can be advantageously employed in the testing of micro- and nanoscale specimens. These devices consist of micromachined elements such as comb-drive actuators and strain sensors that are integrated components on the wafer. They have the potential to impact the small-scale testing field through high resolution force and displacement measurements. Several possibilities for actuation and deformation measurement exist. The methology is based on the fabrication of numerous specimens of identical geometry and microstructure through standard micromachining techniques.

A promising MEMS-based testing approach has been developed by Saif et al. [128–132]. A single crystal micromachined structure is used for stressing submicrometer thin films. *In-situ* SEM or TEM can be performed using this structure; see Figure 24. One end of the structure is attached to a bulk piezoelectric actuator while the other end is fixed. Folded and supporting beams are employed to uniformly transfer the load to the specimen, which is attached to a supporting fixed–fixed beam. This beam, of known spring constant, is then used as the load sensor. Two displacement elements are placed at either end of the specimen where the magnitude of displacement is imaged directly from the separation of beam elements. An innovative feature of the design is that the supporting beam structure is configured such that it can compensate and translate nonuniaxial loads into direct tensile loads on the specimen. In other words, the piezoelectric actuator is not required to pull on the structure exactly in a direction aligned with the specimen, thus solving the difficult issue of loading device–specimen alignment.

Another MEMS-based testing approach employs a comb-drive actuator to achieve time dependent stressing of the specimen through voltage modulation [133–139]. The device architecture consists of the microscale specimen with one end attached to a rigid mount and the other to a large perforated plate, which sweeps in an arc-like fashion when driven electrostatically by a comb-drive actuator (see Fig. 25). The resulting motion of the structure is recorded capacitively by the comb-drive sensor on the opposite side. The result is mode I stress concentration at the specimen notch. The specimen is tested until failure occurs and yields fracture and fatigue information about the material. Further details can be found in the cited literature.

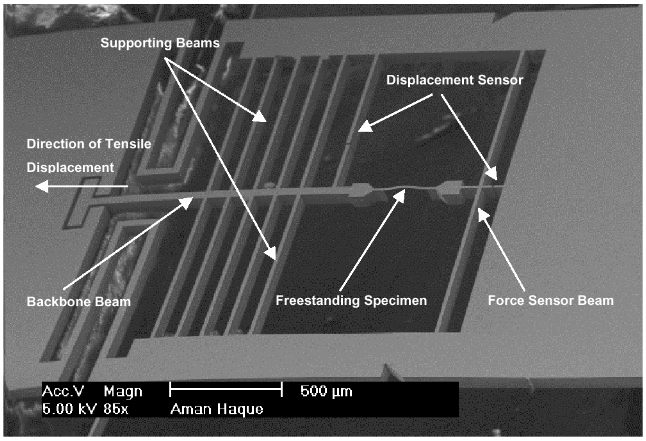

Figure 24. A SEM micrograph of the tensile test chip can be performed *in-situ* inside a SEM or TEM. The freestanding specimen is cofabricated with force and displacement sensors by microelectronic fabrication. Reprinted with permission from [132], M. A. Hague and M. T. A. Saif, in "Proc. of the SEM Ann. Conf. on Exp. and Appl. Mech.," Milwaukee, WI, (2002). © 2002, Society for Experimental Mechanics, Inc.

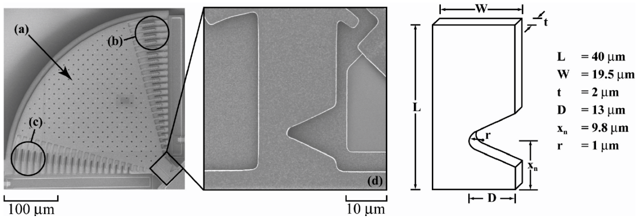

Figure 25. SEM micrographs of the fatigue test structure; (a) mass, (b) comb-drive actuator, (c) capacitive displacement sensor, and (d) notched cantilever beam specimen are shown. The nominal dimensions of the specimen are as indicated in the schematic. Reprinted with permission from [137], C. L. Mohlstein et al., *Mater. Res. Soc. Symp. Proc.* 687 (2002). © 2002, Materials Research Society.

Other MEMS techniques have also employed electrostatically driven comb-drives to perform other types of loadings. One such approach studied the effect of microstructure on fracture toughness through controlled crack propagation [140, 141]. The testing rig consists of a specimen anchored to a rigid support at one end and linked perpendicularly to a comb-drive actuator. The other end is attached to a beam that connects to a comb-drive actuator (see Fig. 26). A notch is either micromachined into the specimen (blunt notch) or a crack is propagated into the specimen through a Vickers microindent made in close proximity to the specimen. This step is performed as an intermediate step during the microfabrication of the specimen. The cracks, which radiate from the indent corners, travel into the specimen. Upon actuation of the comb-drive, the connecting beam applies mode I

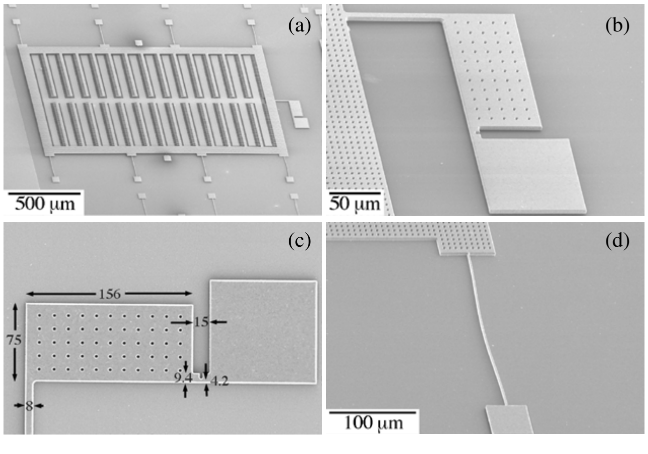

Figure 26. SEM images a MEMS fracture device. (a) is the overall device architecture, (b) is a close-up of the specimen, (c) gives the relative dimensions, and (d) shows a buckled support beam, a problem stemming from residual stress during fabrication that plagues many MEMS devices. Image courtesy of R. Ballerini.

loading at the specimen notch or sharp crack. At a critical value of displacement, controlled fracture is attained.

Another MEMS-based technique utilizes electrothermal actuation to load specimens in direct tension [142, 143]. The device is designed such that slanted or axial beams impose a deformation on the sample (see Fig. 27). The produced Joule effect causes local heating and expansion of the beams. The thermal actuator pulls directly on the specimen, stressing it in uniform tension. Strain is determined from an integrated capacitive sensor and verified through digital image correlation. The rig can also be employed for fatigue testing by using a modulated voltage. However, thermal actuation is hindered by a relatively slow response time.

These MEMS techniques show great promise to test ever-smaller specimens and are expected to have a great impact on the development of nanoscale devices. When coupled with finite element multiphysics modeling they should be able to provide an accurate description of nanoscale structural response and associated features needed to predict their behavior. These data are important for exploiting micro- and nanoscale properties in the design of novel and reliable devices with increased functionality.

2.2. Nanoscale Measurement Techniques

The property measurement of one-dimensional nano-objects, such as nanowires (NWs) and CNTs, is extremely challenging because of the miniscule size. As such, early studies of their mechanical properties focused on theoretical analyses and numerical simulations. They allowed the prediction of Young's modulus, buckling and local deformation, and tensile strength [144–147]. Owing to advances in microscopy, especially scanning probe microscopy (SPM) and electron microscopy, nanoscale experiments employing these tools have been developed. The main challenges in the experimental study of one-dimensional nanosize specimens are: (1) constructing appropriate tools to manipulate and position specimens; (2) applying and precisely measuring forces in the nano-Newton range, and (3) measuring local mechanical deformation precisely. In the next sections, we review techniques and methodologies addressing these challenges.

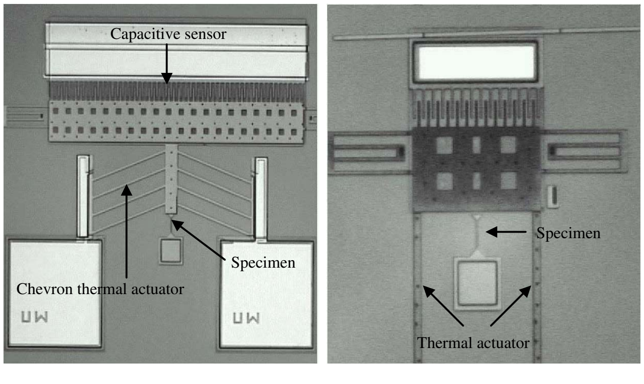

Figure 27. Micromechanical fatigue testers with: (a) an eight-beam chevron actuator and (b) a two-beam actuator. Reprinted with permission from [142], E. E. Fischer and P. E. Labossiere, in "Proc. of the SEM Ann. Conf. on Exp. and Appl. Mech.," Milwaukee, WI, 2002. © 2002, Society for Experimental Mechanics, Inc.

2.2.1. Manipulation and Positioning of Nanotubes

There are several methods used today to synthesize CNTs including electric arc-discharge [148, 149], laser ablation [150], and catalytic chemical vapor deposition [151]. CNTs made by these methods are commercially available, although still very expensive. During synthesis, nanotubes are usually mixed with residues including various types of carbon particles. For applications or tests, a purification process is required in most cases. In the most common approach, nanotubes are ultrasonically dispersed in a liquid (e.g., isopropanol) and the suspension is centrifuged to remove large particles. Other methods including dielectriphoretic separation are being developed to provide improved yield.

Random Dispersion Random dispersion is the easiest method for most of the mechanical testing experiments to date, but it is only modestly effective. After purification, a small aliquot of the nanotube suspension is dropped onto a substrate. The result is CNTs randomly dispersed on the substrate. A metal layer is then uniformly deposited on top of the substrate and patterned by a photolithography process, after which some of the nanotubes become pinned by a grid of pads [152]. To improve the probability of nanotube coverage, CNTs on the substrate are imaged inside a scanning electron microscope and then this image is digitized and imported to the mask drawing software, where the mask for the subsequent electron beam lithography (EBL) is designed. In the mask layout, the pads are designed to superimpose over the CNTs [153]. This process requires an alignment capability of lithography with a resolution of 0.1 μm or better.

Nanomanipulation SPM can be used both to image and to manipulate carbon nanotubes [154]. Using AFM, an individual multiwalled carbon nanotube (MWCNT) was successfully isolated from a group of overlapped MWCNTs. A "NanoManipulator" AFM system, comprising an advanced visual interface, teleoperation capabilities for manual control of the AFM tip, and tactile presentation of the AFM data, was developed at the University of North Carolina [155–157]. The NanoManipulator can take control of the AFM's probe, move it to the desired location, and manipulate atomic-scale structures. A software program integrates force feedback and AFM. A haptic interface, which is a penlike device, enables the users to remotely operate the NanoManipulator. More recently, they combined AFM, SEM, and the NanoManipulator interface to produce a manipulation system with simultaneous microscopy imaging [294].

Electron microscopy provides the imaging capability for manipulation of CNTs and NWs with nanometer resolution. Various sophisticated nanomanipulators under either SEM [294, 158, 159] or TEM [160–163] have been developed. These manipulators are usually composed of both a coarse micrometer-resolution translation stage and a fine nanometer-resolution translation stage; the latter is based on piezo-driven mechanisms. The manipulators have the capability of motion in three linear degrees of freedom, and some even have rotational capabilities. Several probes are attached to the manipulator and can be operated independently. In general, the manipulation and positioning of nanotubes is accomplished in the following manner: (1) a source of nanotubes is positioned close to the manipulator inside the microscope; (2) the manipulator probe is moved close to the nanotubes under visual surveillance of the microscope monitor until a protruding nanotube is attracted to the manipulator due to either van der Waals forces or electrostatic forces; (3) the free end of the attracted nanotube is positioned in contact with the probe and is "spot welded" by the electron beam [164]; (4) the other end of the nanotube is placed at the desired location and "spot welded." Nanodevices can be made using this approach. The technique is being implemented with force feedback for haptic control. Limitations in perception depth are so alleviated [155, 159].

External Field Alignment Dc and ac/dc electric fields have been used for the alignment of CNTs and nanoparticles [165, 166, 301]. Microfabricated electrodes are typically used to create an electric field in the gap between them. A droplet containing CNTs in suspension is dispensed into the gap with a micropipette. The applied electric field aligns the nanotubes, due to the dielectrophoresis effect, which results in the bridging of the electrodes by a single nanotube. The voltage drop that arises when the circuit is closed (dc component) ensures the manipulation of a single nanotube. Dc/ac fields have been successfully used in the manipulation of nanowires [167], nanotubes [165, 295], and bioparticles [168–170].

Huang [171] demonstrated another method of aligning nanotubes. A laminar flow was employed to achieve preferential orientation of nanotubes on chemically patterned surfaces. This method was successfully used in the alignment of silicon nanowires. Magnetic fields have also been used to align carbon nanotubes [172].

Direct Growth Instead of manipulating and aligning CNTs after their manufacturing, researchers have also examined methods for controlled direct growth. Huang et al. [173] used the microcontact printing technique to directly grow aligned nanotubes vertically. Dai et al. [174, 298–300] reported several patterned growth approaches developed in their group. The idea is to pattern the catalyst in an arrayed fashion and control the growth of CNTs from specific catalytic sites. The author successfully carried out patterned growth of both MWCNTs and single-walled carbon nanotubes (SWCNTs) and exploited methods including self-assembly and external electric field control.

Nanomachining It is of scientific interest to open the cap of MWCNTs to investigate the nanotube inner structure and intershell frictional behavior. Cumings and Zettl [253] have implemented an electric sharpening method to open the ends of MWCNTs using TEM. The process involves the electrically driven vaporization of successive outer layers from the end of the MWCNT, leaving the nanotube core intact and protruding from the bulk of the nanotube. This peeling and sharpening process can be applied repeatedly to the same multiwalled nanotube until the innermost tube protrudes, with a tip having a radius of curvature comparable to that of a single-walled nanotube.

2.2.2. High Resolution Force and Displacement Measurements

SEM, TEM, and SPM have been widely used in characterizing nanotubes. These provide effective ways of measuring dimension and deformation of nanotubes with nanometer resolution. Electron microscopy uses high-energy electron beams for scattering (SEM) and diffraction (TEM). Field emission gun SEM has a resolution of about 1 nm and TEM is capable of achieving a point-to-point resolution of 0.1–0.2 nm. The resolution of SEM is limited by the interaction volume between the electron beam and the sample surface. The resolution of TEM is limited by the spread in energy of the electron beam and the quality of the microscope optics.

AFM has become a powerful tool in the characterization of CNTs due to its capability not only to map the surface topography with nanometer resolution but also to manipulate CNTs. AFM can be operated in several modes: contact mode, tapping mode (or force modulation mode), noncontact mode, and lateral force mode [176–180]. The tapping mode has been used to induce radial deformation of nanotubes in addition to the contact mode and the lateral force mode [154, 181]. Scanning tunneling microscopy (STM) has not been widely used in the mechanical testing of CNTs at this stage, but it shows enormous potential since it can reveal the atomic structure and the electronic properties of CNTs [154]. The STM can be operated in two modes: constant current mode and constant height mode. Figure 28 provides several typical images taken by SEM, TEM, AFM, and STM.

Commercial force sensors usually cannot reach nano-Newton resolution. Therefore, AFM cantilevers have been effectively employed as force sensors [164, 187, 188], provided that their spring constant has been accurately calibrated. Alternatively, MEMS technology offers the capability to measure force with nano-Newton resolution. This point will be further discussed in Section 2.3.

To date, the experimental techniques employed in the mechanical testing of nanotubes can be grouped into five categories: resonance, bending, radial, tensile, and torsion loading.

2.2.3. Measurement Techniques for Nanotubes and Nanowires

Resonance Treacy et al. [184] estimated the Young's modulus of MWCNTs by measuring the amplitude of their thermal vibrations during *in-situ* TEM imaging (Fig. 29). The nanotubes were attached to the edge of a hole in 3-mm-diameter nickel rings for TEM observation, with one end clamped and the other free. The TEM images were blurred at the free ends, and increasing specimen temperature significantly increased the blurring. This indicated that the vibration was of thermal origin. Blurring occurs because the vibration cycle is much shorter than the integration time needed for capturing the TEM image.

A nanotube can be considered as a homogeneous cylindrical cantilever of length L with outer and inner radii a

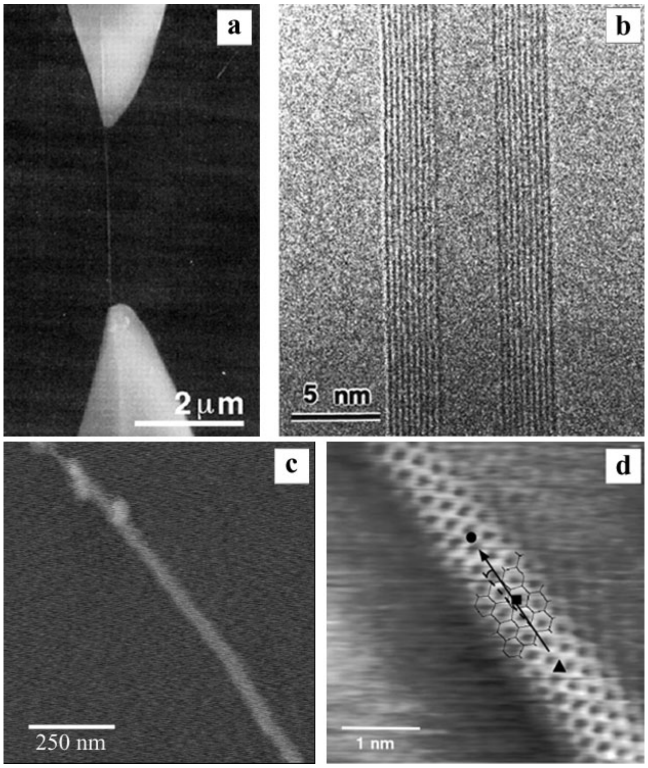

Figure 28. Typical images of CNTs taken by (a) SEM (reprinted with permission from [164], M. F. Yu et al., *Science* 287, 637 (2000). © 2000, American Association for the Advancement of Science.); (b) TEM (reprinted with permission from [293], R. H. Baughman et al., *Science* 297, 787 (2002). © 2002, American Association for the Advancement of Science); (c) AFM (image courtesy of C. Ke); and (d) STM (reprinted with permission from [183], T. W. Odom et al., *Nature* 391, 62 (1998). © 1998, Macmillan Publishers Ltd.). The imaging resolution of various instruments is illustrated.

and b, respectively. For such a structure, the square of the thermal vibration amplitude is given by

$$A^2 = \frac{16L^3kT}{E(a^4 - b^4)} \sum_j \beta_j^{-4} \approx 0.4243 \frac{L^3kT}{E(a^4 - b^4)} \tag{22}$$

where A is the amplitude at the free end, k is the Boltzmann constant, T is the temperature, E is Young's modulus, and β_j is a constant for free vibration mode n. By comparing the blurred images, one can estimate the vibration amplitude and deduce the value of Young's modulus.

This method is fairly simple to implement and exploits available instrumentation, including TEM holders with heating capability. As a matter of fact, this was one of the first experiments to measure Young's modulus of carbon nanotubes. There are some drawbacks associated with this method. Its accuracy to determine the vibration amplitude by comparing the blurred images is limited, the shape of the nanotubes is not exactly identical to a cylindrical cantilever, and the boundary conditions present some uncertainty. Krishnan et al. [185] later applied this method to SWCNTs.

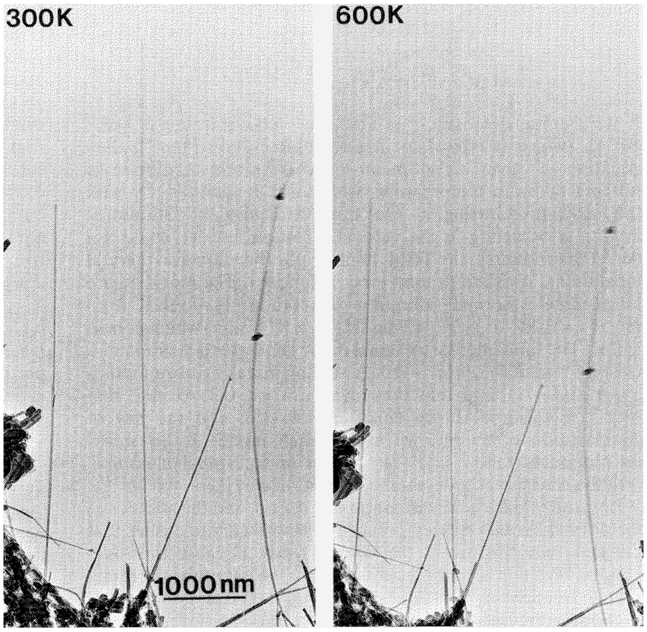

Figure 29. TEM micrographs showing the blurring at the tips due to thermal vibration at 300 and 600 K, respectively. Reprinted with permission from [184], M. M. J. Treacy et al., *Nature* 381, 678 (1996). © 1996, Macmillan Publishers Ltd.

Poncharal et al. [160] measured Young's modulus by using a method based on the mechanical resonance of cantilevered MWCNTs. The actuation was achieved utilizing an ac electrostatic field within a TEM (Fig. 30). In the experiment, the nanotubes were attached to a fine gold wire, on which a potential was applied. In order to precisely position the wire

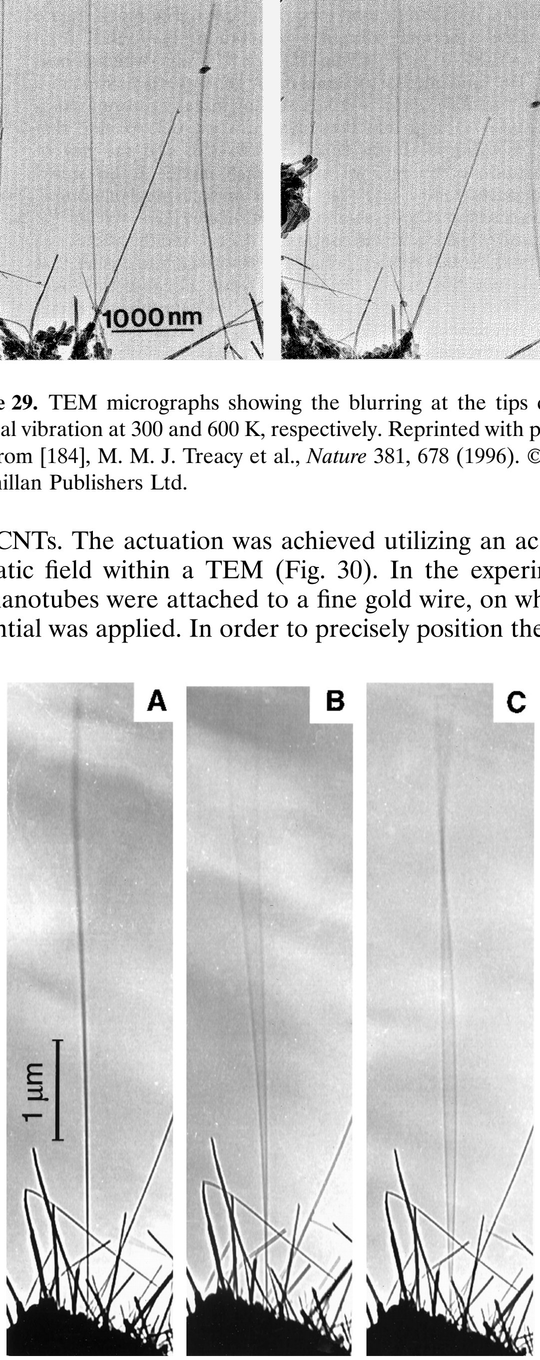

Figure 30. Dynamic responses to alternate applied potentials, (A) absence of a potential, (B) at fundamental mode, and (C) at second harmonic mode. Reprinted with permission from [160], P. Poncharal et al., *Science* 283, 1513 (1999). © 1999, American Association for the Advancement of Science.

near the grounded electrode, a special TEM holder with a piezo-driven translation stage and a micrometer-resolution translation stage was used. Application of an ac voltage to the nanotubes caused a time-dependent deflection. The resonant frequencies were then related to Young's modulus, viz.,

$$\nu_j = \frac{\beta_j^2}{8\pi}\frac{1}{L^2}\sqrt{(a^2+b^2)}\sqrt{\frac{E}{\rho}} \tag{23}$$

where a is the outer diameter, b is the inner diameter, E is the elastic modulus, ρ is the density, and β_j is a constant for the j harmonic. The elastic modulus can then be estimated from the observed resonance frequencies. This method requires the precise positioning of the nanotubes against the counterelectrode, which can only be achieved by a high-precision manipulator. The advantage is that the resonance frequency can be much more precisely measured than the vibration amplitude.

Bending and Curvature Falvo et al. [156] used AFM in contact mode to manipulate and bend a MWCNT resting on a substrate with the assistance of a nanomanipulator. The AFM tip was used to apply lateral force at locations along the tube to produce translation and bending. One end of the nanotube was pinned to the substrate by e-beam carbon deposition. After the bending, some of the deformed nanotubes were fixed by the friction between the nanotubes and the substrate and some returned to the undeformed configuration. Falvo et al. [157] applied this method to investigate the rolling and sliding behaviors of nanotubes.

Wong et al. [152] measured Young's modulus, strength, and toughness of MWCNTs by using AFM in lateral force mode (Fig. 31). In their method, nanotubes were dispersed randomly on a flat surface and pinned to this substrate by means of microfabricated patches. Then AFM was used to bend the cantilevered nanotubes transversely. At a certain location (x) along the length of each nanotube, the force versus deflection (F–d) curve was recorded to obtain the spring constant of the system. Multiple F–d curves were recorded at various locations along the nanotube. Single crystal MoS_2 was used as the substrate due to its low friction coefficient. By modeling the nanotube as a beam, the F–d data acquired by this method were used to estimate Young's modulus. In Figure 31e, the response of a beam to a force P applied at a distance a (along the x axis) from the fixed point ($x = 0$) is schematically illustrated. The governing equation for the elastic curve is

$$EI\frac{d^4y}{dx^4} = -f + P\delta(x-a) \tag{24}$$

where y is the deflection, I is the moment of inertia of the nanotube, and f is the friction force between nanotube and substrate. This term was considered small and omitted in the analysis. By integrating this equation and defining the spring constant at position x as $k(x) = dP/dy$, one can express it in terms of Young's modulus and tube geometry, viz.,

$$k(x) = \frac{3\pi r^4}{4x^3}E \tag{25}$$

where $\pi r^4/4$ is the moment of inertia for a solid cylinder of radius r.

Bending of nanotubes resting on a substrate is straightforward to implement. Nevertheless, it cannot eliminate the effect of adhesion and friction from the substrate. To solve the friction issue, Walters et al. [186] suspended the nanotube over a microfabricated trench and bent the nanotube repeatedly in lateral force mode. Salvetat et al. [187, 188] introduced a similar method to measure Young's modulus of SWCNTs and MWCNTs. The nanotubes were dispersed in ethanol and a droplet was deposited on a commercially available alumina ultrafiltration membrane with 200 nm pores (Whatman Anodics). Some nanotubes were suspended over the pores. The adhesion between the nanotubes and the membrane was found sufficiently strong, so that the nanotubes were effectively clamped. Using AFM in contact mode, the authors applied vertical load to the suspended nanotubes and recorded the force and deflection simultaneously. In this case, the nanotubes behaved like clamped beams subjected to a concentrated load.

Radial Compression Shen et al. [154] performed an indentation test on MWCNTs using AFM. After separating the overlapped nanotubes using AFM in indentation/scratch mode, the authors used AFM in tapping mode to scan the tubes and selected a well-shaped tube to perform further testing. The sample stage was lifted against the AFM tip. After the tube made contact with the tip, the AFM cantilever was bent and the tube was compressed. The cantilever bending changed the position of the laser spot on the four-quadrant photodectector and thereby produced a voltage signal proportional to it. When the signal reached a trigger value, the sample was retracted. The radial compression was obtained from the stage motion and cantilever deflection, and the force was calculated using the known spring constant of the AFM cantilever and its deflection. In summary, Shen et al. actually squeezed the nanotubes by moving them against the AFM cantilever, similar to nanoindentation. However, to study the same problem with the same tool, Yu et al. [181] took a different strategy. They compressed the nanotubes by AFM while imaging the nanotubes

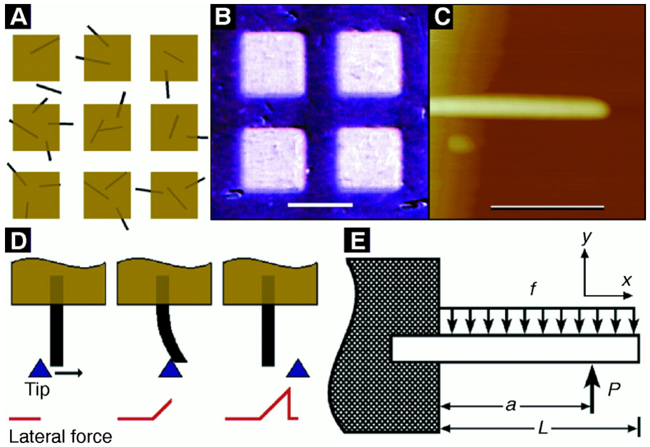

Figure 31. Overview of the approach used to probe mechanical properties of NRs and nanotubes. Reprinted with permission from [152], E. W. Wong et al., *Science* 277, 1971 (1997). © 1997, American Association for the Advancement of Science.

in tapping mode. In tapping-mode AFM, the cantilever was oscillated with amplitude A_0 above the surface. When scanning the sample, the tip struck the sample at the bottom of each oscillation cycle. Such intermittent contacts lead to a decrease of cantilever amplitude of value A. The set point S was defined as the ratio of A/A_0. From the value of the set point, the authors deduced the contact force.

Tensile Testing Tensile testing is the most widely used technique in macro- and microscale material characterization. In the testing of nano-objects, gripping and measuring force–displacement signatures is a major challenge. Direct stretch testing of nanotubes is hard to perform; however, ingenious experiments have been carried out.

Pan et al. [189] used a stress–strain rig to pull a very long (~2 mm) MWCNT rope containing tens of thousands of parallel tubes. They reported Young's modulus and tensile strength for this very long MWCNT. Yu et al. [164] conducted an *in-situ* SEM tensile testing of MWCNTs with the aid of a SEM nanomanipulator (Fig. 32). A single nanotube was clamped to the AFM tips by localized electron beam induced deposition of carbonaceous material inside the SEM chamber. The experiment setup consisted of three parts: a soft AFM probe (force constant less than 0.1 N/m) as a load sensor, a rigid AFM probe as an actuator, which was driven by a linear picomotor, and the nanotubes mounted between two AFM tips. Following the motion of the rigid cantilever, the soft cantilever was bent by the tensile load, equal to the force applied on the nanotube. The nanotube deformation was recorded by SEM imaging, and the force was measured by recording the deflection of the soft cantilever. The force–displacement signature was then converted to stress versus strain data, allowing modulus and strength of the MWCNTs to be measured. Yu et al. [296, 297] applied the same method to investigate the mechanical properties of ropes of SWCNTs, and the intershell friction of MWCNTs.

Cumings and Zettl [175] accomplished an *in-situ* TEM tensile testing of MWCNTs with the configuration shown schematically in Figure 33. A MWCNT was fixed at one end (Fig. 33a) and nanomachined at the other end to expose the inner tubes (Fig. 33b). A nanomanipulator was brought into contact with the core tubes and was spot-welded to the core by means of a short, controlled electrical current pulse (Fig. 33c). In Figure 33d and e two deformation modes are illustrated. In Figure 33d, the manipulator was moved right and left, thus telescoping the core out from or reinserting it into the outer housing of nanotube shells. The extraction and reinsertion process was repeated many times while being viewed at high TEM resolution to examine for atomic-scale nanotube surface wear and fatigue. In Figure 33e, the manipulator first telescoped the inner core out, then fully disengaged, which allowed the core to be drawn back into the outer shells by the intertube van der Waals force, consequently lowering the total system energy. A real-time video recording of the core bundle dynamics gave information pertaining to van der Waals and frictional forces between the tube shells.

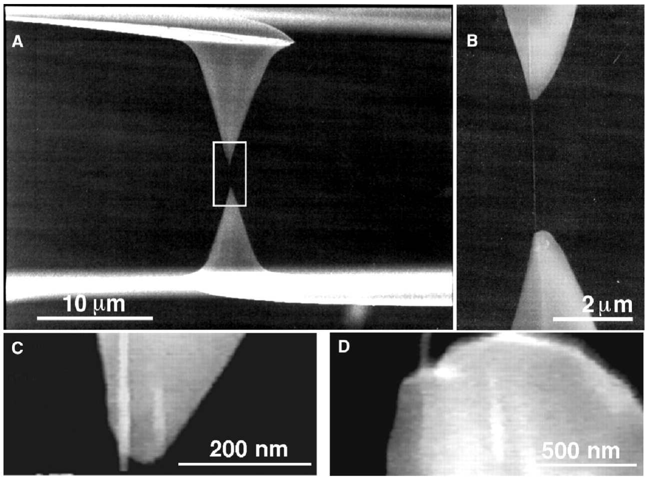

Figure 32. An individual MWNT mounted between two opposing AFM tips and stretched uniaxially by moving one tip. Reprinted with permission from [164], R. H. Baughman et al., *Science* 297, 787 (2002). © 2000, American Association for the Advancement of Science.

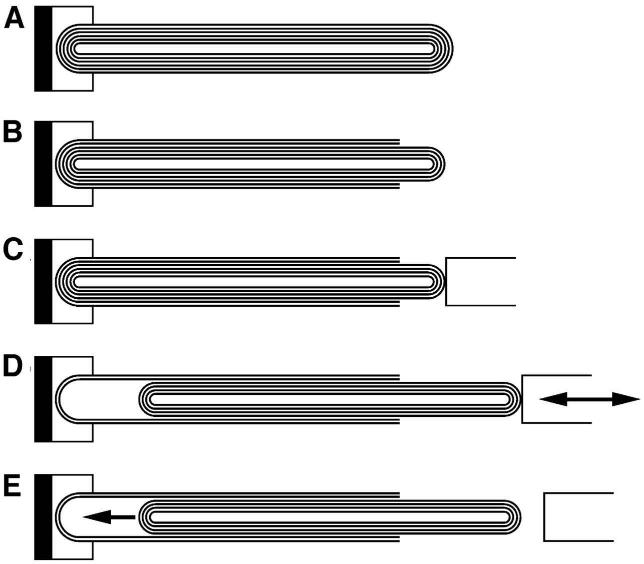

Figure 33. Schematic representation of the intershell experiments performed inside a TEM. Reprinted with permission from [175], J. Comings and A. Zettl, *Science* 289, 602 (2000). © 2000, American Association for the Advancement of Science.

Torsional Testing Williams et al. [153] recently introduced a microfabricated device which offers the capability to conduct torsion tests (Fig. 34). They used an advanced fabrication technique to make this task possible. They started with depositing metal pads by photolithography. Then, alignment marks were deposited on a substrate by EBL and lift-off. The dispersion of MWCNTs onto the surface followed. SEM images were taken to help determine accurate locations of the paddles. Then the underlying silicon oxide was etched to suspend the paddles. The suspended paddles were deflected with an AFM installed inside the SEM. The AFM/SEM setup allowed direct measurements of the applied force and the paddle deflection. Assuming there is no bending, one could calculate the torque and the corresponding rotation of the nanotube. This is an original method to perform torsion test of nanotubes. However, an apparent drawback is that the applied force by the

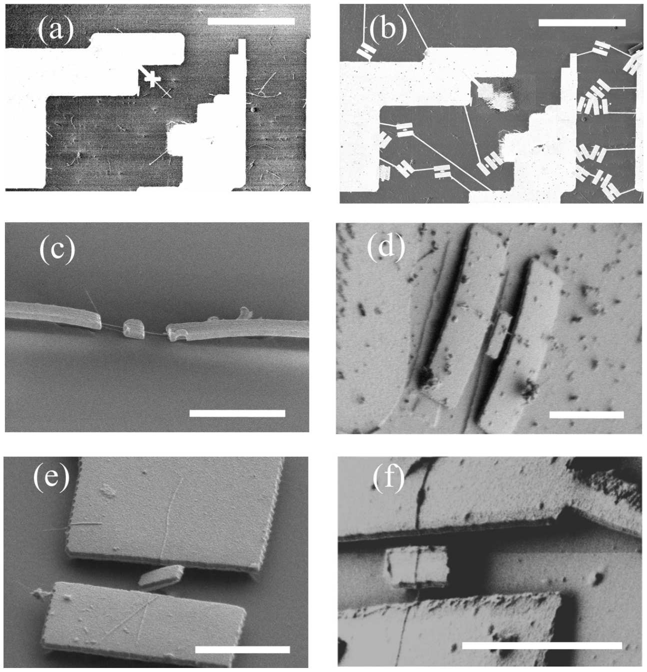

Figure 34. (a) Photolithographically patterned leads and EBL-patterned alignment marks (two crosshairs). (b) The same area with patterned paddles; the scale bars in (a) and (b) correspond to 40 μm. (c) The paddle touched the substrate due to the large curvature of the undercut metal leads. (d) Residual stress in the metal film and imperfect adhesion caused the leads to lift off the substrate. (e) One end of the paddle stuck to the substrate. (f) A Successfully suspended paddle. The scale bars in (c)–(f) correspond to 2 μm. Reprinted with permission from [153], P. A. Williams et al., *Appl. Phys. Lett.* 82, 805 (2003). © 2003, American Institute of Physics.

AFM introduces not only torsion but also bending of the nanotube.

2.3. Frontiers in Nanoscale Experimental Techniques

2.3.1. Limitations of Existing Techniques

Thin films have been studied with a variety of techniques including nanoindentation [15], tensile testing on millimeter and micrometer sized specimens [190–194], membrane deflection experiments [36–39, 84, 119], and *in-situ* high-resolution transmission electron microscopy (HRTEM) [195]. These techniques provided insight on various size scales including grain size effects and demonstrated that, in the case of metals, below a characteristic grain size, a transition occurs in the plastic deformation mechanism from intragranular dislocation motion to grain boundary sliding accompanied by substantial grain rotation and/or diffusion of clusters of vacancies. For the case of gold films, a grain size of 25 nm was identified as the characteristic size at which the transition is observed [195]. It should be noted that *in-situ* HRTEM findings are preliminary and that much work lays ahead. Despite these important advances, one can highlight the following limitations:

- In the case of nanoindentation and most microtensile testing of small samples, the defects responsible for the material deformation mechanisms are not imaged at the nanoscale at various loading states. Postmortem studies are conducted after unloading and further specimen micromachining.
- In the case of *in-situ* HRTEM, the current loading stages can only apply a prescribed displacement and thus do not possess the capabilities for independently measuring loads with adequate resolution. Hence the observed deformations are not accurately correlated with loading history. One exception is the MEMS-based stage being developed by Haque and Saif [131, 132].
- In the case of functional or intelligent materials, the current experimental setups do not have the electrodes and architecture needed for investigating electrical properties under stress (i.e., electromechanical coupling).

Single walled and multiwalled carbon nanotubes have been studied experimentally by means of AFM, SEM, and TEM. *A major issue in all of these studies is the scatter of the data*. For instance Young's modulus may present a scatter of more than 100%; failure strains are much smaller than the strain predicted by means of MD calculations [44]. The mechanics community has a special interest in assessing possible sources of errors and limitations of developed techniques. Among the most obvious, one can mention:

- They do not *directly and independently* measure load and deformation, as is the case in larger scale experiments. In fact, beam or string mechanics is used to infer local deformations.
- They assume homogeneous deformations because they cannot identify CNT atomic defects and monitor their evolution.
- Some use the same AFM tip to image and load the CNTs. As a result, imaging under loading is not possible.
- They cannot sense local deformations at attachment or loading points and therefore premature failure due to local deformations is not identified nor quantified.
- Most experimental configurations cannot measure specimen electronic properties under well-defined loading conditions.

New measurement tools, which can be integrated into high-resolution imaging instruments, are necessary in order to make further advances in the mechanics of CNTs, NWs, single crystal films, and polycrystalline films. MEMS technology offers unique features such as generation of micro-Newton load and nanometer displacement measurements with high resolution. It also provides the means to bridge size scales across several orders of magnitude as needed to investigate nano-objects.

2.3.2. A Novel MEMS Approach for In-situ Electron and Probe Microscopy

In order to overcome the aforementioned limitations, Espinosa and co-workers [196, 197] developed a new experimental setup for the testing of thin films, nanowires, and nanotubes. The setup is an integrated MEMS device consisting of three well-defined components: an actuator, a specimen, and load sensor; see Figures 35. For the testing of thin films, the setup consists of a thermal actuator, a specimen, and a load sensor based on differential capacitance measurement. Thermal actuators have been used in the past to produce up to several milli-Newton forces. In the device shown in Figure 35a, a set of slanted beams connected to a trunk provides the actuation when a current is circulated between the fixed pads. Thermal expansion of the doped polysilicon beams results in a displacement of the trunk and, consequently, the loading of the sample [142]. The device works in displacement control, which is very advantageous in the study of thin films.

Sensors based on differential capacitance measurements are well established (e.g., Analog Devices' and Motorola's MEMS accelerometers). In this approach, the differential capacitor serves as a load sensor upon proper calibration. A readout chip, manufactured by Microsensors Co. [198], is being employed to measure differential capacitance with femtofarad resolution. The chip suppresses parasitic capacitance and provides adjustable internal capacitors to select range and resolution. Here the concept of a two-chip system, a MEMS chip for sample loading and another complementary metal oxide semiconductor chip for capacitance measurement, is employed; see Figure 35c. The movement of the movable electrode is equal to the deformation of the folded beams in the axial direction. Capacitance change is proportional to the displacement of the movable electrode when such displacement is sufficiently small [198]. If a voltage bias V_0 is applied on each fixed electrode there will be a voltage change in the moving electrode, V_{sense}, given as

$$\frac{V_{\text{sense}}}{V_0} = \frac{\Delta d}{d} + o\left(\frac{\Delta d}{d}\right)^3 \tag{26}$$

where d is the gap between movable and fixed electrodes, Δd is the movable electrode displacement in the axial direction, and V_0 is the bias voltage. If Δd is much smaller than the gap d, V_{sense} is proportional to Δd. When the spring constant of the folded beams is characterized, the force applied on the load cell is proportional to V_{sense}. Measurements of specimen deformation are achieved by *in-situ* microscopy. Direct measurement of local displacements and strains is very important. It is known that peculiarities observed in the elastic, plastic, fracture, and transport properties of thin films are directly related to atomic structure and associated defects. This point is addressed further later.

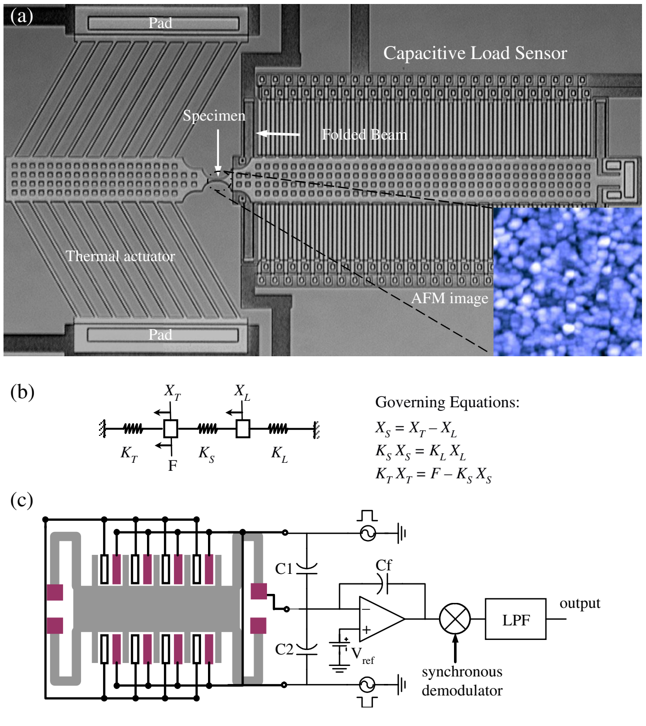

Figure 35. (a) MEMS device for *in-situ* AFM/SEM/TEM electromechanical characterization of polycrystalline nanoaggregates films. The whole system can fit in a 3 mm × 3 mm area. (b) Lumped model of the device shown in (a), where X_S is the deformation of the specimen, X_L is the displacement of the load sensor, X_T is the displacement of the thermal actuator, K_S is the stiffness of the specimen, K_L is the stiffness of the load sensor, K_T the stiffness of the thermal actuator, and F is the total force generated by the thermal actuator. (c) Two-chip architecture used for measuring the load.

The lumped model of this device is shown in Figure 35b. Compatibility and equilibrium equations are also given in the figure. To illustrate the approach, tensile testing of polysilicon film can be examined as an example for design purposes. Considering the failure strain of polysilicon is about 1% [117], the required force from the thermal actuator to break the polysilicon specimen was calculated. The structure of the thermal actuator (e.g., number of slanted beams and geometry of each beam) was then designed after thermal analysis [199, 302]. These estimates were also verified using ANSYS multiphysics (from ANSYS Inc.). They show that the polysilicon specimen can be deformed to failure and that the resolution of a differential plate capacitor can be used to measure the load sensor motion.

For the case of CNT testing, the experimental setup is similar to that of thin film testing. One difference is that a comb-drive actuator is used (force control) instead of a thermal actuator (Fig. 36). The force to break a CNT is only several micro-Newtons, which can be achieved by a comb-drive actuator. A comb-drive actuator can accommodate a several micrometers motion range, which is required to study the nanotribological behavior of MWCNTs after the outside shell failure. Due to the limitation in space we do not provide all the details of the lumped model analysis for this device; however, we just mention that the analysis is very similar to one previously discussed for the thermal actuator.

The 3D nanomanipulator shown in Figure 37 is used to mount the nanosize specimen between the comb-drive actuator and the capacitive load sensor (Fig. 36). Several imaging tools are employed to measure specimen deformation and to identify defect initiation and evolution. In the next section, we report displacement measurement performed by DIC of AFM images obtained at various deformation levels.

2.3.3. In-situ AFM Results

Using the MEMS device shown in Figure 35, testing of polysilicon thin films with *in-situ* AFM displacement and strain measurements of the specimens was performed. AFM was employed to scan the specimen surface before and after

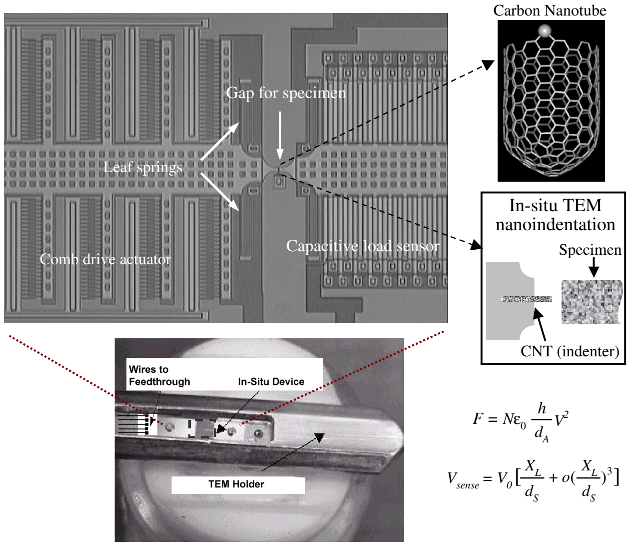

$$F = N\varepsilon_0 \frac{h}{d_A} V^2$$

$$V_{sense} = V_0 [\frac{X_L}{d_S} + o(\frac{X_L}{d_S})^3]$$

Figure 36. MEMS actuator for *in-situ* SEM/TEM/STM electromechanical characterization of carbon nanotubes. Various configurations will be investigated. The dimensions of the device will be such that the chip will fit in a TEM holder. Actuation and sensing pads will be wire bonded to a small breadboard and from there will be wired through the TEM holder feedthrough (see bottom image).

the loading. DIC was then used to process the AFM data to quantify the displacement/strain field. Figure 38a and b shows two AFM images of the specimen before and after loading [196, 197]. The first image was obtained before the application of a voltage to the thermal actuator, while the second image was obtained when a 5 V was applied. Figure 38c shows the displacement field obtained using DIC for a scanned area of 8 μm × 2 μm. The displacement contours show that the thermal actuator symmetrically stretched the specimen, in the x-direction, as expected. Moreover, the planarity of the device was investigated with an optical surface profiler and it turned out that the device was flat and parallel to the substrate within 40 nm.

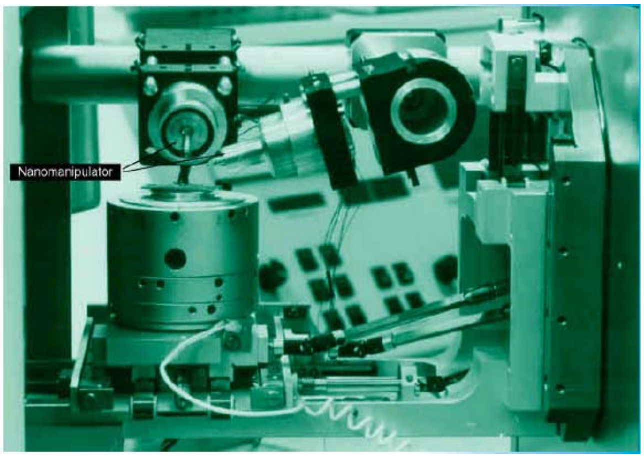

Figure 37. Klocke Nanotechnik nanomanipulator within a LEO field-emission SEM [159].

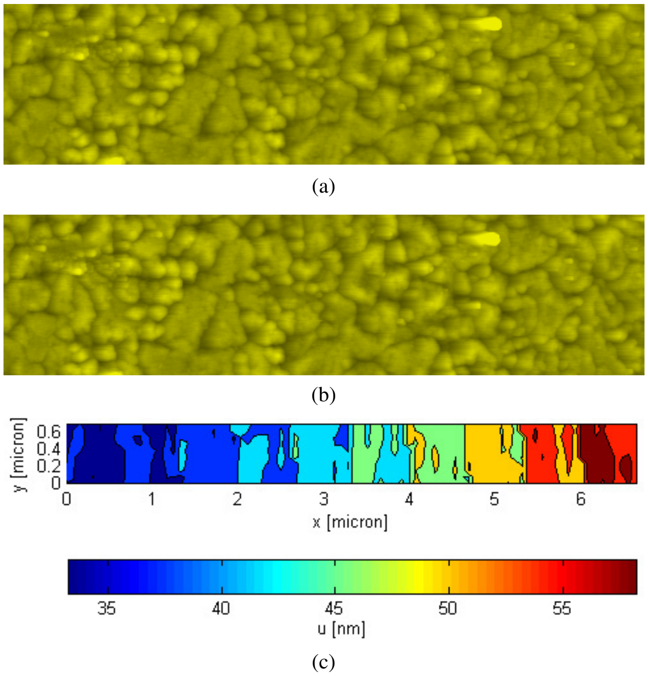

Figure 38. (a) AFM image of the topography of the specimen surface before loading. (b) AFM image during the loading. (c) Displacement contour computed by DIC within the area shown in (a) and (b). The load was applied in the x-direction. Reprinted with permission from [197], Y. Zhu et al., in "Proc. SEM Ann. Conf. Exper. Appl. Mech.," 2003. © 2003, Society for Experimental Mechanics, Inc.

2.3.4. Opportunities in Nanomechanical Imaging of Deformation

In this section we summarize efforts underway to elucidate deformation and failure mechanisms in thin films, nanowires, and nanotubes. Special emphasis is placed on techniques that are being used in conjunction with the MEMS setup discussed in the previous section.

In the investigation of thin films, extensive *in-situ* TEM work is essential to reveal the material behavior under stress at the grain level. Diffraction contrast and convergent beam electron diffraction at and around defects, with a beam diameter of a few angstroms, can be used to obtain lattice parameters and strain under load on ultrathin specimens. Higher order Laue zone line patterns can be compared to computer simulations of the deformed grains for this purpose. A critical aspect is the identification of dislocation sources and their densities, which are commonly assumed in atomistic, discrete dislocation, and other models.

Other TEM techniques such as weak-beam dark-field microscopy and Moire patterns for defect characterization are also possible. These techniques enhance the observation of defects such as dislocations, twins, and stacking faults on real space in real time. This effort is particularly relevant to assess the effectiveness of atomistic models in capturing defect distribution, annihilation, interaction with grain boundaries, and free surfaces. Defects sources, density, speed, and its relationship to material nanostructure and composition can also be quantified through this approach. Moreover, the onset of inelasticity and fracture characterization at the atomic level is also possible.

Stack and collaborators [161, 200, 201] have performed *in-situ* nanoindentation TEM studies by employing a TEM holder containing a piezo-actuator and a specially microfabricated wedge-shaped specimen. Observations of film deformation and nucleation of dislocations were observed in real time. Unfortunately, due to the hysterisis of the piezo-actuator and other experimental limitations, quantitative measurements of force–displacement were not possible. The MEMS device shown in Figure 36 may be one approach to overcome this limitation. Here the specimen is integrated to the load sensor during the microfabrication steps and a sharp indenter (e.g., a CNT) is mounted to the trunk of the MEMS thermal actuator using a 3D nanomanipulator (Klocke Nanotechnik Co.); see Figure 37. This 3D nanomanipulator has already been implemented for *in-situ* SEM site-specific nanowelding of carbon and other nanostructures [159].

Currently, the best TEM in the world has a point-to-point resolution of about 1 angstrom. It is anticipated that transmission electron microscopes will reach a resolution of subangstrom in the next few years by means of spherical and achromatic aberration corrections. This will make feasible the identification of *interatomic potentials* through atomic imaging of crystal planes. Using the device shown before, experiments performed on single crystal and bicrystal specimens could be employed to identify the interatomic potentials used in atomistic and molecular dynamic simulations. For particular crystal orientations, selected *a priori*, the atomic displacement field around a dislocation core or an interface could be mapped. HRTEM images of the crystal structure can be interpreted using software based on fast Fourier transform formalism and other approaches [202–204]. A cross-correlation technique can be used to assess the accuracy of the simulated images. This work would certainly constitute a milestone in materials research.

For the study of nanotubes and nanowires, TEM can provide information on chirality and other structural feature [205] but is unlikely to provide atomic images from which deformations can be computed. By contrast, ultravacuum STM has been successfully employed to obtain atomic images of CNTs [182, 183]. It remains to be determined if this imaging capability could be performed in combination with the MEMS device presented here. Capturing atomic structure under various loading degrees would be the ultimate goal in these studies.

Electromechanical properties of CNTs are of particular interest due to their potential in NEMS. Previous work by Tombler et al. [206] has shown that the conductivity of CNTs can change by several orders of magnitude when deformed by an AFM tip. The MEMS setup shown in Figure 36 has embedded interconnects and pads for electromechanical characterization of nanotubes under loading. By connecting the sensing pads to a signal analyzer, the electrical conductance can be measured under stress. Likewise, for the case of MWCNTs, sliding forces between outer and inner shells can be measured upon outer shell fracture. Therefore, on-chip nanoscale tribological properties can be identified with subnano-Newton force resolution and subnanometer displacement resolution. The main difference between previous work and the experimental approach here discussed is that forces and atomic displacement are measured independently and directly.

3. MICRO- AND NANOSCALE MEASURED MATERIAL PROPERTIES

Thin films have long been harvested by the microelectronics industry for their unique properties. Conventional thinking has usually categorized their electrical properties as the property of primary importance. In the past decade and a half though, other nonelectronic, chemical and mechanical properties have also been found to have great significance [15, 93]. Mechanical properties, in particular, are critical when one is concerned with the fact that devices must have structural integrity and also be reliable throughout their life expectancy.

Thin film materials that are widely used in microdevices include metallic, silicon-based, and carbon-based substances. As diverse as these materials are in the atoms that compose them so are their properties. Processing techniques and parameters for films are numerous and directly affect the film microstructure. It is not surprising then that films of the same material that are processed by different methods can have widely varying properties. The methods employed to measure the properties listed in this section also vary significantly and therefore so do data values as well.

This section is designed to introduce the reader to thin film properties that have been measured thus far. No contrasts or categorizations are made to separate how processing or test methods affect the measured data in most cases. The scientific community has not yet come to a consensus on a uniform testing and characterization methodology by which measurements can be made and classified in a uniform and reproducible manner. Much work lies ahead before thin film behaviors, such as size effects, are fully understood and before theories capable of predicting behavior are developed. It should be noted that a number of the references garnered for this section have been previously collected in a review by Sharpe [207] and readers are directed there for additional citations.

3.1. Metallic Materials

Metallic materials serve many engineering functions in microdevices including both electrical and mechanical components. Metals display a wide range of mechanical behavior including elasticity, plasticity, creep, fatigue, and fracture. Only in recent years has the mechanical behavior of thin film metals become of concern in the design of microdevices. Metal films have been found to be susceptible to electromigration and other diffusion driven processes, stress and defect formation due to thermal effects, and changes in electrical behavior due to straining. These processes have deleterious effects that often lead to device failure.

The more popular metals used in microdevices include gold, aluminum, copper, and nickel. These materials are mainly deposited by sputtering or electron-beam evaporation, processes that contain numerous parameters directly affecting microstructure. They are normally in polycrystalline form with grain size on the order of film thickness. They typically possess significant textures. Table 3 lists properties for the metals listed. With the exception of Au, Young's modulus of thin films mostly agrees with bulk polycrystalline values. Several materials showed increases in yield stress as specimen size decreased, as was previously shown for Au in Figure 5. In general, the yielding behavior of thin films tends to require larger stresses than their bulk counterparts. This is a topic of high interest to researchers and is currently a major research thrust toward the development of theories and models that can accurately predict their behavior.

3.2. Silicon-Based Materials

Most materials used in microdevices are silicon-based, which typically exhibit linear elastic behavior followed by brittle fracture. Silicon and silicon-based materials have been the dominant materials in the microelectronics revolution of the 20th century and the precursor to the microelectromechanical/nanoelectromechanical systems revolution currently underway. It has been the material of choice for current MEMS devices, mainly because devices can be fashioned using standard microfabrication techniques [215, 216]. The materials discussed in this section include single crystal silicon, polycrystalline silicon, silicon dioxide, silicon carbide, and silicon nitride.

Single crystal silicon has been a vehicle for the fabrication of microelectronics for several decades. It also serves as the most common structural material used in MEMS. Its electrical properties have been well characterized over the years; however, the mechanical properties, such as fatigue and fracture toughness, have only recently begun to be tackled. The mechanical properties measured thus far have been shown to be dependent on the micromachining process utilized to prepare specimens and their resulting surface conditions. The techniques employed to test single crystal specimens have been diverse and include many of the methods listed in the previous section. Table 4 provides a compilation of some results achieved over the past several years. Most of these results, in terms of Young's modulus, agree well with established benchmark values. Fracture strength varies considerably and is governed by the orientation of the crystal as well as the surface features particular to each micromachining process [217].

Polycrystalline silicon has become a commonly employed material in microdevices. It is normally employed as the structural part of the device due to its high melting point, ease of growth and micromachineability, and somewhat favorable mechanical behavior [219]. It also has the distinction of having appreciable piezoresistive behavior for the transduction of deflection or other electromechanical coupled variables. Polysilicon has been the focus of more thin film micromechanical properties measurements than any other material thus far. Table 5 lists the results from recent studies. A more complete list of experimental reports can be found in [207].

For the most part, it can be said that Young's modulus varies moderately between techniques. The same can be said for fracture strength when considering that it is a function of the surface flaws present. The effect of specimen size on fracture strength was extensively studied by Sharpe et al. [229] and Tsuchiya et al. [122]. These pioneering studies were able to show that as specimen size decreased, translating to a reduction in surface area, the fracture strength increased due to a lower population of surface flaws.

Silicon Oxide (SiO_2), nitride (Si_3N_4), and carbide (SiC), and combinations thereof, are silicon-based materials of growing importance in microdevices. They are less common than single or polycrystalline silicon as structural components due to residual stresses that develop during processing. Silicon dioxide and silicon nitride are commonly used as sacrificial layers, etch stops, or electrical/environmental passivation layers. Silicon nitride and silicon carbide are extensively used to make membranes for micropumps, pressure sensors, support for X-ray masks, etc. Table 6 lists a summary

Table 3. Summary of data on thin film metals.

Material	Young's modulus (GPa)	Yield strength (GPa)	Tensile strength (GPa)	Method	Ref.
Au-size effect	53–55	0.055–0.220	0.78–0.35	MDE	[36, 38]
Au	40–80	—	0.2–0.4	tension	[2]
Au	74	0.26	—	indentation	[77, 208]
Au	57	—	—	bending	[77, 208]
Al-size effect	65–70	0.150–0.180	0.240–0.375	MDE	[36]
Al	24.2–30.0	0.087–0.105	0.124–0.176	tension	[209]
Al	69	—	—	tension	[128]
Al	69–85	—	—	bending	[210]
Cu-size effect	125–129	0.200–0.345	0.45–0.80	MDE	[36]
Cu-size effect	120–132	0.120–0.480		tension	[211]
Cu	86–173	0.12–0.24	0.33–0.38	tension	[212]
Cu	108–145	—	—	indentation	[212]
Ni-thick	176 ± 30	0.32 ± 0.03	0.55	tension	[114]
Ni-thin	231 ± 12	1.55 ± 05	2.47 ± 0.07	tension	[213]
Ni-LIGA	181 ± 36	0.33 ± 0.03	0.44 ± 0.04	tension	[214]
Ni	156 ± 9	0.44 ± 0.03	—	tension	[212]

MDE = membrane deflection experiment.

Table 4. Summary of data on single crystal silicon.

Direction	Young's modulus (GPa)	Fracture strength (GPa)	Method	Ref.
⟨100⟩, ⟨110⟩, ⟨111⟩	130, 170, 185	—	benchmark	[86]
⟨100⟩	168	—	indentation	[218]
⟨100⟩ (doped Si)	60–200	—	indentation	[151, 219]
⟨110⟩	163–188	3.4	indentation, MCD	[208]
⟨110⟩	166–168	—	MCD	[84, 85]
⟨110⟩	177 ± 18	2.0–4.3	bending	[220]
⟨110⟩ (different fab.)	—	1.0–6.8	tension	[125]
⟨111⟩, ⟨110⟩	—	1.3, 2.3	tension	[221]
⟨110⟩	—	1.2	tension	[222]
⟨110⟩	150	0.3	tension	[223]
⟨110⟩	147	0.26–0.82	tension	[224]
⟨100⟩, ⟨110⟩, ⟨111⟩	125–180	1.3–2.1	tension	[225]
⟨100⟩	142 ± 9	1.73	tension	[213]
⟨110⟩	169.2 ± 3.5	0.6–1.2	tension	[226]
⟨100⟩, ⟨110⟩, ⟨111⟩	115–191	—	tension	[121]
⟨110⟩	—	8.5–20	torsion	[227]
	75 (shear)	—	torsion	[228]

MCD = microcantilever deflection.

of properties measured thus far. Silicon nitride and carbide both show future potential as mechanical components for microdevices due to their high Young's modulus. However, more extensive studies are required to understand how their thin film structure affects fracture strength, etc.

3.3. Carbon-Based Materials

Carbon in its various forms may become a key material for the manufacturing of MEMS/NEMS devices in the 21st century and will most probably displace silicon-based materials in devices. Carbon materials have exceptional and tailorable properties with the potential to meet the stringent demands that MEMS/NEMS devices and other thin film applications require. These include UNCD, diamond-like carbon, amorphous diamond, and carbon nanotubes. To date, the aggregate of testing performed on these materials is preliminary and much work is needed to confirm property measurements and comprehend their meaning.

Table 7 summarizes the current data on thin film diamond materials. The data are separated into four groups that include ultrananocrystalline diamond, nanograined diamond, micrograined diamond, and diamond-like carbon. Each of these materials is fabricated using varying processing schemes to achieve their microstructures with the resulting mechanical behavior being a function of these processes, microstructures, and bonding characteristics. Diamond materials typically have large elastic moduli reflective of their strong cohesive binding and, being brittle in nature, fail by means of crack propagation initiated at flaw sites. The UNCD and micro- and nanograined materials all yield large elastic moduli since they are composed of crystalline grains. Diamond-like carbon is described as having an amorphous structure consisting of a mixture of sp^2 and sp^3 bonding from both graphite and diamond bonding and therefore possessing a lower elastic modulus.

Fracture strength has only recently been measured; results are listed in Table 7. It varies from 0.55 to 5.03 GPa depending on the type of material and testing technique. A typical stress–strain result for a UNCD specimen is given in Figure 39. In the gauge region, the specimen was 10 μm wide and 0.5 μm thick. The membrane deflection experiment described in Section 4 was employed. The stress–strain response of the specimen increases in a linear fashion until

Table 5. Summary of data on polysilicon.

	Young's modulus (GPa)	Fracture strength (GPa)	Method	Ref.
MUMPs21	136–174	1.3–2.8	tensile	[112]
MUMPs19	132	—	tensile	[112]
Stress concentrations	—	1.3–1.5	tensile	[230]
Size effect	154.1–159.6	1.51–1.67	tensile	[229]
Size effect—doped	—	2.0–2.8	tensile	[122]
Microcantilever	174 ± 20	2.8 ± 0.5	bending	[231]
AFM deflection	173 ± 10	2.6 ± 0.4	bending	[232]
Bulk	181–203	—	indentation	[219]
Doped–undoped	95–175	—	indentation	[233]

Table 6. Summary of data on silicon-based materials.

Material	Young's modulus (GPa)	Fracture strength (GPa)	Method	Ref.
SiO_2	—	0.6–1.9	tension	[234]
SiO_2	83	—	bending	[77]
SiO_2	64	0.6	indentation	[77]
Si_3N_4	222 ± 3	—	bulge	[105]
Si_3N_4	216 ± 10	—	indentation	[105]
SiC	470 ± 10	—	bending	[235]
SiC	395	—	indentation	[236]

Table 7. Summary of data on thin film carbon-based materials.

Material	Young's modulus (GPa)	Fracture strength (GPa)	Method	Ref.
UNCD (nanoseeded)	945–963	3.95–5.03	MDE	[84]
UNCD (microseeded)	930–970	0.89–2.42	MDE	[84]
UNCD	916–959	—	MCD	[84]
UNCD	960	—	nanoindentation	[237]
Nanograined diamond	910–1150	—	nanoindentation	[238]
Nanograined diamond	675–765	—	indentation	[239]
Nanograined diamond	510	—	laser-acoustic	[240]
Micrograined diamond	1250	—	nanoindentation	[241]
Micrograined diamond	1155–1207	—	nanoindentation	[242]
Micrograined diamond	1000	—	indentation	[243]
Micrograined diamond	884–940	—	indentation	[239]
Micrograined diamond	830	2.72	MCD	[244]
Micrograined diamond	—	0.55–0.82	mode I	[245, 246]
Diamond-like carbon	800	0.7	nanoindentation	[247, 248]
Diamond-like carbon	700	—	laser-acoustic	[249]
Diamond-like carbon	—	0.8–1.0	three-point bend	[250]
Diamond-like carbon	260	—	indentation	[251]
Diamond-like carbon	60–145	—	nanoindentation	[252]

failure at 5.03 GPa. The slope of the plot represents the elastic modulus and was found to be 949 GPa.

It should also be mentioned that Table 7 contains data for a limited number of specimens of varying size and processing schemes and therefore effects of flaw size in relation to specimen size and processing are not defined. Fracture strengths of 0.7 to 5.03 GPa have been measured for UNCD films with the nanoseeded UNCD yielding by far the highest tensile strength [84, 85, 127].

Espinosa and co-workers have also interpreted the strength of UNCD based on Weibull statistics [127]. They showed that the Weibull parameters are highly dependent on the seeding process used in the growth of the films. When seeding was performed with micrometer size diamond particles, using mechanical polishing, the stress resulting in a probability of failure of 63% was found to be 1.74 GPa, and the Weibull modulus was 5.74. By contrast, when seeding was performed with nanosize diamond particles, using ultrasonic agitation, the stress resulting in a probability of failure of 63% increased to 4.13 GPa and the Weibull modulus was 10.76. The investigation highlights the role of microfabrication defects on material properties and reliability, as a function of seeding technique, when identical MPCVD chemistry is employed. This group is currently examining how strength is affected when specimen size is reduced to a degree where it becomes comparable to the flaw size. By employing the new membrane deflection toughness experiment developed by Espinosa and co-workers [127], the toughness of UNCD was measured to be approximately 7 MPam$^{1/2}$.

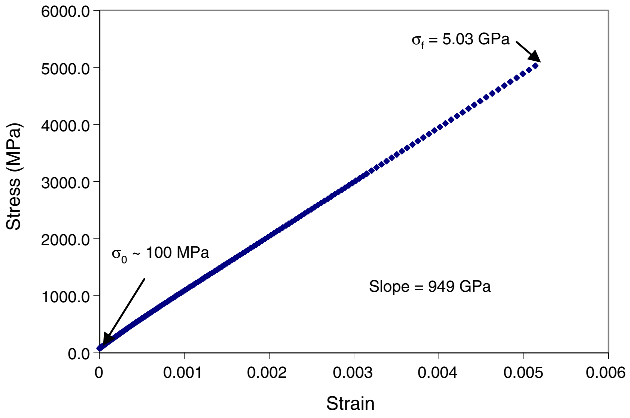

Figure 39. Stress–strain curve representative of a typical UNCD MDE sample. An elastic modulus of 949 GPa, fracture stress of 5.03 GPa, and an estimated initial stress of 100 MPa were identified. Reprinted with permission from [84], B. C. Prorok et al., *Exp. Mech.* (2003). © 2003, Society for Experimental Mechanics.

The results collected thus far demonstrate the significant mechanical advantages that carbon-based films can provide to MEMS/NEMS and their applications over other materials, particularly when extrinsic flaws such as pores and surface flaws can be further minimized and/or eliminated.

Clearly, much remains to be learned about the mechanical behavior of thin film materials. Researchers in the field must come to a consensus on a standard technique by which properties can be measured in an accurate and repeatable manner. Finally, the understanding of mechanisms involved in microstructural and specimen size effects as well as fracture and fatigue will allow the development of models capable of predicting film behavior.

3.3.1. Carbon Nanotubes

Most of the experimental techniques to date have been reviewed in this chapter. All have been performed to characterize the mechanical or related properties of carbon nanotubes. This section lists in tabular form the results of measurements of mechanical properties of MWCNTs and SWCNTs with focus on Young's modulus and strength. This section is intended to provide the reader not only values of mechanical properties but also the corresponding references and test methods employed in their identification.

Most of the experimental measurements were conducted on MWCNTs and ropes of SWCNTs, with only one exception, that of Krishnan et al. [185] who measured Young's modulus of SWCNTs using the thermal resonance method. There exists a wide range in the reported properties primarily owing not only to different synthesis methods but also to the various assumptions used in the calculations of stress and strain.

Presently, there are several debatable issues related to the interpretation of the data. One such issue is whether CNTs behave more like a beam or a string. Most experiments have modeled the nanotube as a beam and obtained the Young's modulus based on this assumption. A typical example is the measurement done by Wong et al. [152], which correlated the distance along the nanotube and corresponding force constant. However, Walters et al. [186] argued that nanotubes behave as a string rather than a beam (Fig. 40).

Another contentious issue is whether there exists a relationship between nanotube diameter and Young's modulus. Poncharal et al. [160] and Salvetat et al. [187, 188] observed that Young's modulus decreases with increase in tube diameter. In the experiment of Poncharal et al., increasing diameter resulted in a sharp decrease of modulus. This decrease was explained due to a wavelike distortion or ripple on the inner arc of the bent nanotube for relatively thick nanotubes (Fig. 41). However, other measurements did not reveal a direct relation between the Young's modulus and tube diameter.

The existence and migration of buckles during the bending of nanotubes was observed by Falvo et al. [156]. The raised points along the tube were interpreted as buckles (Fig. 42), consistent with the increase in height as shown on the right in Figure 42a. The location of the buckles shifted dramatically, which can be seen from Figure 42b–c. The buckles in (c) appeared in regions which had been featureless, and the buckles of (b) mainly disappeared. Table 8 summarizes measured data on multiwalled carbon nanotubes.

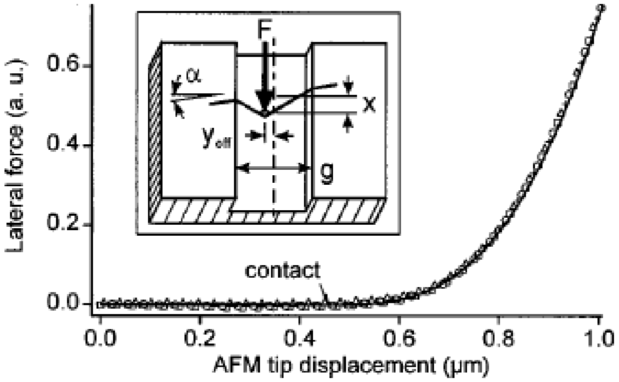

Figure 40. Lateral force on SWCNT rope as a function of AFM tip position. The four symbols represent data from four consecutive lateral force curves on the same rope, showing that this rope is straining elastically with no plastic deformation. Inset: the AFM tip moves along the trench, in the plane of the surface, and displaces the rope as shown. Reprinted with permission from [186], D. A. Walters et al., *Appl. Phys. Lett.* 74, 3803 (1999). © 2003, American Institute of Physics.

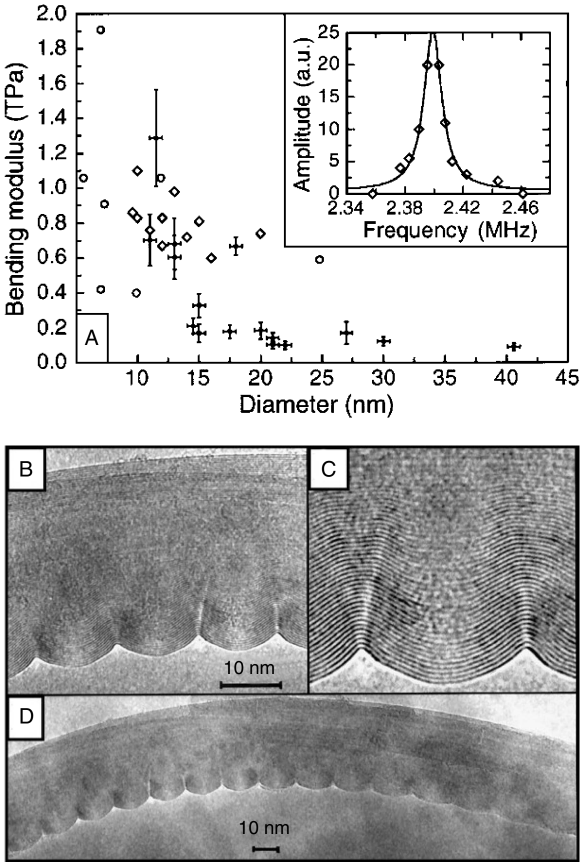

Figure 41. Elastic properties of nanotubes. (A) E_b as a function of diameter: the dramatic drop in E_b for $D \approx 12$ nm is attributed to the onset of a wavelike distortion, which appears to be the energetically favorable bending mode for thicker nanotubes. There is no remarkable change in the Lorentzian line shape of the resonance (inset) for tubes that have large or small moduli, although the low-modulus nanotubes appear to be more damped than the high-modulus tube. (D) TEM image of a bent nanotube showing the characteristic wavelike distortion. (B) and (C) Magnified views of a portion of (D). Reprinted with permission from [160], P. Poncharal et al., *Science* 283, 1513 (1999). © 1999, American Association for the Advancement of Science.

In NEMS applications, it is essential to understand how friction, wear, and lubrication effect the relative motion of objects in contact. The tribology of carbon nanotubes includes two parts: intershell friction and nanotube/substrate friction. Yu et al. [164] pulled the outermost shell and measured the force due to outer shell/inner shell interaction until the outermost shell broke. Cumings et al. [253] opened the end of a MWCNT and exposed the core tubes. The repeated extension and retraction of the core tubes against the outer shell did not reveal any wear or fatigue. The static friction force was estimated to be less than 6.6×10^{-15} N/Å^2 and the dynamic friction force was less than 4.3×10^{-15} N/Å^2.

Falvo et al. [157] studied the frictional behavior of a nanotube on two substrates: mica and graphite. On different substrates, the nanotubes preferred either rolling or sliding, depending on the pulling location. Figure 43 shows the rolling process of a CNT on a graphene substrate and the measured lateral force as a function of tip position.

The effect of mechanical deformation on the electrical properties of CNTs is of particular interest owing to the potential of CNTs in the development of nanoelectromechanical systems. Paulson et al. [254] found that changes

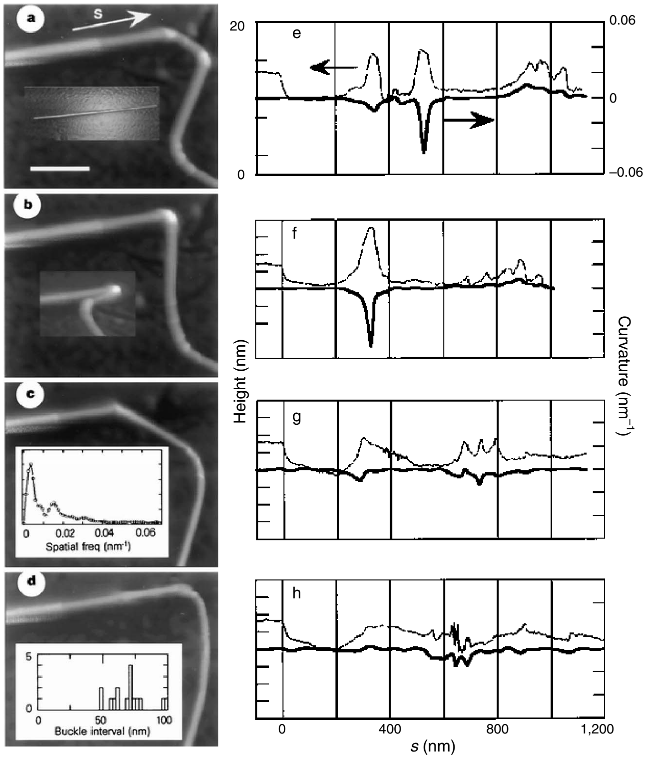

Figure 42. Curvature and height of buckles along a bent carbon nanotube. The white scale bar (in (a) represents 300 nm and all figures are to the same scale. A 20-nm-diameter tube was manipulated from its straight shape [(a), inset)] into several bent configurations (a)–(d). The height and curvature of the bent tubes along its centerline [indicated by the arrow in (a)] are shown in (e)–(h). The upper trace in each graph depicts the height relative to the substrate; the lower trace depicts the curvature data. Height values are relative to substrate height. The "ripple"-like buckles migrate as the tube is manipulated into different configurations. The appearance and disappearance of the ripple buckles, as well as the severe buckle at $s \approx 500$ nm (e)–(f), suggest elastic reversibility. The large buckle at $s \approx 325$ nm (e), (f) retains its raised topographical features even after straightening (g), (h), suggesting that damage has occurred at this point; but the tube does not fracture. The average of the buckle interval histogram [(d), inset)] and the average of the Fourier transforms [(c), inset) for a wide range of bent configurations establish the dominant interval as 68 nm. Reprinted with permission from [156], M. R. Falvo et al., *Nature* 389, 582 (1997). © 1997, American Association for the Advancement of Science.

in nanotube resistance were small unless the nanotubes fractured or the metal–nanotube contacts were perturbed. However, Tombler et al. [206] succeeded in bending individual SWNTs with an AFM tip and measuring conductance as a function of deflection. The study revealed that the conductance of SWCNT changed dramatically under the applied deformation. Figure 44 represents the schematic of their experiment and measured values. Quantum mechanical modeling was employed to verify and explain the experimental findings. The conclusion reached by the authors was that interaction between the AFM tip and the SWCNT deformed the nanotube to a point where the bonding in the nanotube was converted from sp^2 to sp^3. However, in previous studies, the nanotubes were more or less uniformly bent or strained; hence, the chemical bonding evidently remained sp^2.

Table 8. Multiwalled carbon nanotube.

Method	Young's modulus (TPa)	Strength (GPa)	Comments	Ref.
Thermal vibration	1.8	—		[184]
Electrostatic vibration	0.1–1	—	varies with diameter	[160]
Lateral force bending	1.28 ± 0.59	14.2 ± 8.0		[152]
Contact force bending	$0.81 + 0.41$ 0.81–0.16		arc-discharge MWCNT	[188]
Radial indentation	0.0097–0.08	>5.3	compressive modulus and strength	[154]
Tensile test	0.45 ± 0.23	1.72 ± 0.64	very long MWCNT	[189]
Tensile test	0.27–0.95	11–63	outermost layer	[164]
Torsion test	0.6^a			[153]

[a] Shear modulus G.

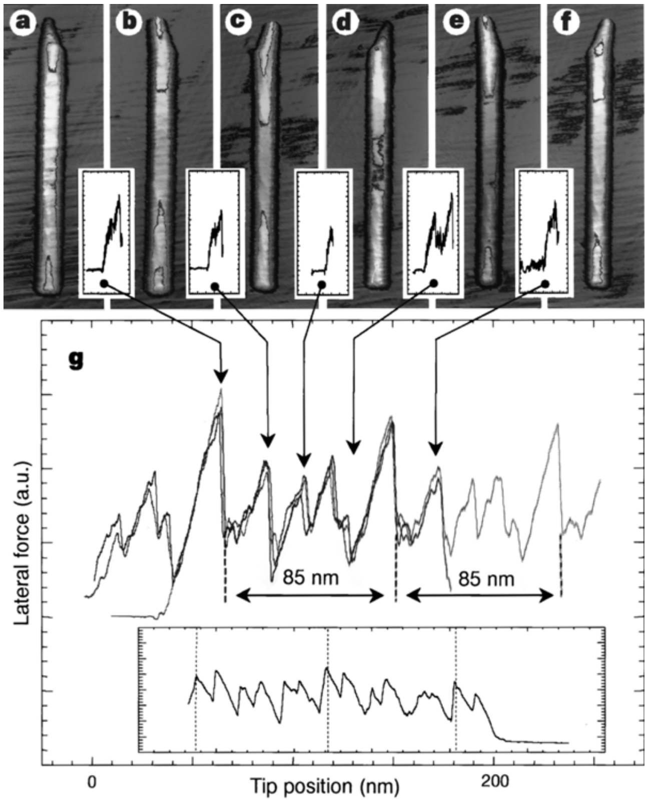

Figure 43. Rolling behavior of CNTs on the graphene substrate (a)–(f) as it is manipulated from left to right. The tube is imaged before and after each of the five manipulations. The insets between each topographical image show the lateral force during each manipulation. The tube is moving from left to right, not gradually but in sudden slips in a stick–slip type rolling motion. In (g), three overlapped signals from separate rolling trials are shown for the lateral force as the tube is pushed through several revolutions of stick–slip rolling motion. The features of the force traces are reproducible. The 85 nm periodicity in the signal, indicated by the dashed lines, is equal to the circumference of the tube at its ends. Reprinted with permission from [157], M. R. Falvo et al., *Nature* 397, 236 (1999). © 1999, Macmillan Publishers Ltd.

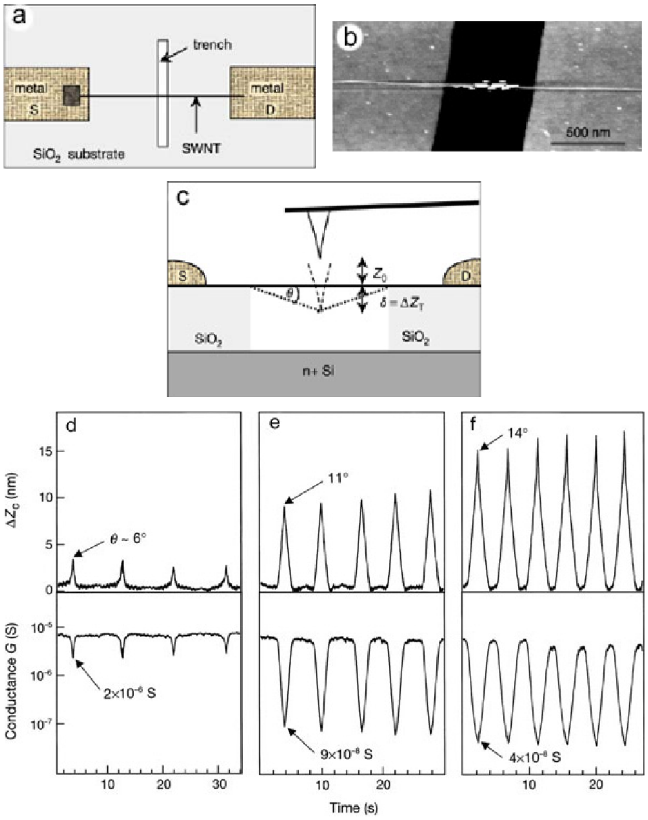

Figure 44. Bending of SWCNT by an AFM tip and the corresponding electrical conductance evolution. (a) Top view of an SWCNT partly suspended over a trench for electromechanical measurements; (b) AFM image of an SWCNT with suspended length $l \approx 605$ nm; (c) Side view of the AFM pushing suspended SWCNT. (d)–(f) cantilever deflection and nanotube electrical conductance evolution during repeated cycles of pushing the suspended SWCNT. θ is the tube bent angle. Initial tip–tube distance is 65 (d), 30 (e), and 8 nm (f), and the speed of the tip motion was about 22 (d), 34 (e), and 44 nm/s (f). It is seen that the conductance of an SWCNT is reduced by two orders of magnitude when deformed by an AFM. Reprinted with permission from [206], T. W. Tombler et al., *Nature* 405, 769 (2000). © 2000, Macmillan Publishers Ltd.

4. THEORETICAL MODELING AND SCALING

During the 1980s and 1990s, a host of experiments on the micrometer and submicrometer scale, including microindentation [15], microtorsion [29, 30], and microbending [28], revealed a strong size effect on the yield strength and hardening of metals. Similar size effects were observed also in metal matrix composites with particle diameters in the micrometer and submicrometer scale [255, 256]. The classical plasticity theories cannot predict these size effects because they involve no material characteristic length. To explain them, several strain gradient theories were developed. The first one was a phenomenological theory by Fleck and Hutchinson [30] based on the existence of a potential. This theory was later extended and improved in several versions [31, 257, 258] while retaining the same basic structure. Another strain gradient theory which received considerable attention was the mechanism-based strain-gradient (MSG) theory [33, 35] derived under certain simplifying assumptions from the concept of geometrically necessary dislocations. Based on numerical experience, this theory was recently improved as the Taylor-base nonlocal (TNT) theory [259], and the improvement consisting in the form of strain gradient dependence of the hardening function made the theory conform to a revision proposed by Bažant [260, 261] on the basis of scaling analysis. Another noteworthy theory was the Acharya and Bassani strain gradient plasticity theory based on the idea of lattice incompatibility [262, 263], which represented a generalization of the incremental theory of plasticity. The asymptotic characters of these strain gradient theories were analyzed recently and it was found that the small-size asymptotic size effect predicted by some of the theories is excessive and unreasonable [259–261].

It might seem that the small-size asymptotic behavior of gradient plasticity is irrelevant because it is approached only at sizes below the range of validity of theory, for which the spacing of the geometrically necessary dislocations (about 10 to 100 nm) and the crystal size are not negligible, and other physical phenomena, such as surface tension, gradation of crystal size, and texture, intervene. However, knowledge of both the small-size and large-size asymptotics is very useful for developing asymptotic matching approximations for the intermediate range, for which the solutions are much harder to obtain. For the purpose of asymptotic matching, the asymptotic behavior must be physically reasonable even if attained outside the range of validity of the theory (this has been demonstrated in the modeling of cohesive fracture when the small-size plastic asymptote is often approached only for specimen sizes much smaller than the inhomogeneity size, e.g., the aggregate size in concrete [260]).

The present chapter reviews and summarizes several recent papers in which it was shown that the main theories proposed in the past, including couple stress theory, stress and rotation gradient theory, MSG, TNT, and the Acharya and Bassani theory, suffer from excessive asymptotic size effect and some exhibit an unrealistic shape of the load-deflection curve. Simple adjustments of all these theories suffice to achieve reasonable asymptotic behavior and thus to make asymptotic matching approximations feasible.

The main strain gradient theories will be briefly introduced and their asymptotic analysis presented by Bažant and Guo [264] will be outlined. After that, a simple asymptotic-matching approximation, suitable for predictions of yield limit and plastic hardening on the micrometer scale, will be presented.

4.1. Strain Gradient Theories

First we will consider the Fleck and Hutchinson phenomenological strain gradient theory [29, 30] and its successive versions. In these theories, the effect of strain gradient tensor is incorporated into the potential energy density function, in a manner similar to the classical theories of Toupin [265] and Mindlin [266] in which only linear elasticity was considered. A higher order stress tensor needs to be introduced in these theories to provide a work conjugate to the strain gradient tensor, and the boundary condition of classical solid mechanics also needs to be modified as well. The classical J_2 deformation theory of plasticity (i.e., Hencky-type solid strain theory) is chosen as the basis of strain gradient generalization.

The Gao and Huang MSG theory [33, 35] does not use the potential energy approach (and actually, potential energy even does not exist in that theory). Rather, this theory is based on the Taylor relation between the shear strength and dislocation density. A multiscale framework is used to introduce the higher order stress tensor and to establish the virtual work balance. Numerical simulations showed that while the higher order stress tensor is affected by the material length characterizing the size of the framework cell (called the mesoscale cell), the stress and strain tensors are almost unaffected. This observation triggered a reformulation in the form of the TNT theory [259], in which the strain gradient is numerically simulated as a nonlocal variable and the higher order stress disappears. This reformulation coincided with a revision proposed by Bažant [260, 261] for entirely different reasons—namely, the observation that the presence of couple stresses, dictated by the use of a strain gradient tensor as an independent kinematic variable, causes an excessive small-size asymptotic size effect, indicating that couple stresses should be removed from the formulation.

The Acharya and Bassani strain gradient theory [262, 263] differs significantly from the previous theories. It represents a generalization of incremental plasticity rather than total strain theory. The effect of a strain gradient is considered by changing the tangential modulus in the constitutive relation, while the framework of classical plasticity theory remains.

4.1.1. Fleck and Hutchinson Theories

The first phenomenological strain-gradient theory developed by Fleck and Hutchinson [29, 30] is called the couple stress theory (denoted by CS). The subsequent modification [31] is called the stretch and rotation gradients theory (denoted by SG). Since the main idea of these two theories is the same, we will consider them jointly. To simplify the problem, only incompressible materials will be considered and the elastic part will be ignored because it is negligible compared to large plastic deformation of metals.

In the classical work of Toupin [265] and Mindlin [266], and dealing only with the linear elasticity case, the strain gradient is introduced into the strain energy density W as

$$\begin{aligned} W = 1/2\lambda\varepsilon_{ii}\varepsilon_{jj} + \mu\varepsilon_{ij}\varepsilon_{ij} + a_1\eta_{ijj}\eta_{ikk} + a_2\eta_{iik}\eta_{kjj} \\ + a_3\eta_{iik}\eta_{jjk} + a_4\eta_{ijk}\eta_{ijk} + a_5\eta_{ijk}\eta_{kij} \end{aligned} \tag{27}$$

where λ and μ are the usual Lamé constants, $\varepsilon_{ij} = (u_{i,j} + u_{j,i})/2$ is the strain, $\eta_{ijk} = u_{k,ij}$ is the component of strain gradient tensor $\boldsymbol{\eta}$, and a_n is the additional elastic stiffness constant of the material. The sum of the first two terms on the right-hand side is the classical strain energy density function, while the other five terms are the contributions of the strain gradient tensor. Based on the strain energy density defined as (27), the Cauchy stress σ_{ij} can be defined as a work conjugate to ε_{ij} (i.e. $\sigma_{ij} = \partial W/\partial\varepsilon_{ij}$). A higher order stress tensor $\boldsymbol{\tau}$, work conjugate to the strain gradient tensor $\boldsymbol{\eta}$, needs to be defined as $\tau_{ijk} = \partial W/\partial\eta_{ijk}$. The strain energy W defined by (22) represents a linear elastic constitutive relation. There are many ways to extend it to a general nonlinear plastic material. Fleck and Hutchinson [31] chose to do it by defining a new variable, a scalar called the combined strain quantity, E, which involves both the strain tensor and the strain gradient tensor, to replace the effective strain in the J_2 theory. W is then assumed, for a general nonlinear plastic material, to be a nonlinear function of E. To define E, the strain gradient tensor $\boldsymbol{\eta}$ needs to be decomposed into a hydrostatic part $\boldsymbol{\eta}^H$ and deviatoric part $\boldsymbol{\eta}'$:

$$\eta^H_{ijk} = (\delta_{ik}\eta_{jpp} + \delta_{jk}\eta_{ipp})/4 \qquad \boldsymbol{\eta}' = \boldsymbol{\eta} - \boldsymbol{\eta}^H \tag{28}$$

Due to incompressibility, we have $\varepsilon'_{ij} = \varepsilon_{ij}$, $\eta'_{ijk} = \eta_{ijk}$. Furthermore, $\boldsymbol{\eta}'$ is decomposed into three orthogonal parts $\boldsymbol{\eta}' = \boldsymbol{\eta}'^{(1)} + \boldsymbol{\eta}'^{(2)} + \boldsymbol{\eta}'^{(3)}$ such that $\eta'^{(m)}_{ijk}\eta'^{(n)}_{ijk} = 0$ when $m \neq n$ [31]; the three invariants $\eta'^{(n)}_{ijk}\eta'^{(n)}_{ijk}$ are used to define E,

$$E = \sqrt{2\varepsilon'_{ij}\varepsilon'_{ij}/3 + \ell_1^2\eta'^{(1)}_{ijk}\eta'^{(1)}_{ijk} + \ell_2^2\eta'^{(2)}_{ijk}\eta'^{(2)}_{ijk} + \ell_3^2\eta'^{(3)}_{ijk}\eta'^{(3)}_{ijk}} \tag{29}$$

where ℓ_i are three length constants which are given different values in different version of the theory.

$$\text{For CS:} \quad \ell_1 = 0 \quad \ell_2 = \ell_{\text{CS}}/2 \quad \ell_3 = \sqrt{5/24}\ell_{\text{CS}} \tag{30}$$

$$\text{For SG:} \quad \ell_1 = \ell_{\text{CS}} \quad \ell_2 = \ell_{\text{CS}}/2 \quad \ell_3 = \sqrt{5/24}\ell_{\text{CS}} \tag{31}$$

Here ℓ_{CS} is called the material characteristic length. If the strain gradient part is ignored, scalar E becomes identical to the effective strain ε used in the classical plasticity theories.

Now the strain energy density W can be expressed as a function of E instead of ε as $W = W(E)$; thus the Cauchy stress tensor $\boldsymbol{\sigma}$ and the higher order stress tensor $\boldsymbol{\tau}$ can be expressed as

$$\sigma_{ij} = \frac{\partial W}{\partial\varepsilon_{ij}} = \frac{dW}{dE}\frac{\partial E}{\partial\varepsilon_{ij}} = \frac{2\varepsilon_{ij}}{3E}\frac{dW}{dE} \tag{32}$$

$$\begin{aligned} \tau_{ijk} &= \frac{\partial W}{\partial\eta_{ijk}} = \frac{dW}{dE}\frac{\partial E}{\partial\eta_{ijk}} \\ &= \frac{dW}{E\,dE}\left(\ell_1^2\eta'^{(1)}_{lmn}\frac{\partial\eta'^{(1)}_{lmn}}{\partial\eta_{ijk}} + \ell_2^2\eta'^{(2)}_{lmn}\frac{\partial\eta'^{(2)}_{lmn}}{\partial\eta_{ijk}} + \ell_3^2\eta'^{(3)}_{lmn}\frac{\partial\eta'^{(3)}_{lmn}}{\partial\eta_{ijk}}\right) \\ &= \frac{\ell_{\text{CS}}^2 C_{ijklmn}\eta_{lmn}dW}{E\,dE} \end{aligned} \tag{33}$$

Here C_{ijklmn} is a six-dimensional constant dimensionless tensor [264]. Since the values of ℓ_i are different in CS and SG theories, the tensor **C** will also be different in these two theories, although for each of them **C** is a constant tensor, that is, independent of ε, $\boldsymbol{\eta}$, and ℓ_{CS}. Because of the existence of higher order stress, the field equations of equilibrium must be generalized as

$$\sigma_{ik,i} - \tau_{ijk,ij} + f_k = 0 \tag{34}$$

where f_k is the body force.

4.1.2. Gao and Huang MSG Theory and TNT Theory

As the first strain gradient theory based on geometrically necessary dislocations, the MSG theory is a generalization of the incremental theory of plasticity [267]. In the MSG theory, the definition of strain gradient tensor $\eta_{ijk} = u_{k,ij}$ is the same as it is in the Fleck and Hutchinson theories, but the definition of higher order stress is different. It is defined by virtual work balance in a multiscale framework. The final constitutive relation reads [33, 260, 261, 264]

$$\sigma_{ik} = K\delta_{ik}\varepsilon_{nn} + \frac{2\sigma}{3\varepsilon}\varepsilon'_{ik} \qquad \tau_{ijk} = l_\varepsilon^2\left(\frac{K}{6}\eta^H_{ijk} + \sigma\Phi_{ijk} + \frac{\sigma_Y^2}{\sigma}\Psi_{ijk}\right) \tag{35}$$

where

$$\Phi_{ijk} = \frac{1}{\varepsilon}(\Lambda_{ijk} - \Pi_{ijk}) \qquad \Psi_{ijk} = f(\varepsilon)f'(\varepsilon)\Pi_{ijk} \tag{36}$$

$$\begin{gathered} \varepsilon = \sqrt{2\varepsilon'_{ij}\varepsilon'_{ij}/3} \qquad \eta = \sqrt{\eta'_{ijk}\eta'_{ijk}/2} \\ \sigma = \sigma_Y\sqrt{f^2(\varepsilon) + l\eta} \end{gathered} \tag{37}$$

and

$$\begin{aligned} \Lambda_{ijk} &= [2\eta_{ijk} + \eta_{kji} + \eta_{kij} - (\delta_{ik}\eta_{ppj} + \delta_{jk}\eta_{ppi})/4]72 \\ \Pi_{ijk} &= [\varepsilon_{ik}\eta_{jmn} + \varepsilon_{jk}\eta_{imn} - (\delta_{ik}\varepsilon_{jp} + \delta_{jk}\varepsilon_{ip})\eta_{pmn}/4] \\ &\quad \times \varepsilon_{mn}/54\varepsilon^2 \\ \eta^H_{ijk} &= (\delta_{ik}\eta_{jpp} + \delta_{jk}\eta_{ipp})/4 \qquad \eta'_{ijk} = \eta_{ijk} - \eta^H_{ijk} \end{aligned} \tag{38}$$

where K is the elastic bulk modulus. Equation (37) defines the new hardening rule of the material in which σ_Y is the yield stress; ε and σ are the effective strain and stress; η is the effective strain gradient, which is proportional to the density of geometrically stored dislocations; $\sigma_Y f(\varepsilon)$ represents the classical plastic hardening function; l is the material intrinsic length (similar to parameter ℓ_{CS} used in the Fleck and Hutchinson theories [29–31]); $\varepsilon'_{ij} = \varepsilon_{ij} - \varepsilon_{nn}/3$ is the deviatoric strain; η^H_{ijk} is the volumetric part of strain gradient tensor; and l_ε is the size of the so-called "mesoscale" cell which is expressed by Gao et al. [33] as

$$l_\varepsilon = \beta(G/\sigma_Y)b \tag{39}$$

Here G is the shear modulus, b is the Burgers vector, and β is an empirical factor whose value is suggested to be between 1 to 10 [33]. The equilibrium equations are the same as (29). It is also interesting to consider a more general hardening relation,

$$\sigma = \sigma_Y[f^q(\varepsilon) + (l\eta)^p]^{1/q} \tag{40}$$

where p and q are positive exponents; and MSG theory corresponds to the case $p = 1$, $q = 2$.

When the MSG theory is used in numerical simulations, the results show that when the value of l_ε is changed, the stress and strain do not change much, although the higher order stress does. This means that the existence of the higher order stress offers no advantage [35] (aside from the fact that they make the asymptotic scaling problematic [261, 264]). Upon noticing this fact, the MSG theory has been replaced by the TNT theory, in which the higher order stress tensor is removed.

In the TNT theory, the strain gradient is not an independent variable but a nonlocal variable defined by numerical integration. The gradient term $\varepsilon_{ij,k}$ can be numerically approximated in a nonlocal form as [259]

$$\varepsilon_{ij,k} = \int_{V_{\text{cell}}} [\varepsilon_{ij}(\mathbf{x} + \xi) - \varepsilon_{ij}(\mathbf{x})]\xi_m \, dV \left(\int_{V_{\text{cell}}} \xi_k\xi_m \, dV\right)^{-1} \tag{41}$$

in which V_{cell} is a sufficiently small representative cell surrounding point described by $\mathbf{x}$. To simplify the integration, V_{cell} can be chosen as a cube centered at $\mathbf{x}$, and then the strain gradient η_{ijk} can be expressed as

$$\begin{gathered} \eta_{ijk} = \frac{1}{I_\varepsilon}\int_{V_{\text{cell}}} [\varepsilon_{ik}\xi_j + \varepsilon_{jk}\xi_i - \varepsilon_{ij}\xi_k] \, dV \quad \text{with} \\ I_\varepsilon = \int_{V_{\text{cell}}} \xi_1^2 \, dV = \frac{1}{12}l_\varepsilon^5 \end{gathered} \tag{42}$$

where l_ε is the size of the cube. Furthermore, one may introduce the volumetric part $\boldsymbol{\eta}^H$ and the deviatoric part $\boldsymbol{\eta}'$ of tensor $\boldsymbol{\eta}$, and the effective strain gradient invariant $\eta = \sqrt{\eta'_{ijk}\eta'_{ijk}}/2$, which is identical to that defined in the MSG theory. Because the strain gradient tensor does not function in (40) as an independent kinematic variable, we need not define the corresponding work-conjugate higher order stress tensor. For $p = 1$, $q = 2$, the constitutive relation is [259]

$$\sigma_{ik} = K\delta_{ik}\varepsilon_{nn} + \frac{2\sigma}{3\varepsilon}\varepsilon'_{ik}$$

where

$$\sigma = \sigma_Y\sqrt{f^2(\varepsilon) + l\eta} \tag{43}$$

Since the new higher order stress is absent, the equilibrium equation of the TNT theory is the same as in the classical theory (i.e., $\sigma_{ij,i} + f_j = 0$).

4.1.3. Acharya and Bassani Theory

The Acharya and Bassani strain gradient theory is a generalization of the classical incremental plasticity theory, in which the strain gradient is assumed to affect only the instantaneous modulus. The strain gradient is considered to be a measure of lattice incompatibility and is introduced only through the second-order tensor as [262, 263]

$$\alpha_{ij} = e_{jkl}\varepsilon^p_{il,k} \tag{44}$$

where e_{jkl} is the alternating symbol and ε^p is the plastic strain. Introducing the invariant:

$$\alpha = \sqrt{2\alpha_{ij}\alpha_{ji}} \tag{45}$$

Acharya and Bassani modified the classical J_2 flow theory as follows [262, 263]:

$$\tau = \sqrt{\sigma'_{ij}\sigma'_{ij}/2} \qquad \dot{\tau} = \dot{\tau}_{cr} = h(\gamma^p, \alpha)\dot{\gamma}^p \tag{46}$$

$$\dot{\varepsilon}^p_{ij} = (\dot{\gamma}^p/2\tau)\sigma'_{ij} \qquad \dot{\sigma}_{ij} = C_{ijkl}(\dot{\varepsilon}_{kl} - \dot{\varepsilon}^p_{kl}) \qquad \gamma^p = \sqrt{2\varepsilon^p_{ij}\varepsilon^p_{ij}/3} \tag{47}$$

Here the instantaneous hardening modulus h depends not only on plastic strain invariant γ^p but also on plastic strain gradient invariant α. An example of this function is [262, 263]

$$h(\gamma^p, \alpha) = h_0\left(1 + \frac{\gamma^p}{\gamma_0}\right)^{N-1}\left[1 + \frac{l^2(\alpha/\gamma_0)^2}{1 + c(\gamma^p/\gamma_0)^2}\right]^{1/2} \tag{48}$$

where l is the material intrinsic length, and h_0, γ_0, c, and N are positive material constants.

There exist other strain gradient theories, but generally they are similar to one of the theories introduced here. For example, the Chen and Wang [268, 269] strain gradient theory is similar to the Fleck and Hutchinson theories.

4.2. Asymptotic Analysis of Strain Gradient Theories

For the purpose of scaling analysis, we need to consider geometrically similar structures of different sizes. This means that the structures are also similarly loaded. It is obvious that the strain gradient theories must reduce to the classical plasticity theory when the structure size is very large. To discuss the asymptotic cases, it is necessary to introduce dimensionless variables. Diverse sets of such variables could be chosen but only one is easy to interpret,

$$\begin{gathered} \bar{x}_i = x_i/D \qquad \bar{u}_i = u_i/D \qquad \bar{\varepsilon}_{ij} = \varepsilon_{ij} \\ \bar{\eta}_{ijk} = \eta_{ijk}D \qquad \bar{f}_k = f_kD/\sigma_N \end{gathered} \tag{49}$$

where D is the characteristic length of the structure, and σ_N is the nominal strength. For geometrically similar structures the strain distribution may often be assumed to be the same, and then $\bar{x}_i$, $\bar{u}_i$, $\bar{\varepsilon}_{ij}$, and $\bar{\eta}_{ijk}$ will be size independent; that is, they will be the same for structures of different sizes. Consequently, the asymptotic behavior of the strain gradient tensor must be $\eta_{ijk} \propto 1/D$.

4.2.1. Asymptotic Analysis of the Fleck and Hutchinson Theories

Scaling and Size Effect The Fleck and Hutchinson strain gradient theory can be used to generalize various particular forms of classical constitutive relations for plasticity. A stress–strain relation in the form of a general power law relation may be chosen as an example, in which the strain energy density is [29–31]

$$W = \frac{n}{n+1}\sigma_0E_0\left(\frac{E}{E_0}\right)^{(n+1)/n} \tag{50}$$

where σ_0, E_0, and n are positive material constants. For hardening materials, $n \geq 1$; typically $n \approx 2$–5 for normal metals. According to (32) and (33), the constitutive relation then reads

$$\sigma_{ik} = \frac{2}{3}\sigma_0\left(\frac{1}{E_0}\right)^{1/n}E^{(1-n)/n}\varepsilon_{ik} \tag{51}$$

$$\tau_{ijk} = \sigma_0\left(\frac{1}{E_0}\right)^{1/n}\ell_{\mathrm{CS}}^2E^{(1-n)/n}C_{ijklmn}\eta_{lmn} \tag{52}$$

It is now useful to define dimensionless variables:

$$\begin{gathered} \bar{\tau}_{ijk} = \tau_{ijk}/(E_0\ell_{\mathrm{CS}}) \qquad \bar{\sigma}_{ij} = \sigma_{ij}/\sigma_0 \qquad \overline{E} = E \\ \bar{\eta}_{ijk}^{(l)} = \eta_{ijk}^{\prime(l)}D \qquad (l = 1, 2, 3) \end{gathered} \tag{53}$$

Then the constitutive relation can be expressed as

$$\bar{\sigma}_{ik} = \frac{2}{3}\left(\frac{1}{E_0}\right)^{1/n}\overline{E}^{(1-n)/n}\bar{\varepsilon}_{ik} \tag{54}$$

$$\bar{\tau}_{ijk} = \left(\frac{1}{E_0}\right)^{1/n}\frac{\ell_{\mathrm{CS}}}{D}\overline{E}^{(1-n)/n}C_{ijklmn}\bar{\eta}_{lmn} \tag{55}$$

The equilibrium equation (29) can be rewritten as

$$\partial_i\bar{\sigma}_{ik} - \frac{\ell_{\mathrm{CS}}}{D}\partial_i\partial_j\bar{\tau}_{ijk} + \frac{\sigma_N}{\sigma_0}\bar{f}_k = 0 \tag{56}$$

where $\partial_i = \partial/\partial\bar{x}_i$ = derivatives with respect to the dimensionless coordinates. Substituting (49) and (55) into (56), one obtains the dimensionless field equation of equilibrium in the form

$$\begin{gathered} \frac{2}{3}\left(\frac{1}{E_0}\right)^{1/n}\partial_i\big(\overline{E}^{(1-n)/n}\bar{\varepsilon}_{ik}\big) - \left(\frac{\ell_{\mathrm{CS}}}{D}\right)^2\left(\frac{1}{E_0}\right)^{1/n} \\ \times\,\partial_i\partial_j\big(C_{ijklmp}\overline{E}^{(1-n)/n}\bar{\eta}_{lmp}\big) = -\frac{\sigma_N}{\sigma_0}\bar{f}_k \end{gathered} \tag{57}$$

Following Bažant [260, 261] and Bažant and Guo [264], we may simplify the analysis by replacing the surface fractions with body forces applied in a very thin boundary layer, the thickness of which tends to zero. This ensures that all the boundary conditions are homogeneous. When the structure is sufficiently large, $\ell_{\mathrm{CS}}/D \to 0$, $\bar{\tau}_{ijl}$ vanish, according to (55), and the equilibrium equations reduce to the classical equilibrium equations, as required. The combined strain quantity, E, reduces to the classical effective strain because the strain gradient part can be ignored compared to the strain part. Then the strain energy density function takes the normal form as a function of the strain only.

As proposed by Bažant and Guo [264], it is interesting to look at the opposite asymptotic character of the theory when the structure size tends to zero, $\ell_{\mathrm{CS}}/D \to \infty$. At first, the dimensionless combined strain quantity can be rewritten as

$$\begin{aligned} \overline{E} &= \sqrt{2\varepsilon'_{ij}\varepsilon'_{ij}/3 + \left(\ell_1^2\bar{\eta}_{ijk}^{\prime(1)}\bar{\eta}_{ijk}^{\prime(1)} + \ell_2^2\bar{\eta}_{ijk}^{\prime(2)}\bar{\eta}_{ijk}^{\prime(2)} + \ell_3^2\bar{\eta}_{ijk}^{\prime(3)}\bar{\eta}_{ijk}^{\prime(3)}\right)/D^2} \\ &\propto D^{-1} \qquad \text{for } \ell_{\mathrm{CS}}/D \to \infty \end{aligned} \tag{58}$$

If one defines a size-independent dimensionless variable

$$\overline{H} = \sqrt{\ell_1^2\bar{\eta}_{ijk}^{\prime(1)}\bar{\eta}_{ijk}^{\prime(1)} + \ell_2^2\bar{\eta}_{ijk}^{\prime(2)}\bar{\eta}_{ijk}^{\prime(2)} + \ell_3^2\bar{\eta}_{ijk}^{\prime(3)}\bar{\eta}_{ijk}^{\prime(3)}}\,/\ell_{\mathrm{CS}} \tag{59}$$

the asymptotic behavior is seen to be

$$\overline{E} \approx \frac{\ell_{\mathrm{CS}}}{D}\overline{H} \qquad \text{for } \ell_{\mathrm{CS}}/D \to \infty \tag{60}$$

Substituting (60) into (57), the asymptotic form of the equilibrium equation reads

$$\frac{2}{3}\left(\frac{\ell_{\mathrm{CS}}}{D}\right)^{(1-n)/n}\left(\frac{1}{E_0}\right)^{1/n}\partial_i\left(\overline{H}^{(1-n)/n}\bar{\varepsilon}_{ik}\right)-\left(\frac{\ell_{\mathrm{CS}}}{D}\right)^{(1+n)/n}$$
$$\times\left(\frac{1}{E_0}\right)^{1/n}\partial_i\partial_j\left(C_{ijklmp}\overline{H}^{(1-n)/n}\bar{\eta}_{lmp}\right)=-\frac{\sigma_N}{\sigma_0}\bar{f}_k \qquad (61)$$

After multiplying this equation by $(D/\ell_{\mathrm{CS}})^{(n+1)/n}$ and taking the limit of the left-hand side for $\ell_{\mathrm{CS}}/D\to\infty$, one gets the following asymptotic form of the equilibrium equations:

$$\partial_i\partial_j\left(C_{ijklmp}\overline{H}^{(1-n)/n}\bar{\eta}_{lmp}\right)=\chi\bar{f}_k$$
$$\text{with } \chi=\overline{E}_0^{1/n}\frac{\sigma_N}{E_0}\left(\frac{D}{\ell_{\mathrm{CS}}}\right)^{(n+1)/n} \qquad (62)$$

Because the left-hand side of the foregoing equation, as well as the dimensionless body force $\bar{f}_k$, is independent of size D and because the boundary conditions are homogeneous and thus size independent, the parameter χ must be size independent. Thus, upon solving σ_N from (62), one finds that the small-size asymptotic scaling law is

$$\sigma_N=\sigma_0\chi\overline{E}_0^{-1/n}\left(\frac{\ell_{\mathrm{CS}}}{D}\right)^{(n+1)/n} \qquad (63)$$

or

$$\sigma_N\propto D^{-(n+1)/n} \qquad (64)$$

For plastic hardening materials, we have $1<(n+1)/n\le 2$. Although the result (64) applies only to the special case of strain energy density function given by (50), the analytical technique used here is general. It is even suitable to the strain energy density function defined directly in terms of strain and strain gradients, rather than as the combined strain quantity. For example, if the strain energy density function is defined as (27) for the case of linear elasticity, a similar analysis can be made and it is found that the size effect law for very small sizes reads [264]

$$\sigma_N\propto D^{-2} \qquad (65)$$

This also shows that (64) is quite general because (65) can be regarded as a special case of (64) in which the strain hardening exponent $n=1$.

Small-Size Asymptotic Load–Deflection Response For some special cases (e.g., the pure torsion of a long thin wire or the bending of a slender beam), the symmetry conditions require displacement distribution to remain similar during the loading process. For such cases, the dimensionless displacement $\bar{u}_k$ can be related to a single parameter, w, and characterized by displacement profile $\hat{u}_k$ as $\bar{u}_k=w\hat{u}_k$ [260, 261, 264]. Since $\hat{u}_k$ is dimensionless, it must be independent of the size D. Displacements $\bar{u}_k$ evolve during the proportional loading process while the distribution profile remains constant. Thus the parameter w can be considered as the displacement norm, $\|\bar{u}_k\|$. It follows that the strain, strain gradient, and combined strain quantity are all proportional to w. Therefore, $\overline{E}$ can be similarly represented as $\overline{E}=w\widehat{E}$, where $\widehat{E}$ is a size independent profile function, and w can be regarded as the deflection magnitude. Substituting this relation into the dimensionless constitutive relation (54) and (55), one can easily get

$$\bar{\sigma}_{ik}=w^{1/n}\hat{\sigma}_{ik} \qquad \bar{\tau}_{ijk}=w^{l/n}\hat{\tau}_{ijk} \qquad (66)$$

where $\hat{\sigma}_{ik}$ and $\hat{\tau}_{ijk}$ are both size independent profile functions. Substituting these relations into dimensionless equilibrium equation (56), one finds that the load-deflection curve must have the form

$$\bar{f}_k\propto w^{1/n} \qquad (67)$$

This relation is similar to the traditional strain–stress relation derived from the strain energy density function (50). The reason the load deflection curve begins with a vertical tangent is that the initial elastic response is assumed to be negligible.

Example One important example is the microtorsion of a thin wire, for which a strong size effect was demonstrated [29–31] and described by strain gradient theories. The strain energy density function W is defined as $W=\sigma E^{N+1}/(N+1)$. Compared with (50), one finds that $N=1/n$. The radius of the wire, D, is chosen as the characteristic size of the structure. The deformation is characterized by the twist angle per unit length, κ. The nominal stress can be defined as $\sigma_N=T/D^3$, where T is the torque. For different radii of the wire, we compare the σ_N values corresponding to the same dimensionless twist $\bar{\kappa}=\kappa D$. The nominal stress can be expressed according to the CS theory as follows:

$$\sigma_N=\frac{T}{D^3}=\frac{6}{N+3}\sigma_0\bar{\kappa}^N\left\{\left[\frac{1}{3}+\left(\frac{\ell_{\mathrm{CS}}}{D}\right)^2\right]^{(N+3)/2}-\left(\frac{\ell_{\mathrm{CS}}}{D}\right)^{N+3}\right\} \qquad (68)$$

When $\ell_{\mathrm{CS}}/D\to\infty$, one has

$$\left[\frac{1}{3}+\left(\frac{\ell_{\mathrm{CS}}}{D}\right)^2\right]^{(N+3)/2}-\left(\frac{\ell_{\mathrm{CS}}}{D}\right)^{N+3}$$
$$\approx\frac{N+3}{2}\left(\frac{D}{3\ell_{\mathrm{CS}}}\right)^2\left(\frac{\ell_{\mathrm{CS}}}{D}\right)^{N+3} \qquad (69)$$

from which

$$\sigma_N\propto D^{-N-1}=D^{-(n+1)/n} \qquad (70)$$

For the load-deflection response, we now obtain the following relation between the load T and the deformation $\bar{\kappa}$:

$$T\propto\kappa^N=\kappa^{1/n} \qquad (71)$$

4.2.2. Asymptotic Analysis of the Gao and Huang MSG Theory and TNT Theory

Scaling and Size Effect The dimensionless variables defined in (49) also need to be used here, and further dimensionless variables need to be defined as follows:

$$\begin{gathered}\bar{\varepsilon} = \varepsilon \qquad \bar{\eta} = \eta D \qquad \bar{\sigma}_{ij} = \sigma_{ij}/\sigma_Y \\ \bar{\tau}_{ijk} = \tau_{ijk}/(\sigma_Y l) \qquad \bar{\sigma} = \sigma/\sigma_Y\end{gathered} \tag{72}$$

$$\begin{gathered}\bar{\eta}^H_{ijk} = \eta^H_{ijk} D \qquad \overline{\Lambda}_{ijk} = \Lambda_{ijk} D \qquad \overline{\Pi}_{ijk} = \Pi_{ijk} D \\ \overline{\Phi}_{ijk} = \Phi_{ijk} D \qquad \overline{\Psi}_{ijk} = \Psi_{ijk} D\end{gathered} \tag{73}$$

These definitions are meaningful because η^H_{ijk}, Λ_{ijk}, and Π_{ijk} are all homogeneous functions of degree 1 of tensors η_{ijk} and ε_{ij}. It is not difficult to obtain a dimensionless version of the constitutive law of the MSG theory

$$\begin{aligned}\bar{\sigma}_{ik} &= \frac{K}{\sigma_Y}\delta_{ik}\bar{\varepsilon}_{nn} + \frac{2\bar{\sigma}}{3\bar{\varepsilon}}\bar{\varepsilon}'_{ik} \\ \bar{\tau}_{ijk} &= \frac{l_\varepsilon^2}{lD}\left(\frac{K}{6\sigma_Y}\bar{\eta}^H_{ijk} + \bar{\sigma}\overline{\Phi}_{ijk} + \frac{1}{\bar{\sigma}}\overline{\Psi}_{ijk}\right)\end{aligned} \tag{74}$$

where l and l_ε are two characteristic material lengths. The corresponding dimensionless equilibrium equation reads

$$\partial_i \bar{\sigma}_{ik} - \frac{l}{D}\partial_i\partial_j\bar{\tau}_{ijk} + \frac{\sigma_N}{\sigma_Y}\bar{f}_k = 0 \tag{75}$$

Same as before, the boundary conditions can again be considered as homogeneous and the applied loads replaced by body forces $\bar{f}_k$ applied within a thin surface layer. The asymptotic behavior for a very large structure is simple. When $l/D \to 0$, we also have $l_\varepsilon/D \to 0$. Thus $\bar{\tau}_{ijk}$ tends to zero, according to Eq. (69), and all the equations reduce to the standard equations of classical plasticity theory, which means that there is no size effect, as required by classical plasticity.

The opposite asymptotic character for sufficiently small structures ($l/D \to \infty$ and $l_\varepsilon/D \to \infty$) is more interesting. The general hardening rule (40) can be rewritten with dimensionless variables as

$$\bar{\sigma} = [f^q(\varepsilon) + (l\bar{\eta}/D)^p]^{1/q} \tag{76}$$

Thus, we have $\bar{\sigma} \approx (l\bar{\eta}/D)^{p/q}$ when $l/D \to \infty$. Substituting (74) into (75), we can express the equilibrium equation as follows:

$$\begin{aligned}&\partial_i\left[\frac{K}{\sigma_Y}\delta_{ik}\bar{\varepsilon}_{nn} + \frac{2}{3\bar{\varepsilon}}\left(\frac{l\bar{\eta}}{D}\right)^{p/q}\bar{\varepsilon}'_{ik}\right] - \left(\frac{l_\varepsilon}{D}\right)^2 \\ &\quad \times \partial_i\partial_j\left[\frac{K}{6\sigma_Y}\bar{\eta}^H_{ijk} + \left(\frac{l\bar{\eta}}{D}\right)^{p/q}\overline{\Phi}_{ijk} + \left(\frac{D}{l\bar{\eta}}\right)^{p/q}\overline{\Psi}_{ijk}\right] \\ &\quad = -\frac{\sigma_N}{\sigma_Y}\bar{f}_k\end{aligned} \tag{77}$$

When $l/D \to \infty$, the five terms on the left-hand side of the foregoing equation are, in sequence, of the order of

$$O(1) \quad O(D^{-p/q}) \quad O(D^{-2}) \quad O(D^{-2-p/q}) \quad O(D^{2+p/q}) \tag{78}$$

When $D \to 0$, the fourth term is generally the dominant one, and so we get the asymptotic form of the equilibrium equation,

$$\partial_i\partial_j(\bar{\eta}^{p/q}\overline{\Phi}_{ijk}) = \chi_1\bar{f}_k \tag{79}$$

with

$$\chi_1 = \left(\frac{l}{l_\varepsilon}\right)^2\frac{\sigma_N}{\sigma_Y}\left(\frac{D}{l}\right)^{2+p/q} \tag{80}$$

Since D is not present in the left-hand side of (80) and the boundary conditions are also homogeneous, the parameter χ must be independent of D. Thus, the general small-size asymptotic scaling law of MSG theory reads [260, 261, 264]

$$\sigma_N = \sigma_Y\chi_1\left(\frac{l_\varepsilon}{l}\right)^2\left(\frac{l}{D}\right)^{2+p/q}$$

and for $\frac{p}{q} = \frac{1}{2}$

$$\sigma_N \propto D^{-5/2} \tag{81}$$

This asymptotic size effect is very strong [260, 261, 264]. It is much stronger than the normal linear elastic fracture mechanics size effect, which is $\sigma_N \propto D^{-1/2}$, or the typical Weibull size effect, which is around $\sigma_N \propto D^{-0.1}$.

There are also some special cases. For example, in the case of microbending, $\overline{\Phi}_{ijk} = 0$ for all i, j, k, which makes the fourth term on the left-hand side of (77) vanish; in the case of incompressible material, $\eta^H_{ijk} = 0$, which makes the third term on the left-hand side of (77) zero. So the general size effect law will change to $\sigma_N \propto D^{-2}$ for microbending of a compressible material, and to $\sigma_N \propto D^{-2+p/q}$ for microbending of an incompressible material (in detail, see [264]).

The size effect $D^{-5/2}$, as well as D^{-2}, is enormous and unrealistic. This is a consequence of the last three terms on the left-hand side of (77), which represent contributions from the couple stresses. A detailed analysis showed that the couple stresses are not necessary to fit the test results and to ensure the virtual work balance [264]. Based on this analysis, Bažant [260, 261] and Bažant and Guo [264] proposed a modified version of the MSG theory in which the couple stresses are made to vanish. This led to a theory identical to the TNT theory [260, 261, 264], which was proposed on the basis of numerical experience with varying the "mesoscale cell size" l_ε. Let us now analyze the asymptotic size effect of this theory. The dimensionless variables defined for the MSG theory may again be used for TNT theory. The dimensionless constitutive relation of the TNT theory reads

$$\bar{\sigma}_{ik} = \frac{K}{\sigma_Y}\delta_{ik}\bar{\varepsilon}_{nn} + \frac{2\bar{\sigma}}{3\bar{\varepsilon}}\bar{\varepsilon}'_{ik} \tag{82}$$

and the differential equation of equilibrium in terms of the dimensionless variables takes the form

$$\partial_i\bar{\sigma}_{ik} + \frac{\sigma_N}{\sigma_Y}\bar{f}_k = 0 \tag{83}$$

For large enough sizes, $D/l \to \infty$, the asymptotic behavior will be identical to the classical theory of plasticity, which implies no size effect. For very small sizes, $D/l \to 0$, we have

$$\bar{\sigma} = [f^q(\varepsilon) + (l\bar{\eta}/D)^p]^{1/q} \approx (l\bar{\eta}/D)^{p/q} \tag{84}$$

and the equilibrium equation can be rewritten as follows:

$$\partial_i\left[\frac{K}{\sigma_Y}\delta_{ik}\bar{\varepsilon}_{nn}+\frac{2}{3\bar{\varepsilon}}\left(\frac{l\bar{\eta}}{D}\right)^{p/q}\bar{\varepsilon}'_{ik}\right]=-\frac{\sigma_N}{\sigma_Y}\bar{f}_k \tag{85}$$

Obviously, the second term on the lefthand side dominates when $D/l \to 0$, and so the asymptotic form of the equilibrium equation is

$$\partial_i\left(\bar{\eta}^{p/q}\frac{\bar{\varepsilon}'_{ijk}}{\bar{\varepsilon}}\right)=\chi\bar{f}_k \qquad \text{with } \chi=-\frac{3}{2}\frac{\sigma_N}{\sigma_Y}\left(\frac{D}{l}\right)^{p/q} \tag{86}$$

Same as before, χ is sizeindependent, and consequently the small-size asymptotic scaling law for the TNT theory is

$$\sigma_N=-\frac{2\sigma_Y}{3}\chi\left(\frac{l}{D}\right)^{p/q}$$

and for $\frac{p}{q}=\frac{1}{2}$

$$\sigma_N \propto D^{-1/2} \tag{87}$$

Four possible cases of small-size asymptotic scaling for the MSG theory and the TNT theory are shown in Figure 45.

Small-Size Asymptotic Load-Deflection Response The characteristic features of the small-size asymptotic load-deflection curves will now be determined. The MSG theory will be analyzed first, and the TNT theory can be treated as a special limiting case of the MSG theory. Again we consider only the special cases where the relative displacement profile does not change during the loading process. Same as before, the displacement can be characterized by parameter w as $\bar{u}_k = w\hat{u}_k$, where $\hat{u}_k$ is the displacement profile, which is not only independent of D but also invariable during the proportional loading process. Similarly, the strain and strain gradient can be expressed as $\bar{\varepsilon}_{ij}=\varepsilon_{ij}=w\hat{\varepsilon}_{ij}$, $\bar{\varepsilon}=\varepsilon=w\hat{\varepsilon}$, $\bar{\eta}_{ijk}=w\hat{\eta}_{ijk}$, $\bar{\eta}=w\hat{\eta}$. Since variables Λ_{ijk} and Π_{ijk} are homogeneous functions of degree 1 of both $\boldsymbol{\eta}$ and $\boldsymbol{\varepsilon}$, their corresponding dimensionless variables can also be expressed as products of w and a dimensionless profile function (i.e., $\overline{\Lambda}_{ijk}=w\widehat{\Lambda}_{ijk}$ and $\overline{\Pi}_{ijk}=w\widehat{\Pi}_{ijk}$). Because of the factor $1/\varepsilon$ in the definition of Φ_{ijk} [see Eq. (36)], we have $\overline{\Phi}_{ijk}=\widehat{\Phi}_{ijk}$, which means that $\overline{\Phi}_{ijk}$ is independent of w. When we consider the beginning of the load-deflection diagram at $D \to 0$, we also have $w \to 0$, which is a limit not discussed during previous sizeeffect analysis. When the effect of w is considered, the five terms on the left-hand side of (77) are proportional, in sequence, to the functions as follows:

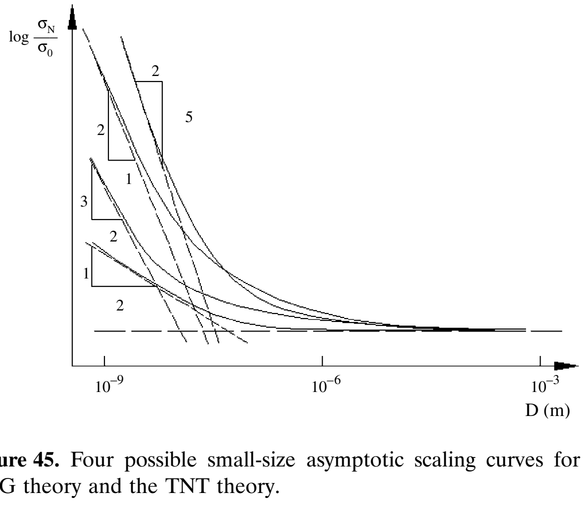

Figure 45. Four possible small-size asymptotic scaling curves for the MSG theory and the TNT theory.

$$\begin{array}{cccc} w & (w/D)^{p/q} & w/D^2 & w^{p/q}/D^{2+p/q} \\ & w^{1-p/q} & w^{1-p/q}/D^{2-p/q} & \end{array} \tag{88}$$

In the case of MSG theory with $p=1$, $q=2$, these functions are

$$w \qquad \sqrt{w/D} \qquad w/D^2 \qquad w^{1/2}/D^{5/2} \qquad w^{1/2}/D^{3/2} \tag{89}$$

and (77) can then be expressed as

$$-\frac{\sigma_N}{\sigma_Y}\bar{f}_k=a_1w+a_2w^{p/q}D^{-p/q}+a_3wD^{-2}+a_4w^{p/q}D^{-2-p/q}$$
$$+a_5w^{1-p/q}D^{-2+p/q} \tag{90}$$

where parameters a_i are constants independent of D and w. Since the force $\bar{f}_k$ should decrease when w decreases, one knows that $1-p/q>0$, which implies $p<q$. As we discussed before, if only $D \to 0$ is considered (or, in other words, $D \ll w$), the dominant term is $a_4w^{p/q}D^{-2-p/q}$, which means that

$$\bar{f}_k \propto w^{p/q} \qquad (\text{for } w \gg D) \tag{91}$$

For the MSG theory, this gives

$$\bar{f}_k \propto w^{1/2} \qquad (\text{for } w \gg D) \tag{92}$$

We need to consider another asymptotic case in which $w \ll D$ (e.g., at the beginning of the load-deflection diagram). The dominant term in this case is either $a_4w^{p/q}D^{-2-p/q}$ or $a_5w^{1-p/q}D^{-2+p/q}$, depending on the value of p/q. The asymptotic load-deflection behavior is

$$\bar{f}_k \propto w^r \qquad r=\min\{p/q,1-p/q\} \qquad (\text{for } w \ll D) \tag{93}$$

For MSG theory, the dominant term is $a_4w^{1/2}D^{-5/2}$, and so the load $\bar{f}_k$ initially increases in proportion to $w^{1/2}$. Thus one has the asymptotic load-deflection relation for MSG theory as

$$\bar{f}_k \propto w^{1/2} \qquad \text{for all } w \tag{94}$$

As discussed in the preceding section, some terms in (77) may vanish in some special cases, and a similar analysis can be applied to these special cases. For example, for microbending of an incompressible material, the third and fourth terms in (77) vanish, and as a result (92) changes as follows:

$$-\frac{\sigma_N}{\sigma_Y}\bar{f}_k=a_1w+a_2\sqrt{w/D}+a_5w^{1/2}/D^{3/2} \tag{95}$$

The asymptotic load-deflection curve is simple because the last term on the right-hand side of (95) dominates when

D is small, regardless of the ratio of w/D, and so the asymptotic load-deflection relation for this special case is again

$$\bar{f}_k \propto w^{1/2} \qquad \text{for all } w \tag{96}$$

This means the vanishing of some terms in flexure problems will not change the asymptotic load-deflection behavior. The TNT theory can be treated as a special case of the MSG theory. If the last three terms on the right-hand of the MSG equilibrium equation (77) vanish, the equation becomes identical to equilibrium equation (85) of the TNT theory. So (85) can be expressed as

$$-\frac{\sigma_N}{\sigma_Y}\bar{f}_k = a_1 w + a_2\sqrt{w/D} \tag{97}$$

For small enough D and w, the dominant term will be the second term on the right-hand side of (97), and so we have

$$\bar{f}_k \propto w^{1/2} \qquad \text{for all } w \qquad \text{(TNT theory)} \tag{98}$$

It should be noted that the elastic part of the response has been neglected, which is why the load-deflection curves in (94), (96), and (98) begin with a vertical tangent.

Example The experiment of microtorsion of a thin wire can also be analyzed by the MSG theory [35] or TNT theory. Equation (35) in [35] can be transformed to the dimensionless formula

$$\sigma_N = \frac{T}{D^3} = \sigma_Y \frac{2\pi\bar{\kappa}}{3}\int_0^1 \left\{ \frac{\bar{\sigma}}{\bar{\varepsilon}}\left(\rho^2 + \frac{l_\varepsilon^2}{12D^2}\right) + \frac{l_\varepsilon^2 f(\bar{\varepsilon})f'(\bar{\varepsilon})}{12D^2\bar{\sigma}} \right\}\rho\, d\rho \tag{99}$$

where σ_N is the nominal stress, T is the torque, D is the radius of wire (which is also chosen as the characteristic length of the structure), σ_Y is the yield stress of macroscale metal, and $\bar{\kappa} = \bar{\eta} = \kappa D$ is the dimensionless specific angle of twist, where κ = actual specific angle of twist (i.e., the rotation angle per unit length of wire). Substituting $\bar{\sigma} = \sqrt{f^2(\bar{\varepsilon}) + l\bar{\eta}/D} \approx \sqrt{l\bar{\kappa}/D}$ into this formula, we find that, for $D \to 0$, the dominant part is obtained by integration of the second term, which leads to the following small-size asymptotic form:

$$\sigma_N = \sigma_Y\left(\frac{\pi}{18} l_\varepsilon^2 l^{1/2}\int_0^1 \frac{\rho}{\bar{\varepsilon}} d\rho\right)\bar{\kappa}^{1/2} D^{-5/2} \tag{100}$$

This result verifies the conclusions (81) and (89), where $\bar{\kappa}$ is considered as a measure of deflection, analogous to w in (89). The asymptotic load-deflection behavior of the TNT theory can be obtained similarly.

Another special case is the application of the MSG theory to the microbending of incompressible metals [35]. Equation (29) in [35] can be transformed to the dimensionless version

$$\sigma_N = \frac{M}{D^2} = 2\sigma_Y\int_0^{1/2}\left[\frac{2}{\sqrt{3}}\bar{\sigma}\rho + \frac{\bar{\kappa} l_\varepsilon^2 f(\bar{\varepsilon})f'(\bar{\varepsilon})}{9D^2\bar{\sigma}}\right]d\rho \tag{101}$$

where D is the beam depth (the characteristic dimension of the structure), M is the bending moment, $\bar{\kappa} = \bar{\eta} = \kappa D$ is the dimensionless bending curvature, and κ is the actual bending curvature. When $D \to 0$, the small-size asymptotic form is

$$\sigma_N = \sigma_Y\left(\frac{2}{9} l_\varepsilon^2 l^{-1/2}\int_0^{1/2} f(\bar{\varepsilon})f'(\bar{\varepsilon})d\rho\right)\bar{\kappa}^{1/2} D^{-3/2} \tag{102}$$

This verifies for this special case the asymptotic behavior $\sigma_N \propto D^{-2+p/q}$, as well as (96). Letting $l_\varepsilon = 0$, one finds that this asymptotic character also applies to the TNT theory.

4.2.3. Asymptotic Analysis of Acharya and Bassani's Theory

Let us now give a simple analysis of the asymptotic behavior of the Acharya and Bassani strain gradient theory [263]. We define dimensionless variables $\bar{u}_i = u_i/D$, $\bar{\varepsilon}_{ij,k} = \varepsilon_{ij,k}D$, and that $\bar{\alpha}_{ij} = \alpha_{ij}D$. When $D \to 0$, the asymptotic behavior of the plastic hardening modulus ($\bar{\gamma}^p = \gamma^p$) defined by (48) is found to be

$$\begin{aligned} h(\gamma^p, \alpha) &= h_0\left(1 + \frac{\gamma^p}{\gamma_0}\right)^{N-1}\left[1 + c(\gamma^p/\gamma_0)^2\right]^{-1/2}\frac{\bar{\alpha}}{\gamma_0}\frac{l}{D} \\ &\propto D^{-1} \end{aligned} \tag{103}$$

This shows that, at the same strain level, the plastic hardening modulus (slope of load deflection curve) increases as D^{-1} when $D \to 0$. If the elastic part is neglected for very large plastic strain, the nominal stress must also scale asymptotically as D^{-1}. This asymptotic size effect is again quite strong (but not as strong as in the MSG theory). This size effect can be reduced by modifying the hardening function $h(\gamma^p, \alpha)$. For example, if the hardening modulus is redefined as

$$h(\gamma^p, \alpha) = h_0\left(1 + \frac{\gamma^p}{\gamma_0}\right)^{N-1}\left[1 + \frac{l\alpha/\gamma_0}{1 + c(\gamma^p/\gamma_0)}\right]^{1/2} \tag{104}$$

then the asymptotic scaling becomes more reasonable:

$$h(\gamma^p, \alpha) \propto D^{-1/2} \quad \text{when } D \to 0 \tag{105}$$

4.3. Asymptotic-Matching Approximation Formula

After determining the asymptotic behaviors of strain gradient plasticity theories, one can obtain an asymptotic matching approximation for a smooth transition of the nominal strength in the intermediate size range. In [260, 261, 264], a smooth transition between the case of no size effect for $D \to \infty$ and the case of power law size effect $\sigma_N \propto D^{-s}$ for $D \to 0$ ($s > 0$) has been described by the simple asymptotic-matching approximation

$$\sigma_N = \sigma_0\left[1 + \left(\frac{D_0}{D}\right)^{2s/r}\right]^{r/2} \tag{106}$$

where r is a constant to be determined by data fitting, while parameters σ_0 and D_0 can be determined by either the asymptotic size effect formula or data fitting. This formula was shown to fit the results for microtorsion and microbending (Figs. 46 and 47).

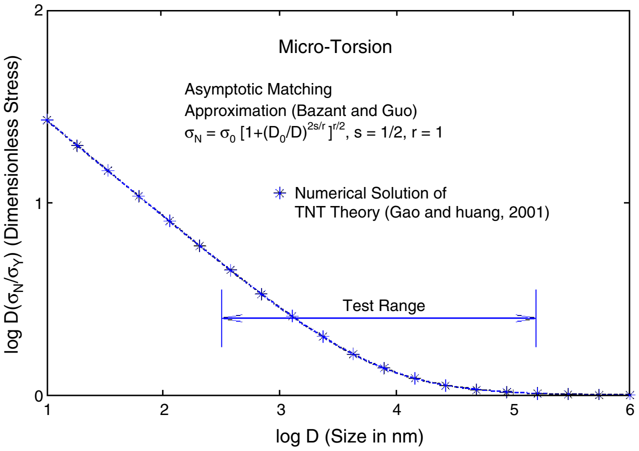

Figure 46. Asymptotic-matching approximation for microtorsion.

4.4. Concluding Remarks on Strain Gradient Theories

In many applications of interest (e.g., microelectronics and MEMS), characteristic dimensions are in excess of 100 nm–1 μm. Modeling the mechanics of such systems at the atomistic level is beyond present computational capabilities. Therefore, extension of continuum theories to account for size scales is of high relevance. Here we have discussed many of the existing theories. At the same time, their range of applicability was examined through small-size asymptotics.

Even though the small-size asymptotic behavior is obtained only below the size range of applicability of the theory (>100 nm), it is useful to pay attention to it. Several main theories show unreasonable small-size asymptotic behavior, which impairs the representation of experimentally observed behavior in the practical size range and spoils asymptotic matching approximations. Simple adjustments of the theories suffer to obtain reasonable asymptotics and make asymptotic matching approximation meaningful.

Finally, an analogy with quasibrittle materials such as concrete, rocks, sea ice, and fiber composite may be mentioned [270]. For them, too, the small size as well as large size asymptotic behaviors are attained only outside the range of validity of the theoretical models (cohesive crack model, crack band model, nonlocal damage models), that is, for specimen sizes much smaller than the inhomogeneity size or much larger than the largest constructable structures. Yet the knowledge of two-sided asymptotics has been shown to be very helpful to achieving good asymptotic matching approximations for the intermediate practical range.

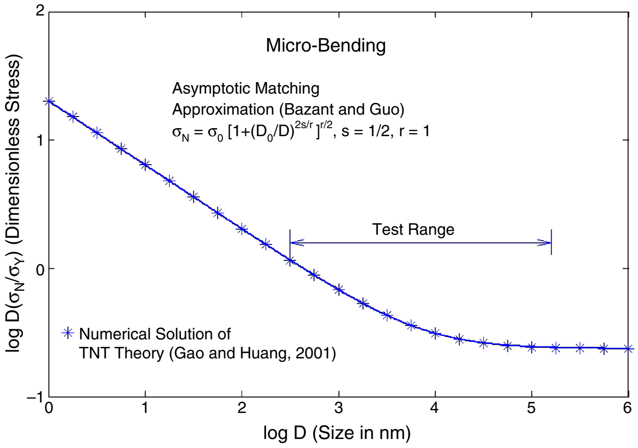

Figure 47. Asymptotic-matching approximation for microbending.

It is also important to emphasize that strain gradient theories cannot explain the size scale effects observed in fcc metals in the absence of strain gradients [36, 37]. Clearly, new continuum theories are needed to be able to predict these size effects.

5. MODELING ONE-DIMENSIONAL MATERIALS: NANOTUBES AND NANOWIRES

One-dimensional nanoscale materials, that is, nanotubes (carbon CNT, boron nitride BNNT, etc.) and nanowires (e.g., silicon SiNW), are drawing ever more attention due to their promising properties for a variety of future applications. Mechanical strength of CNTs and BNNTs along with their electrical (for carbon) and thermal conductivity (for both), are appealing for composite applications. Although SiNWs have little advantage in strength, their chemical properties enable ease of doping and as a result they are outstanding light-emitters due to a quantum confinement effect. These nanowires have the additional advantage that can be straightforwardly integrated in Si circuits. Here, we review some of the recent results concerning the mechanical yield and failure as well as the possible coalescence or welding mechanisms of C and BN nanotubes. Fundamental structures and energetics of SiNWs are also discussed, in order to contrast bulk-based materials with the uniquely built cylindrical entities.

Interest in composite application of CNTs is due to their mechanical strength combined with the electrical and thermal conductivity that together could lead to development a multifunctional material basis for a variety of novel purposes ranging from textile to aerospace applications. Besides the economical aspects, like low cost volume production of CNT, the limiting factors for their utilization in composites include their proper dispersion in matrix media, matrix-CNT adhesion and load transfer, intertubular connectivity and shear resistance, and internal strength of individual tubes. While manufacturing and cost issues remain mostly a subject of experimental empirical study, the mechanics of nanotubes has been a topic of detailed theoretical investigations and multiscale computational modeling.

Theoretical studies of CNT mechanics have been motivated by experimental evidence of great resilience and by expectations of extraordinary strength. These are based upon the strength of the individual carbon bonds and the elegance of two-dimensional carbon network structures. CNT mechanics, including buckling, yielding, and failure mechanisms, have been extensively investigated and are summarized in recent reviews [145, 271], while the studies of elastic behavior, both linear and nonlinear, and buckling have made the transition from science to engineering (via the demonstrated correspondence of atomistic modeling methods and continuum elasticity and finite elements [145, 271]). Many issues of inelastic behavior still require analysis at the atomic scale utilizing the solid state physics and quantum chemistry formulations.

As an important example, we have recently undertaken a systematic series of quantum *ab initio* calculations of structures and moduli [272, 273] for C, BN (boron nitride or "white graphite," shown in Fig. 48) and CF_x (fluorinated carbon) shells. They utilize density functional based computations (within Gaussian package) with periodic boundary conditions that yielded a set of accurate elastic parameters [272] that can be further employed in engineering shell models for CNT elasticity, vibrations, or postbuckling deformations. This careful discussion is also timely since somewhat controversial data have recently emerged in the literature, caused mainly by different interpretations of the effective cross-section of nanostructures, referred to recently as *Yakobson's paradox* [274].

SiNW is another type of 1D structure of high interest due mostly to the strategy of building nanoscale technology via the developed infrastructure of the silicon microelectronics industry. Recent efforts have demonstrated that ultrathin SiNWs indeed have properties that make them very competitive in many aspects of nanoscale electronics. First, Si is fairly reactive, enabling it to be easily doped. Second, faster and lower energy-consuming electronic devices have been suggested that are constructed of arrays of SiNWs, preliminary forms of which have already been built [275]. Finally, the quantum confinement effect opens a direct bandgap as wide as 2.0–3.0 eV, laying a potential foundation for effective visible light emitters and the so-called *all-photonic* technology possible using silicon materials alone [276]. Additionally, this direct bandgap has the potential to enable photovoltaics of ultrahigh efficiency, that is, if bulk quantities of SiNWs could be produced reasonably cheaply.

Recently, we found the ground-state structure of ultrathin, pristine SiNWs by utilizing theoretical analysis and large-scale computations [277]. Surprisingly, these SiNWs are polycrystalline and favor a whisker growth mode (i.e., they grow much faster along their axis than circumferentially). Their structures and energetics with be shown in comparison to other single crystalline nanowires. Moreover, faceting and matching of the facets at the wire's edges were found to play a critical role in stabilizing the SiNWs.

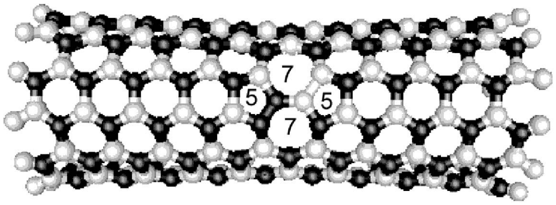

Figure 48. Stone–Wales 5/7/7/5 defect in (5, 5) BN nanotube. Reprinted with permission from [273], H. F. Bettinger et al., *Phys. Rev. B* 65, 041406 (2002). © 2002, American Physical Society.

5.1. Strength, Failure, and Healing Mechanisms in Nanotubes

5.1.1. Energies and Thermodynamics of the Yield Defects

The transition from yield to tensile strength for CNTs and its underlying atomic mechanism have been subjects of particular interest. It has been proposed that two alternative yield-failure paths in CNT are generally possible [44, 278]: (i) a brittle fracture through a nucleation and growth of a crack as in Figure 49, or (ii) a dislocation relaxation (i.e. *intramolecular plasticity*) in case of a miniscule fiber-nanotube. Indeed, it has been observed in detailed computer simulations that the primary yield defect, an event at the atomic scale, is represented by individual bond rotation, which leads to the formation of two pentagon–heptagon pairs in the hexagonal lattice, 5/7/7/5 in Figure 48. In the chemistry of fullerenes and nanotubes, this corresponds to "pyracylene" or Stone–Wales transformation. A computational study of this defect energy at different levels of applied tension allows one to determine the strain ε at which the defect formation becomes thermodynamically favorable, whereby the nanotube can then possibly yield to the external tensile load.

Classical empirical potentials, tight binding approximations (TBA), and *ab initio* density functional theory calculations all identify the range of thermodynamic instability with respect to yield as ε exceeds 6–7%. More recently we applied the same approach to isomorphic BN nanotubes, where the Stone–Wales defect (Fig. 48) again has been shown to have the lowest energy, below that of the competing structure of 4/8/8/4 polygons. The determined defect formation energy under strain approximately follows a linear relationship, namely,

$$E_{\mathrm{SW}} = 5.5\text{–}46\varepsilon \text{ eV} \tag{107}$$

(cf. $E_{\mathrm{SW}} = 3.1\text{–}45\varepsilon$ eV in case of armchair carbon). Thus, density functional analysis of yield thermodynamics for carbon (C, purely covalent) and boron nitride (BN, covalent-ionic) permits a comparison of their yield strength with the conclusion that partially ionic BN can be more resistant to yield than the homoelemental C.

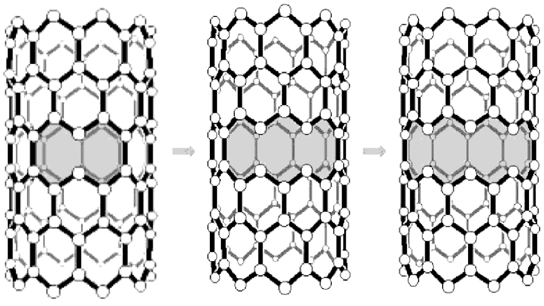

Figure 49. Quantum-mechanical relaxation of a nanocrack in H-terminated CNT. Reprinted with permission from [280], T. Dumitrica et al., *J. Chem. Phys.* 119, 1281 (2003). © 2003, American Institute of Physics.

5.1.2. Kinetic Theory of Strength

In any practical situation, a system is expected to sustain tension only within a finite time limit, while thermodynamic equilibrium implies time-unlimited conditions. A more consistent approach to failure [279, 280] comes from one based on rate equations and leads to more realistic estimates of strength. A kinetic theory approach to strength evaluation is an important step in this regard where the key point is to determine the probability, P, of defect formation (yield) as a function of time. It therefore can be calculated, provided that the computed activation barriers E^* are available, by

$$P = 10^{15} L d \Delta t \,\text{sec}^{-1}\,\text{nm}^{-2} \exp[-E^*(\varepsilon, \chi)/k_b T] \sim 1 \qquad (108)$$

where L is the CNT length and d is its diameter. Following extensive computational examination of the saddle-point activation barriers E^* (Fig. 50a), this equation enabled calculation of the breaking strains ε for a variety of temperatures T, duration times Δt, and chiral symmetries χ of SWNT, as shown in Figure 50b. With more accurate *ab initio* calculations of the transition state barriers E^*, the process can be enhanced.

Kinetic analysis shows that although thermodynamic requirements for yield can be relatively low (strains of 6–7%), overcoming activation barriers the strain level must exceed 15–20% (depending on chiral symmetry of the tube and the test duration). At this high strain level, nanotubes can in principle undergo brittle failure through "direct" bond breaking via a series of metastable radical states that include dangling bonds or unpaired electrons. We have recently [281] performed quantum mechanical structure relaxations which determined the energies of several of the first metastable defect states corresponding to one, two, or three broken bonds in the lattice. As an example, Figure 49 shows a singular broken-bond structure that emerges as metastable at approximately 16% tensile strain. From a chemistry viewpoint, such structures represent a biradical, $R^{\cdot} + {}^{\cdot}R$, that would immediately recombine under normal conditions. Unlike the Stone–Wales defect, these *virtual* defects do not exist in free lattice structures but can only emerge beyond the bifurcation point at high tension.

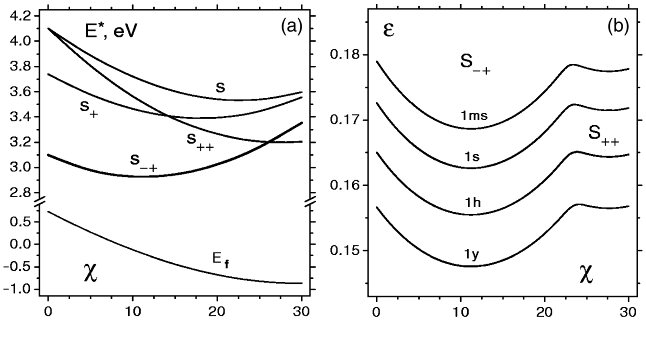

Figure 50. Activation barriers at $\varepsilon = 5\%$ (a), and breaking strain values (b) of CNT. Reprinted with permission from [280], G. G. Samsonidze and B. I. Yakobson, *Phys. Rev. Lett.* 88 (2002). © 2002, American Physical Society.

5.1.3. Welding and Reversible Failure

The possibility of nanotube coalescence, which is either a lateral or a butt-welding process of merging separate entities into one, has been investigated in detail due to its importance in formation of CNT networks, and therefore on overall electrical conductance, thermal transport, and mechanical strength [282]. We have discovered a mechanism of welding that consists exclusively of Stone–Wales bond rotations. It therefore appears as a feasible physical process at elevated temperatures or under irradiation. An example is shown in Figure 51 that illustrates the intermediate steps (as numbered) of (10,10)-CNT pair butt-welding, at high temperature or under irradiation (e-beam or laser):

$$(10,10) + (10,10) \rightarrow (10,10) \quad \text{or}$$
$$(15,0) + (15,0) \rightarrow (15,0) \qquad (109)$$

Emerging intermediate structures must possess unique and possibly useful electronic properties as they represent quantum dots with already attached nanotube-wires. Detailed calculations of the intermediate energies, E, shown in Figure 52 allow us to compare the energy barriers. The main data are obtained with TBA; open squares correspond to density functional results, and open circles are obtained from high-temperature molecular dynamics simulations. The data also show a possible reduction of the barriers by application of external mechanical forces, F, compression or tension, in transition from energy to enthalpy criteria, $H = E + FL$. This is important for engineering new nanostructures through stretching [283] or welding [281], as well as for improvement of bulk materials due to increased connectivity of the tubules in CNT bundles or possibly in composites.

5.2. Silicon Nanowires: Structure and Energetics

Although SiNWs possess much weaker bonds, they have higher rigidity (originating from the higher coordination [284, 285]) making the tiny wires extremely fragile compared to carbon nanotubes. Any practical construction of Si nanowires should not be too small in order to allow them to be sustainable in natural ambient conditions. Obviously, extremely thin ($d < 1$ nm) 1D Si structures could not emulate bulk structuring because all the atoms are actually located on a surface. Therefore, reconstruction will conform them into clusters or a chain of clusters even at zero temperature. The modeling of cluster chains considered as a SiNW currently accounts for a big portion of theoretical studies [286, 287]. Recently, a chain of fullerene-like clustered Si_{20}

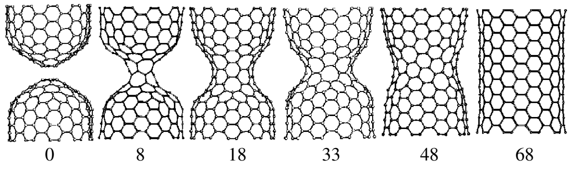

Figure 51. Steps of (10,10) + (10,10) coalescence via Stone–Wales bond rotations.

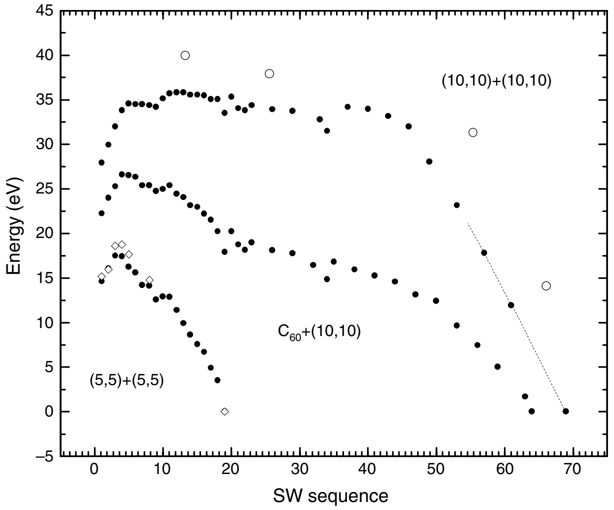

Figure 52. Computed energies of intermediate structures in coalescence. Reprinted with permission from [282], Y. F. Zhao et al., *Phys. Rev. Lett.* 88 (2002). © 2002, American Physical Society.

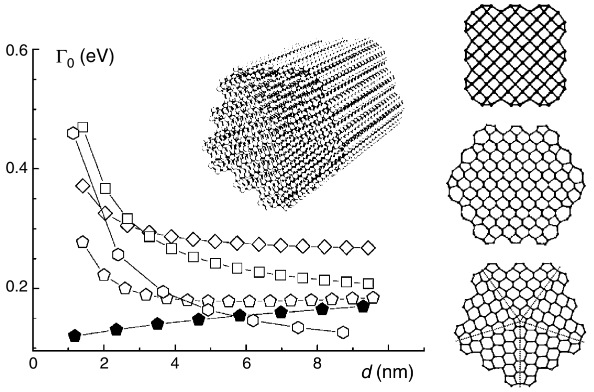

Figure 53. Energy and structure (only cross-section on the right three) of three types of SiNWs. On the energy curve, diamonds and squares denote two surface reconstructions of the square SiNW; solid and open pentagons denote two types of pentagonal SiNWs. The five radial lines in the pentagonal model (right bottom) are {111} interfaces of stacking faults. Reprinted with permission from [277], Y. F. Zhao and B. I. Yakobson, *Phys. Rev. Lett.* 91, 035501 (2003).

was found to have a reasonably low energy [288]. If one adds more atomic layers to the cluster, chains will systematically accumulate strain, become distorted, and rapidly increase the energy of the system. Above a particular thickness ($d \sim 1.5$ nm for pristine SiNW), crystalline whiskers are more favorable and the process of faceting is the decisive factor to conserve energy.

Conventionally, the equilibrium shape of a faceted crystal is determined by minimization of Wulff's free energy, which neglects the interaction of facets (edge effect) and assumes a fixed bulk. This is a good approximation for relatively large crystals but poorly applicable to ultrathin SiNWs with $d <$ 10 nm.

In [289] we generalized Wulff's free energy as

$$F = s\gamma_s + E_e + E_b \tag{110}$$

to include the energy of matching the adjacent facets, E_e, and certain changes in the bulk, E_b, including possible internal granularity or elastic strain toward lowering the overall energy. Because the shape of a crystalline SiNWs is scalable with its diameter, the energy of an isomorphic family (with the same shape but various thickness) can be evaluated without full-scale computation. Several families of pristine whiskers with four-, five-, and six-fold symmetry in cross-section have been investigated and the relative energy is shown in Figure 53.

Surprisingly, a polycrystalline family has the lowest overall energy at $d < 6$ nm due to the perfect matching of the facets along the edges with very little cost to the bulk energy. This type of SiNW also has an important growth kinetics property: the dimer rows along the axis make the adatoms diffuse much faster in the axis direction than along the circumference.

Because the structures of the SiNW will influence their properties [290], the creation of new structures with controlled thickness and crystallographic orientation [291] is very important in practical applications. The new crystallographic structure with cross-sectional fivefold symmetry potentially provides opportunity for novel properties. It is known that the unique growth kinetics make it possible to produce SiNWs with identical crystallographic orientation (i.e., [110] direction).

In recent experiments, bundles of pristine SiNWs with diameters of 3–7 nm and lengths of >100 nm were formed in high vacuum [288] (see Fig. 54), which might be of the pentagonal type according to its growth kinetics. The hexagonal single crystalline SiNW with hydrogen-terminated facets has also been recently identified in [292].

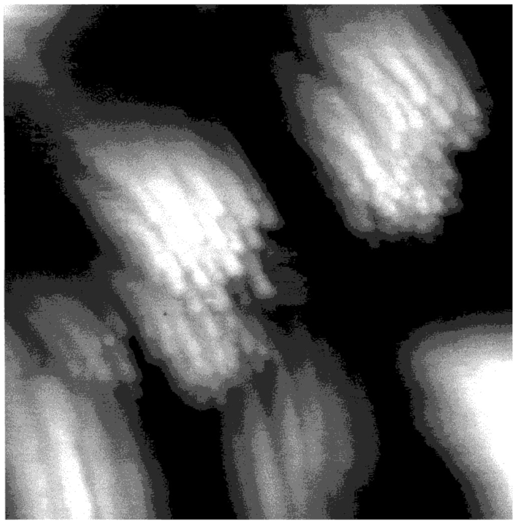

Figure 54. Bundles of the pristine SiNW, produced in high vaccum. Reprinted with permission from [288], B. Marsen and K. Sattler, *Phys. Rev. B* 60, 11593. (1999). © 1999, American Physical Society.

GLOSSARY

ACKNOWLEDGMENTS

H.D.E acknowledges support from the Nanoscale Science and Engineering Initiative of the National Science Foundation (NSF) under NSF award EEC-0118025, NSF through award CMS-0120866, and the Federal Aviation Administration (FAA) award DTFA03-01-C-00031.

REFERENCES

1. C. V. Thompson, *Annu. Rev. Mater. Sci.* 30, 159 (2000).
2. C. A. Neugebauer, J. B. Newkirk, and D. A. Vermilyea, "Structure and Properties of Thin Films." Wiley, New York, 1959.
3. E. Arzt, *Acta Mater.* 46, 5611 (1998).
4. J. W. Hutchinson, *Int. J. Solids Struct.* 37, 225 (2000).
5. A. Needleman and E. Van der Giessen, *Mater. Sci. Eng. A* 309, 1 (2001).
6. D. Weygand, L. H. Friedman, E. van der Giessen, and A. Needleman, *Mater. Sci. Eng. A* 309, 420 (2001).
7. J. Y. Shu, N. A. Fleck, E. Van der Giessen, and A. Needleman, *J. Mech. Phys. Solids* 49, 1361 (2001).
8. J. Weertman and J. R. Weertman, "Elementary Dislocation Theory." Oxford Univ. Press, Oxford, 1992.
9. D. Hull and D. J. Bacon, "Introduction to Dislocations." Pergamon, Oxford, 1984.
10. P. Lejcek and V. Sima, *Mater. Sci. Eng.* 60, 121 (1983).
11. M. M. Borodkina and T. S. Orekhova, *Fiz. Metallov Metalloved.* 54, 1204 (1982).
12. P. A. Beck, J. C. Kremer, L. J. Demer, and M. L. Holzworth, *Trans. Am. Inst. Mining Metall. Eng.* 175, 372 (1948).
13. W. W. Mullins, *Acta Metall.* 6, 414 (1958).
14. C. V. Thompson, *J. Mater. Res.* 8, 237 (1993).
15. W. D. Nix, *Metall. Trans. A* 20, 2217 (1989).
16. P. Chaudhari, *Philos. Mag. A* 39, 507 (1979).
17. M. S. De Guzman, G. Neubauer, P. Flinn, and W. D. Nix, *Mater. Res. Soc. Symp. Proc.* 308 (1993).
18. Q. Ma and D. R. Clarke, *J. Mater. Res.* 10, 853 (1995).
19. N. A. Stelmashenko, M. G. Walls, L. M. Brown, and Y. V. Milman, *Acta Metall. Mater.* 41, 2855 (1993).
20. M. Atkinson, *J. Mater. Res.* 10, 2908 (1995).
21. W. J. Poole, M. F. Ashby, and N. A. Fleck, *Scr. Mater.* 34, 559 (1996).
22. W. D. Nix, *Mater. Sci. Eng. A* 234, 37 (1997).
23. W. D. Nix and H. J. Gao, *J. Mech. Phys. Solids* 46, 411 (1998).
24. K. W. McElhaney, J. J. Vlassak, and W. D. Nix, *J. Mater. Res.* 13, 1300 (1998).
25. M. Goken and M. Kempf, *Acta Mater.* 47, 1043 (1999).
26. S. Suresh, T. G. Nieh, and B. W. Choi, *Scr. Mater.* 41, 951 (1999).
27. M. R. Begley and J. W. Hutchinson, *J. Mech. Phys. Solids* 46, 2049 (1998).
28. J. S. Stolken and A. G. Evans, *Acta Mater.* 46, 5109 (1998).
29. N. A. Fleck, G. M. Muller, M. F. Ashby, and J. W. Hutchinson, *Acta Metall. Mater.* 42, 475 (1994).
30. N. A. Fleck and J. W. Hutchinson, *J. Mech. Phys. Solids* 41, 1825 (1993).
31. N. A. Fleck and J. W. Hutchinson, in "Advances in Applied Mechanics" (J. W. Hutchinson and T. Y. Wu, Eds.), Vol. 33, p. 295. San Diego, Academic, 1997.
32. E. C. Aifantis, *Int. J. Eng. Sci.* 30, 1279 (1992).
33. H. Gao, Y. Huang, W. D. Nix, and J. W. Hutchinson, *J. Mech. Phys. Solids* 47, 1239 (1999).
34. H. Gao, Y. Huang, and W. D. Nix, *Naturwissenschaften* 86, 507 (1999).
35. Y. Huang, H. Gao, W. D. Nix, and J. W. Hutchinson, *J. Mech. Phys. Solids* 48, 99 (2000).
36. H. D. Espinosa, B. C. Prorok, and B. Peng, *J. Mech. Phys. Solids*, in press.
37. H. D. Espinosa, B. C. Prorok, and M. Fischer, *J. Mech. Phys. Solids* 51, 47 (2003).
38. H. D. Espinosa and B. C. Prorok, *Mater. Res. Soc. Symp. Proc.* 688 (2001).
39. B. C. Prorok and H. D. Espinosa, *J. Nanosci. Nanotechnol.* 2, 427 (2002).
40. S. Iijima, *Nature* 354, 56 (1991).
41. M. S. Dresselhaus, G. Dresselhaus, and R. Saito, *Carbon* 33, 883 (1995).
42. V. Ivanov, A. Fonseca, J. B. Nagy, A. Lucas, P. Lambin, D. Bernaerts, and X. B. Zhang, *Carbon* 33, 1727 (1995).
43. D. Qian, G. J. Wagner, W. K. Liu, M. F. Yu, and R. S. Ruoff, *Appl. Mech. Rev.* 55, 495 (2002).
44. B. I. Yakobson, *Appl. Phys. Lett.* 72, 918 (1998).
45. F. R. Brotzen, *Int. Mater. Rev.* 39, 24 (1994).
46. O. Kraft and C. A. Volkert, *Adv. Eng. Mater.* 3, 99 (2001).
47. R. P. Vinci and J. J. Vlassak, *Annu. Rev. Mater. Sci.* 26, 431 (1996).
48. Nano Indenter XP, MTS Systems Corp., http://www.mts.com/.
49. Triboscope, Hysitron Inc., http://www.hysitron.com/.
50. UMIS-2000, CSIRO, http://www.csiro.au/.
51. Nano Hardness Tester, CSM Instruments, http://www.csm-instruments.com/.
52. Fischerscope, Helmut Fischer Gmbh, http://www.fischer-technology. com/home.html.
53. M. F. Doerner and W. D. Nix, *J. Mater. Res.* 1, 601 (1986).
54. W. C. Oliver and G. M. Pharr, *J. Mater. Res.* 7, 1564 (1992).
55. R. Saha, Z. Xue, Y. Huang, and W. D. Nix, *J. Mech. Phys. Solids* 49, 1997 (2001).
56. R. Saha and W. D. Nix, *Acta Mater.* 50, 23 (2002).
57. R. Saha and W. D. Nix, *Mater. Sci. Eng. A* 319–321, 898 (2001).
58. H. Buckle, "The Science of Hardness Testing and Its Research Applications." ASM, Metals Park, OH, 1973.
59. H. Yuan and J. Chen, *Int. J. Solids Struct.* 38, 8171 (2001).
60. A. B. Mann, R. C. Cammarata, and M. A. Nastasi, *J. Mater. Res.* 14, 2195 (1999).
61. A. E. Giannakopoulos and S. Suresh, *Scr. Mater.* 40, 1191 (1999).
62. T. Y. Tsui and G. M. Pharr, *J. Mater. Res.* 14, 292 (1999).
63. Y. Y. Lim, M. M. Chaudhri, and Y. Enomoto, *J. Mater. Res.* 14, 2314 (1999).
64. D. L. Joslin and W. C. Oliver, *J. Mater. Res.* 5, 123 (1990).
65. R. B. King, *Int. J. Solids Struct.* 23, 1657 (1987).
66. C. B. Ponton and R. D. Rawlings, *Mater. Sci. Technol.* 5, 865 (1989).
67. C. B. Ponton and R. D. Rawlings, *Mater. Sci. Technol.* 5, 961 (1989).
68. J.-L. Loubet, B. N. Lucas, and W. C. Oliver, *Mater. Res. Soc. Symp. Proc.* 436, 233 (1996).
69. M. J. Mayo and W. D. Nix, *Acta Metall.* 36, 2183 (1988).
70. A. Bolshakov, W. C. Oliver, and G. M. Pharr, *Mater. Res. Soc. Symp. Proc.* 436, 141 (1996).
71. A. Bolshakov and G. M. Pharr, *J. Mater. Res.* 13, 1049 (1998).
72. J. C. Hay, A. Bolshakov, and G. M. Pharr, *J. Mater. Res.* 14, 2296 (1999).
73. M. Dao, N. Chollacoop, K. J. Van Vliet, T. A. Venkatesh, and S. Suresh, *Acta Mater.* 49, 3899 (2001).
74. A. C. Fischer, "Nanoindentation." Springer, New York, 2002.
75. S. P. Baker, R. F. Cook, S. G. Corcoran, and N. R. Moody, "Fundamentals of Nanoindentation and Nanotribology II." Material Research Society, 2001.
76. N. R. Moody, W. W. Gerberich, and S. P. Baker, *Mater. Res. Soc. Symp. Proc.* 522 (1998).

77. T. P. Weihs, S. Hong, J. C. Bravman, and W. D. Nix, *J. Mater. Res.* 3, 931 (1988).
78. J. A. Schweitz, *MRS Bull.* 17, 34 (1992).
79. S. P. Baker and W. D. Nix, *J. Mater. Res.* 9, 3131 (1994).
80. M. Knauss, Thesis, University of Stuttgart, 1996.
81. O. Kraft, R. Schwaiger, and W. D. Nix, *Mater. Res. Soc. Symp. Proc.* 518, 39 (1998).
82. R. Schwaiger and O. Kraft, *Scr. Mater.* 41, 823 (1999).
83. J. Florando, H. Fujimoto, Q. Ma, O. Kraft, R. Schwaiger, and W. D. Nix, *Mater. Res. Soc. Symp. Proc.* 563, 231 (1999).
84. B. C. Prorok, H. D. Espinosa, B. Peng, K.-H. Kim, N. Moldovan, O. Auciello, J. A. Carlisle, D. M. Gruen, and D. C. Mancini, *Exp. Mech.*, in press.
85. H. D. Espinosa, B. Peng, K.-H. Kim, B. C. Prorok, N. Moldovan, X. C. Xiao, J. E. Gerbi, J. Birrell, O. Auciello, J. A. Carlisle, D. M. Gruen, and D. C. Mancini, *Mater. Res. Soc. Symp. Proc.* 741 (2002).
86. Y. A. Burenkov and S. P. Nikanorov, *Soviet Phys.-Solid State* 16, 963 (1974).
87. G. G. Stoney, *Proc. Roy. Soc. London* 82, 172 (1909).
88. F. J. von Preissig, *J. Appl. Phys.* 66, 4262 (1989).
89. J. T. Pan and I. Blech, *J. Appl. Phys.* 55, 2874 (1984).
90. P. A. Flinn, *Mater. Res. Soc. Symp. Proc.* 130, 41 (1989).
91. D. S. Gardner and P. A. Flinn, *IEEE Trans. Electron Devices* 35, 2160 (1987).
92. D. S. Gardner and P. A. Flinn, *Mater. Res. Soc. Symp. Proc.* 130, 69 (1989).
93. P. H. Townsend and T. A. Brunner, *J. Appl. Phys.* 62, 4438 (1987).
94. J. D. Romero, M. Khan, H. Fatemi, and J. Turlo, *J. Mater. Res.* 6, 1996 (1991).
95. V. T. Gillard and W. D. Nix, *Z. Metall.* 84, 874 (1993).
96. E. M. Zellinski, R. P. Vinci, and J. C. Bravman, *Mater. Res. Soc. Symp. Proc.* 391, 103 (1995).
97. O. Kraft and W. D. Nix, *Mater. Res. Soc. Symp. Proc.* 516, 201 (1998).
98. R. M. Keller, S. P. Baker, and E. Arzt, *J. Mater. Res.* 13, 1307 (1998).
99. T. S. Park and S. Suresh, *Acta Mater.* 48, 3169 (2000).
100. J. W. Beams, "Structure and Properties of Thin Films." Wiley, New York, 1959.
101. R. L. Edwards, G. Coles, and W. N. Sharpe, Jr., *Exp. Mech.*, in press.
102. E. I. Bromley, J. N. Randall, D. C. Flanders, and R. W. Mountain, *J. Vac. Sci. Technol. B* 1, 1364 (1983).
103. M. G. Allen, M. Mehregany, R. T. Howe, and S. D. Senturia, *Appl. Phys. Lett.* 51, 241 (1987).
104. O. Tabata, S. Sugiyama, and M. Takigawa, *Appl. Phys. Lett.* 56, 1314 (1990).
105. J. J. Vlassak and W. D. Nix, *J. Mater. Res.* 7, 3242 (1992).
106. V. M. Paviot, J. J. Vlassak, and W. D. Nix, *Mater. Res. Soc. Symp. Proc.* 356, 579 (1994).
107. V. Ziebart, O. Paul, U. Munch, J. Schwizer, and H. Baltes, *J. Microelectromech. Syst.* 7, 320 (1998).
108. D. T. Read, *Int. J. Fatigue* 20, 203 (1998).
109. D. T. Read and J. W. Dally, *J. Mater. Res.* 8, 1542 (1993).
110. J. A. Ruud, D. Josell, F. Spaepen, and A. L. Greer, *J. Mater. Res.* 8, 112 (1993).
111. D. Josell, D. van Heerden, D. Read, J. Bonevich, and D. Shechtman, *J. Mater. Res.* 13, 2902 (1998).
112. I. Chasiotis and W. G. Knauss, *Proc. SPIE* 3512, 66 (1998).
113. I. Chasiotis and W. G. Knauss, *Proc. SPIE* 4175, 96 (2000).
114. W. N. Sharpe, B. Yuan, and R. L. Edwards, *J. Microelectromech. Syst.* 6, 193 (1997).
115. W. N. Sharpe, Jr., S. Brown, G. C. Johnson, and W. C. Knauss, *Mater. Res. Soc. Symp. Proc.* 518, 57 (1998).
116. D. A. LaVan and W. N. Sharpe, *Exp. Mech.* 39, 210 (1999).
117. W. N. Sharpe, K. T. Turner, and R. L. Edwards, *Exp. Mech.* 39, 162 (1999).
118. K. M. Jackson, R. L. Edwards, G. F. Dirras, and W. N. J. Sharpe, *Mater. Res. Soc. Symp. Proc.* 687 (2001).
119. H. D. Espinosa, B. C. Prorok, and M. Fischer, in "Proc. SEM Ann. Conf. on Exp. and Appl. Mech.," Portland, OR, 2001, p. 446.
120. S. Greek and S. Johansson, *Proc. SPIE* 3224, 344 (1997).
121. T. Yi and C. J. Kim, in "Proc. MEMS (MEMS-Vol. 1), ASME Int. Mechanical Engineering Congress and Exposition," Nashville, TN, 1999, pp. 81–86.
122. T. Tsuchiya, O. Tabata, J. Sakata, and Y. Taga, *J. Microelectromech. Syst.* 7, 106 (1998).
123. G. Cornella, R. P. Vinci, R. S. Iyer, and R. H. Dauskardt, *Mater. Res. Soc. Symp. Proc.* 518, 81 (1998).
124. J. Amano, T. Ando, M. Shikida, K. Sato, and T. Tsuchiya, *Mater. Res. Soc. Symp. Proc.* 687 (2002).
125. T. Tsuchiya, J. Sakata, M. Shikida, and K. Sato, *Mater. Res. Soc. Symp. Proc.* 687 (2002).
126. S. Greek, F. Ericson, S. Johansson, M. Furtsch, and A. Rump, *J. Micromech. Microeng.* 9, 245 (1999).
127. H. D. Espinosa, B. Peng, B. C. Prorok, N. Moldovan, O. Auciello, J. A. Carlisle, D. M. Gruen, and D. C. Mancini, submitted for publication.
128. M. T. A. Saif, S. Zhang, M. A. Haque, and K. J. Hsia, *Acta Mater.* 50, 2779 (2002).
129. M. A. Haque and M. T. A. Saif, *Scr. Mater.* 47, 863 (2002).
130. M. A. Haque and M. T. A. Saif, *Sens. Actuator A* 97-8, 239 (2002).
131. M. A. Haque and M. T. A. Saif, *Exp. Mech.* 42, 123 (2002).
132. M. A. Haque and M. T. A. Saif, in "Proc. of the SEM Ann. Conf. on Exp. and Appl. Mech.," Milwaukee, WI, 2002.
133. J. A. Connally and S. B. Brown, *Science* 256, 1537 (1992).
134. S. B. Brown, W. Van Arsdell, and C. L. Muhlstein, in "Transducers 97, International Conference on Solid-State Sensors and Actuators," 1997, p. 591.
135. W. W. Van Arsdell and S. B. Brown, *J. Microelectromech. Syst.* 8, 319 (1999).
136. C. L. Muhlstein, S. B. Brown, and R. O. Ritchie, *Mater. Res. Soc. Symp. Proc.* 657 (2000).
137. C. L. Muhlstein, S. E. A. Stach, and R. O. Ritchie, *Mater. Res. Soc. Symp. Proc.* 687 (2002).
138. C. L. Muhlstein, S. B. Brown, and R. O. Ritchie, *J. Microelectromech. Syst.* 10, 593 (2001).
139. C. L. Muhlstein, S. B. Brown, and R. O. Ritchie, *Sens. Actuator A* 94, 177 (2001).
140. H. Kahn, R. Ballarini, and A. H. Heuer, *Mater. Res. Soc. Symp. Proc.* 657, 543 (2001).
141. H. Kahn, R. Ballarini, R. L. Mullen, and A. H. Heuer, *Proc. Roy. Soc. London Ser. A* 455, 3807 (1999).
142. E. E. Fischer and P. E. Labossiere, in "Proc. of the SEM Ann. Conf. on Exp. and Appl. Mech.," Milwaukee, WI, 2002.
143. L. Que, J. S. Park, and Y. B. Gianchandani, *J. Microelectromech. Syst.* 10, 247 (2001).
144. B. I. Yakobson, C. J. Brabec, and J. Bernholc, *Phys. Rev. Lett.* 76, 2511 (1996).
145. B. I. Yakobson and R. E. Smalley, *Am. Scientist* 85, 324 (1997).
146. X. Zhou, J. J. Zhou, and Z. C. Ou-Yang, *Phys. Rev. B* 62, 13692 (2000).
147. J. P. Lu, *Phys. Rev. Lett.* 79, 1297 (1997).
148. C. Journet, W. K. Maser, P. Bernier, A. Loiseau, M. L. delaChapelle, S. Lefrant, P. Deniard, R. Lee, and J. E. Fischer, *Nature* 388, 756 (1997).
149. T. W. Ebbesen and P. M. Ajayan, *Nature* 358, 220 (1992).
150. A. Thess, R. Lee, P. Nikolaev, H. J. Dai, P. Petit, J. Robert, C. H. Xu, Y. H. Lee, S. G. Kim, A. G. Rinzler, D. T. Colbert, G. E. Scuseria, D. Tomanek, J. E. Fischer, and R. E. Smalley, *Science* 273, 483 (1996).
151. W. Z. Li, S. S. Xie, L. X. Qian, B. H. Chang, B. S. Zou, W. Y. Zhou, R. A. Zhao, and G. Wang, *Science* 274, 1701 (1996).

152. E. W. Wong, P. E. Sheehan, and C. M. Lieber, *Science* 277, 1971 (1997).
153. P. A. Williams, S. J. Papadakis, A. M. Patel, M. R. Falvo, S. Washburn, and R. Superfine, *Appl. Phys. Lett.* 82, 805 (2003).
154. W. D. Shen, B. Jiang, B. S. Han, and S. S. Xie, *Phys. Rev. Lett.* 84, 3634 (2000).
155. R. M. I. Taylor and S. R., in "Advanced Interfaces to Scanning Probe Microscopes" (H. S. Nalwa, Ed.), Vol. 2. Academic Press, New York, 1999.
156. M. R. Falvo, G. J. Clary, R. M. Taylor, V. Chi, F. P. Brooks, S. Washburn, and R. Superfine, *Nature* 389, 582 (1997).
157. M. R. Falvo, R. M. Taylor, A. Helser, V. Chi, F. P. Brooks, S. Washburn, and R. Superfine, *Nature* 397, 236 (1999).
158. M. F. Yu, M. J. Dyer, G. D. Skidmore, H. W. Rohrs, X. K. Lu, K. D. Ausman, J. R. von Ehr, and R. S. Ruoff, *Nanotechnology* 10, 244 (1999).
159. Klocke Nanotechnik Co., http://www.nanomotor.de.
160. P. Poncharal, Z. L. Wang, D. Ugarte, and W. A. de Heer, *Science* 283, 1513 (1999).
161. E. A. Stach, T. Freeman, A. M. Minor, D. K. Owen, J. Cumings, M. A. Wall, T. Chraska, R. Hull, J. W. Morris, A. Zettl, and U. Dahmen, *Microsc. Microanal.* 7, 507 (2001).
162. Z. Lin, Ph.D. Thesis, Northwestern University, 2000.
163. Nanofactory Instruments, http://www.nanofactory.com/.
164. M. F. Yu, O. Lourie, M. J. Dyer, K. Moloni, T. F. Kelly, and R. S. Ruoff, *Science* 287, 637 (2000).
165. X. Q. Chen, T. Saito, H. Yamada, and K. Matsushige, *Appl. Phys. Lett.* 78, 3714 (2001).
166. A. Bezryadin, C. Dekker, and G. Schmid, *Appl. Phys. Lett.* 71, 1273 (1997).
167. P. A. Smith, C. D. Nordquist, T. N. Jackson, T. S. Mayer, B. R. Martin, J. Mbindyo, and T. E. Mallouk, *Appl. Phys. Lett.* 77, 1399 (2000).
168. M. P. Hughes, in "Handbook of Nanoscience, Engineering and Technology" (B. D. S. Lyshevski, G. Iafrate, and W. A. Goddard III, Eds.). Boca Raton, CRC Press, 2002.
169. M. P. Hughes and H. Morgan, *J. Phys. D* 31, 2205 (1998).
170. A. Ramos, H. Morgan, N. G. Green, and A. Castellanos, *J. Phys. D* 31, 2338 (1998).
171. Y. Huang, X. F. Duan, Q. Q. Wei, and C. M. Lieber, *Science* 291, 630 (2001).
172. M. Fujiwara, E. Oki, M. Hamada, Y. Tanimoto, I. Mukouda, and Y. Shimomura, *J. Phys. Chem. A* 105, 4383 (2001).
173. S. M. Huang, L. M. Dai, and A. W. H. Mau, *J. Phys. Chem. B* 103, 4223 (1999).
174. H. J. Dai, *Acc. Chem. Res.* 35, 1035 (2002).
175. J. Cumings and A. Zettl, *Science* 289, 602 (2000).
176. B. Bhushan, "Handbook of Micro/Nano Tribology." CRC Press, Boca Raton, 1999.
177. S. Morita, R. Wiesendanger, and E. Meyer, "Nanocontact Atomic Force Microscopy." Springer-Verlag, Berlin, 2002.
178. V. J. Morris, A. P. Gunning, and A. R. Kirby, "Atomic Force Microscopy for Biologists." Imperial College Press, London, 1999.
179. R. Wiesendanger, "Scanning Probe Microscopy and Spectroscopy: Methods and Applications." Cambridge Univ. Press, Cambridge, UK, 1995.
180. D. Bonnell, "Scanning Probe Microscopy and Spectroscopy: Theory, Techniques, and Applications." Wiley, New York, 2000.
181. M. F. Yu, T. Kowalewski, and R. S. Ruoff, *Phys. Rev. Lett.* 85, 1456 (2000).
182. J. W. G. Wildoer, L. C. Venema, A. G. Rinzler, R. E. Smalley, and C. Dekker, *Nature* 391, 59 (1998).
183. T. W. Odom, J. L. Huang, P. Kim, and C. M. Lieber, *Nature* 391, 62 (1998).
184. M. M. J. Treacy, T. W. Ebbesen, and J. M. Gibson, *Nature* 381, 678 (1996).
185. A. Krishnan, E. Dujardin, T. W. Ebbesen, P. N. Yianilos, and M. M. J. Treacy, *Phys. Rev. B* 58, 14013 (1998).
186. D. A. Walters, L. M. Ericson, M. J. Casavant, J. Liu, D. T. Colbert, K. A. Smith, and R. E. Smalley, *Appl. Phys. Lett.* 74, 3803 (1999).
187. J. P. Salvetat, G. A. D. Briggs, J. M. Bonard, R. R. Bacsa, A. J. Kulik, T. Stockli, N. A. Burnham, and L. Forro, *Phys. Rev. Lett.* 82, 944 (1999).
188. J. P. Salvetat, A. J. Kulik, J. M. Bonard, G. A. D. Briggs, T. Stockli, K. Metenier, S. Bonnamy, F. Beguin, N. A. Burnham, and L. Forro, *Adv. Mater.* 11, 161 (1999).
189. Z. W. Pan, S. S. Xie, L. Lu, B. H. Chang, L. F. Sun, W. Y. Zhou, G. Wang, and D. L. Zhang, *Appl. Phys. Lett.* 74, 3152 (1999).
190. J. R. Weertman and P. G. Sanders, *Solid State Phenom.* 35–36, 249 (1993).
191. T. Volpp, E. Goring, W. M. Kuschke, and E. Arzt, *Nanostruct. Mater.* 8, 855 (1997).
192. R. Z. Valiev, "Mechanical Properties and Deformation Behavior of Materials Having Ultra-Fine Microstructures." Kluwer Academic, Dordecht, 1993.
193. J. E. Carsley, W. W. Milligan, X. H. Zhu, and E. C. Aifantis, *Scr. Mater.* 36, 727 (1997).
194. J. E. Carsley, A. Fisher, W. W. Milligan, and E. C. Aifantis, *Metall. Mater. Trans. A* 29, 2261 (1998).
195. W. W. Milligan, S. A. Kachney, M. Ke, and E. C. Aifantis, *Nanostruct. Mater.* 2, 267 (1993).
196. H. D. Espinosa, Y. Zhu, and B. Peng, in "Proc of the SEM Ann. Conf. on Exp. and Appl. Mech.," Milwaukee, WI, 2002.
197. Y. Zhu, F. Barthelat, P. E. Labossiere, N. Moldovan, and H. D. Espinosa, in "Proc. of the SEM Ann. Conf. Exp. and Appl. Mech.," Charlotte, NC, 2003.
198. MicroSensors, Inc., http://www.microsensors.com.
199. C. D. Lott, T. W. McLain, J. N. Harb, and L. L. Howell, *Sens. Actuator A* 101, 239 (2002).
200. A. M. Minor, E. T. Lilleodden, E. A. Stach, and J. W. Morris, *J. Electron. Mater.* 31, 958 (2002).
201. A. M. Minor, J. W. Morris, and E. A. Stach, *Appl. Phys. Lett.* 79, 1625 (2001).
202. J. C. Spence, "Experimental High-Resolution Electron Microscopy," 2nd ed. Oxford Univ. Press, Oxford, 1988.
203. D. B. Williams and B. C. Carter, "Transmission Electron Microscopy, A Textbook for Materials Science." Plenum, New York, 1996.
204. P. Buseck, J. M. Cowley, and L. Eyring, "High Resolution Transmission Electron Microscopy—Theory and Applications." Oxford Univ. Press, Oxford, 1990.
205. M. Gao, J. M. Zuo, R. D. Twesten, I. Petrov, L. A. Nagahara, and R. Zhang, *Appl. Phys. Lett.* 82, 2703 (2003).
206. T. W. Tombler, C. W. Zhou, L. Alexseyev, J. Kong, H. J. Dai, L. Lei, C. S. Jayanthi, M. J. Tang, and S. Y. Wu, *Nature* 405, 769 (2000).
207. W. N. Sharpe, Jr., in "The MEMS Handbook" (M. Gad-el-Hak, Ed.). CRC Press, Boca Raton, 2002.
208. T. P. Weihs, S. Hong, J. C. Bravman, and W. D. Nix, *Mater. Res. Soc. Symp. Proc.* 402, 87 (1989).
209. D. Read, Y. Cheng, R. Keller, and J. McColskey, *Scr. Mater.* 45, 583 (2001).
210. B. T. Comella and M. R. Scanlon, *J. Mater. Sci.* 35, 567 (2000).
211. M. Hommel and O. Kraft, *Acta Mater.* 49, 3835 (2001).
212. T. E. Buchheit, T. R. Schmale, and D. A. LaVan, *Mater. Res. Soc. Symp. Proc.* 546, 121 (1999).
213. S. Greek and F. Ericson, *Mater. Res. Soc. Symp. Proc.* 518, 51 (1998).
214. W. N. Sharpe, Jr. and A. McAleavey, *Proc. SPIE* 3512, 130 (1998).
215. J. J. Sniegowski and M. P. de Boer, *Ann. Rev. Mater. Res.* 30, 299 (2000).
216. J. M. Bustillo, R. T. Howe, and R. S. Muller, *Proc. IEEE* 86, 1552 (1998).

217. T. Yi and C. J. Kim, *Meas. Sci. Technol.* 10, 706 (1999).
218. X. D. Li and B. Bhushan, *Thin Solid Films* 340, 210 (1999).
219. B. Bhushan and X. D. Li, *J. Mater. Res.* 12, 54 (1997).
220. S. Johansson, J. A. Schweitz, L. Tenerz, and J. Tiren, *J. Appl. Phys.* 63, 4799 (1988).
221. C. J. Wilson and P. A. Beck, *J. Microelectromech. Syst.* 5, 142 (1996).
222. W. Suwito, M. L. Dunn, and S. J. Cunningham, in "Int. Solid-State and Actuators Conf.—Transducers' 97," Chicago, 1997, p. 611.
223. K. E. Peterson, *Proc. IEEE* 70, 5 (1982).
224. S. J. Cunningham, S. Wan, and D. T. Read, in "Int. Solid-State and Actuators Conf.—Transducers' 95," Stockholm, Sweden, 1995, p. 25.
225. K. Sato, M. Shikida, T. Yoshioka, T. Ando, and T. Kawbata, in "Int. Solid-State and Actuators Conf.—Transducers' 97," Chicago, 1997, p. 595.
226. T. Yi and C. J. Kim, in "Int. Solid-State and Actuators Conf.—Transducers' 99," Sendai, Japan, 1999, p. 518.
227. M. T. A. Saif and N. C. MacDonald, in "Ninth Int. Workshop on Micro Electro Mechanical Systems," San Diego, 1996.
228. J. Dual, E. Mazza, G. Schiltges, and D. Schlums, *Proc. SPIE* 3225, 12 (1997).
229. W. N. Sharpe, Jr., K. M. Jackson, K. J. Hemker, and Z. Xie, *J. Microelectromech. Syst.* 10, 317 (2001).
230. J. Bagdahn and W. N. Sharpe, Jr., *Mater. Res. Soc. Symp. Proc.* 687 (2002).
231. W. N. Sharpe, Jr., B. Yuan, and R. Vaidyanathan, in "10th Int. Workshop on Micro Electro Mechanical Systems," Nagoya, Japan, 1997, p. 424.
232. P. T. Jones, G. C. Johnson, and R. T. Howe, *Mater. Res. Soc. Symp. Proc.* 518, 197 (1998).
233. B. Bhushan and L. Xiaodong, *Thin Solid Films* 340, 210 (1999).
234. T. Tsuchiya, A. Inoue, and J. Sakata, in "Int. Solid-State and Actuators Conf.—Transducers' 99," Sendai, Japan, 1999, p. 488.
235. C. Seere, A. Perez-Rodriguez, A. Romano-Rodriguez, J. R. Morante, J. Esteve, and M. C. Acero, *J. Micromech. Microeng.* 9, 190 (1999).
236. S. Sundararajan and B. Bhushan, *Wear* 217, 251 (1998).
237. A. V. Sumant, O. Auciello, A. R. Krauss, D. M. Gruen, D. Ersoy, J. Tucek, A. Jayatissa, E. Stach, N. Moldovan, D. Mancini, H. G. Busmann, and E. M. Meyer, *Mater. Res. Soc. Symp. Proc.* 657 (2000).
238. S. A. Catledge, J. Borham, and Y. K. Vohraa, *J. Appl. Phys.* 91, 5347 (2002).
239. M. I. De Barros and L. Vandenbulcke, L. Chinsky, D. Rats, and J. von Stebut, *Diamond Related Mater.* 10, 337 (2001).
240. E. A. Ekimov, E. L. Gromnitskaya, S. Gierlotka, W. Lojkowski, B. Palosz, A. Swiderska-Sroda, J. A. Kozubowski, and A. M. Naletov, *J. Mater. Sci. Lett.* 21, 1699 (2002).
241. S. A. Catledge and Y. K. Vohra, *J. Appl. Phys.* 83, 198 (1998).
242. R. L. Newton and J. L. Davidson, in "Mechanical Properties of Structural Films" (C. L. Muhlstein and S. B. Brown, Eds.), p. 318. ASTM, West Conshohocken, PA, 2001.
243. A. Kant, M. D. Drory, N. R. Moody, W. J. MoberlyChan, J. W. Ager, and R. O. Ritchie, *Mater. Res. Soc. Symp. Proc.* 505, 611 (1998).
244. P. Gluche, M. Adamschik, A. Vescan, W. Ebert, E. Kohn, A. Floter, R. Zachai, H. J. Fecht, and F. Szucs, *Diamond Related Mater.* 7, 779 (1998).
245. M. D. Drory, R. H. Dauskardt, A. Kant, and R. O. Ritchie, *J. Appl. Phys.* 78, 3083 (1995).
246. A. Kant, M. D. Drory, and R. O. Ritchie, *Mater. Res. Soc. Symp. Proc.* 383 (1995).
247. S. Christiansen, M. Albrecht, and H. P. Strunk, *J. Mater. Res.* 11, 1934 (1996).
248. K. H. Lai, C. Y. Chan, M. K. Fung, I. Bello, C. S. Lee, and S. T. Lee, *Diamond Related Mater.* 10, 1862 (2001).
249. D. Schneider, C. F. Meyer, H. Mai, B. Schoneich, H. Ziegele, H. J. Scheibe, and Y. Lifshitz, *Diamond Related Mater.* 7, 973 (1998).
250. S. E. Coe and R. S. Sussmann, *Diamond Related Mater.* 9, 1726 (2000).
251. T. Michler, M. Grischke, I. Traus, K. Bewilogua, and H. Dimigen, *Diamond Related Mater.* 7, 1333 (1998).
252. J. C. Sanchez-Lopez, C. Donnet, J. L. Loubet, M. Belin, A. Grill, V. Patel, and C. Jahnes, *Diamond Related Mater.* 10, 1063 (2001).
253. J. Cumings, P. G. Collins, and A. Zettl, *Nature* 406, 586 (2000).
254. S. Paulson, M. R. Falvo, N. Snider, A. Helser, T. Hudson, A. Seeger, R. M. Taylor, R. Superfine, and S. Washburn, *Appl. Phys. Lett.* 75, 2936 (1999).
255. D. J. Lloyd, *Int. Mater. Rev.* 39, 1 (1994).
256. M. T. Kiser, F. W. Zok, and D. S. Wilkinson, *Acta Mater.* 44, 3465 (1996).
257. N. A. Fleck and J. W. Hutchinson, *J. Mech. Phys. Solids* 49, 2245 (2001).
258. N. A. Fleck, M. F. Ashby, and J. W. Hutchinson, *Scr. Mater.* 48, 179 (2003).
259. Y. Guo, Y. Huang, H. Gao, Z. Zhuang, and K. C. Hwang, *Int. J. Solids Struct.* 38, 7447 (2001).
260. Z. P. Bazant, Theoretical and Applied Mechanics Report 00-12/C99s, Northwestern University (2000).
261. Z. P. Bažant, *J. Mech. Phys. Solids* 50, 435 (2002).
262. J. L. Bassani, *J. Mech. Phys. Solids* 49, 1983 (2001).
263. A. Acharya and J. L. Bassani, *J. Mech. Phys. Solids* 48, 1565 (2000).
264. Z. P. Bazant and Z. Y. Guo, *Int. J. Solids Struct.* 39, 5633 (2002).
265. R. A. Toupin, *Arch. Ration. Mech. Anal.* 11, 385 (1963).
266. R. D. Mindlin, *Int. J. Solids Struct.* 1, 417 (1965).
267. M. Jirasek and Z. P. Bazant, "Inelastic Analysis of Structures." Wiley, New York, 2002.
268. S. H. Chen and T. C. Wang, *Acta Mater.* 48, 3997 (2000).
269. S. H. Chen and T. C. Wang, *Int. J. Plast.* 18, 971 (2002).
270. Z. P. Bazant, "Scaling of Structural Strength," Hermes-Penton Science (Kogan Publishing), London, 2002.
271. B. I. Yakobson and P. Avouris, *Topics Appl. Phys.* 80, 287 (2001).
272. K. N. Kudin, G. E. Scuseria, and B. I. Yakobson, *Phys. Rev. B* 64, 235406 (2001).
273. H. F. Bettinger, T. Dumitrica G. E. Scuseria, and B. I. Yakobson, *Phys. Rev. B* 65, 041406 (2002).
274. O. A. Shenderova, V. V. Zhirnov, and D. W. Brenner, *Crit. Rev. Solid State Mater. Sci.* 27, 227 (2002).
275. D. Appell, *Nature* 419, 553 (2002).
276. P. Ball, "Made to Measure." Princeton Univ. Press, Princeton, NJ, 1997.
277. Y. F. Zhao and B. I. Yakobson, *Phys. Rev. Lett.* 91, 035501 (2003).
278. M. B. Nardelli, B. I. Yakobson, and J. Bernholc, *Phys. Rev. Lett.* 81, 4656 (1998).
279. G. G. Samsonidze and B. I. Yakobson, *Comput. Mater. Sci.* 23, 62 (2002).
280. G. G. Samsonidze and B. I. Yakobson, *Phys. Rev. Lett.* 88, 065501 (2002).
281. T. Dumitrica, T. Belytschko, and B. I. Yakobson, *J. Chem. Phys.* 119, 1281 (2003).
282. Y. F. Zhao, B. I. Yakobson, and R. E. Smalley, *Phys. Rev. Lett.* 88 (2002).
283. B. I. Yakobson, U.S. Patent, 2001.
284. D. J. Jacobs and M. F. Thorpe, *Phys. Rev. Lett.* 75, 4051 (1995).
285. D. J. Jacobs and M. F. Thorpe, *Phys. Rev. E* 53, 3682 (1996).
286. B. X. Li, P. L. Cao, R. Q. Zhang, and S. T. Lee, *Phys. Rev. B* 65, 125305 (2002).
287. P. Sen, O. Gulseren, T. Yildirim, I. P. Batra, and S. Ciraci, *Phys. Rev. B* 65, 235433 (2002).
288. B. Marsen and K. Sattler, *Phys. Rev. B* 60, 11593 (1999).
289. S. Ismail-Beigi and T. Arias, *Phys. Rev. B* 57, 11923 (1998).
290. H. Yorikawa, H. Uchida, and S. Muramatsu, *J. Appl. Phys.* 79, 3619 (1996).

291. J. D. Holmes, K. P. Johnston, R. C. Doty, and B. A. Korgel, *Science* 287, 1471 (2000).
292. D. D. D. Ma, C. S. Lee, F. C. K. Au, S. Y. Tong, and S. T. Lee, *Science* 299, 1874 (2003).
293. R. H. Baughman, A. A. Zakhidov, and W. A. de Heer, *Science* 297, 787 (2002).
294. P. A. Williams, S. J. Papadakis, M. R. Falvo, A. M. Patel, M. Sinclair, A. Seeger, A. Helser, R. M. Taylor II, S. Washburn, and R. Superfine, *Appl. Phys. Lett.* 80, 2574 (2002).
295. J. Chung and J. Lee, *Sensors Actuators A* 104, 229 (2003).
296. M. F. Yu, B. S. Files, S. Arepalli, and R. S. Ruoff, *Phys. Rev. Lett.* 84, 5552 (2000).
297. M. F. Yu, B. I. Yakobson, and R. S. Ruoff, *J. Phys. Chem. B* 104, 8764 (2000).
298. Y. Zhang, A. Chang, J. Cao, Q. Wang, W. Kim, Y. Li, N. Morris, E. Yenilmez, J. Kong, and H. Dai, *Appl. Phys. Lett.* 79, 3155 (2001).
299. H. Dai, *Phys. World* 13, 43 (2000).
300. J. Kong, H. T. Soh, A. M. Cassell, C. F. Quate, and H. Dai, *Nature* 395, 878 (1998).
301. K. Yamamoto, S. Akita, and Y. Nakayama, *J. Phys. D* 31, L34 (1998).
302. L. Lin and M. Chiao, *Sensors Actuators A* 55, 35 (1996).